# QUANTIFICATION OF BLOOD VELOCITY AND VASCULAR WALL SHEAR RATE FROM ULTRASOUND RADIO FREQUENCY SIGNALS AND ITS RELATIONSHIP TO VASCULAR MECHANICAL PROPERTIES AND POTENTIAL CLINICAL APPLICATIONS

by

Dae Woo Park

A dissertation submitted in partial fulfillment
of the requirements for the degree of
Doctor of Philosophy
(Biomedical Engineering)
in The University of Michigan
2012

Doctoral Committee:

Professor William F. Weitzel, Co-Chair
Professor Albert J. Shih, Co-Chair
Professor J. Brian Fowlkes
Professor Jonathan M. Rubin
Research Investigator Grant H. Kruger

## Dedication

This dissertation is dedicated to my family and my wife Sun Woo who has shown an incredible amount of strength and faith in myself, has sacrificed incredibly to see me through this, and who I so longingly look forward to getting reacquainted with once this is completed.

## Acknowledgements

Research of this length and depth cannot happen without the help, guidance, and support of many people. It is with great appreciation and humility that I offer this work up for review.

I would like to thank my co-advisor, Professor William (Rick) Weitzel, for his guidance and support of my research. When I desperately needed to find an advisor who could support and guide me, he accepted me as a graduate student. Without his support and guidance, I could not have achieved this glorious fruit of research. He has provided me direction and ideas for this research. Through working with him, I have gained extensive experience in research and data analysis skills.

I would like to thank my co-advisor, Professor Albert Shih, for his guidance and support of my research. When I was looking for an advisor, he took me as a graduate student and allowed me to work with him. He gave me comments and advice whenever and wherever he was available despite of my lack of understanding. This dissertation could be successfully accomplished owing to his comments and suggestions. I appreciate his passionate guidance and advice again.

I would also like to thank my other committee members, Professor Jon Rubin, Grant Kruger, Ph.D, Professor Cheri Deng and Professor Brian Fowlkes for their guidance and critiquing of this research as it progressed. I appreciate their support and advice throughout this entire process.

Professor Jon Rubin has given me the idea and much advice during this research. He has often attended the elasticity meetings to listen and offer advice. His advice affected tremendously direction of this research. He also gave me generous compliments and encouragements.

Dr. Grant Kruger has given me much help during this research. I have learned much ultrasound background knowledge from him when I was preparing for the qualifying

exam. He suggested many ideas in the elasticity meetings and they were very helpful for this research. He also greatly contributed during the revision of the vascular wall elasticity paper (chapter 2).

Professor Cheri Deng has given me much advice during this research. Her critical questions in the qualifying exam inspired me to study and investigate more about the ultrasound background knowledge. I also learned much research skills and knowledge while I was working in her lab for the ultrasound skin compression measurements. Those research skills were helpful for this research.

Professor Brian Fowlkes made himself available to serve as my committee member. His willingness to serve as my committee member was much appreciated. Additionally, I have learned a lot of fundamental ultrasound knowledge from his class and this was helpful for this research.

This thesis would also not have been possible without the help of many people from across the University. First, I would like to give my deepest thanks to James Hamilton. He gave me much help to achieve the goals of this research. He offered a lot of advice and suggestions during this research and those were really helpful for successful achievement of this research.

Paul Gottschalk has also been invaluable to my work. He suggested a lot of useful ideas for this research at the elasticity meetings. I needed a professional person who could answer my questions about this research and he spent his time to answer my questions.

Rob Dodde has also been helpful during my research. He has been my office mate and has given me useful advice and suggestions during this research, sitting right next to me.

I would like to thank David Conway, Ben Carpenter, Chris Diroff for their help in performing flow experiments, especially during those times when I desperately needed it; they were there to support me with their skills and time.

I must give thanks to my fellow office mates, and a special thanks to Melissa Rippee, for her assistance during many years of my research. She helped me to get experimental tools and reserve a place to perform this research.

Finally, I owe my largest thank you to my family, for their encouragement and patience throughout this process. It has not been easy and I know it would not have been possible without my loving wife. I am married to an incredible woman, as my Ph.D. research wrapped up. Sun Woo has sacrificed her study to help me, and for that I am endlessly appreciative. Thank you from the bottom of my heart for your encouragement and love; I will love you always. To my parents, who have always been so proud of me, thank you not only for the encouragement, but for everything you have given me over the years. I owe much of what I have become to you. To the rest of my family, some of whom I have not even seen in many years, I love you all and look forward to seeing you again soon.

# Table of Contents

## List of Figures

# List of Tables

## Abstract

This study evaluates a novel measurement method of determining vascular wall strain and wall shear rate, which are interrelated physiologic parameters fundamentally important in vascular disease. Wall strains during vascular wall dilation were performed using ultrasound 2D speckle tracking; vascular wall edges and vascular wall shear rate were determined using decorrelation based velocity measurement method for *in-vitro* and *in-vivo* flow measurement. These experiments and measurements were performed to investigate both the novel measurement methods as well as the relationship between the vascular wall shear rate and vascular wall dilation. First, this study measures the strains of the arterial wall using the ultrasound radio-frequency (RF) signals. The RF signals were acquired from B-mode images of a human brachial artery for healthy adult subjects under normal physiologic pressure and the use of external pressure (pressure equalization) to increase strain. Strains in the arterial wall during arterial dilation (from diastole to systole) were determined using a 2D speckle tracking algorithm. These ultrasound results were compared with measurements of arterial strain as determined by finite-element analysis (FEA) models with and without the effects from surrounding tissue, which was represented by homogenous material with fixed elastic modulus. The ultrasound and FEA strain measurements were not much different under physiologic pressure. Under pressure equalization, however, the strain levels predicted by FEA model without surrounding tissue were considerably greater than the strain levels measured by both ultrasound and the FEA model with surrounding tissue, which were relatively similar. Second, this research aims to measure wall edges and wall shear rate for *in-vitro* flow experiment using decorrelation ultrasound based velocity measurement. By moving a transducer with a given speed on a tissue-mimicking phantom, the speckle movements versus correlation curves were obtained for each depth using 2D tracking. The flow velocity was obtained by multiplying the speckle movement in two consecutive frames by the acoustic frame rate. The wall edge was determined using B-mode images and 2$^{nd}$ order gradient of flow velocity profiles. The wall shear rate was measured at the

wall edge and evaluated by comparison with velocity gradients from parabolic flow velocity profile based on Poiseuille theory. The decorrelation flow velocity measurement method demonstrated to be more accurate than the lateral speckle tracking method for the prediction of the wall shear rate. Third, this research measures the vascular wall shear rate in the brachial artery for nine healthy, six chronic kidney disease and two end-stage renal disease subjects using the decorrelation based ultrasound velocity measurement. The vascular wall shear rate and vascular diameter pre-, during- and post-vascular occlusion with pressure cuffs were compared for five healthy and three renal disease (two chronic kidney disease and one end-stage renal disease) subjects at top and bottom wall edges. The healthy subjects had significantly higher mean and maximum vascular wall shear rate than renal disease subjects at top and bottom vessel wall edges. The mean vascular wall shear rate change between pre- and post-vascular occlusion was also significantly different for the healthy versus renal disease subjects. These research findings validate the underlying novel measurement methods and determine the relationship between the vascular wall shear rate and vascular wall dilation. This relationship can be corroborated by considering vascular wall elasticity during vascular dilation and these results indicate that these measurements can be improved by incorporating the effects of surrounding tissue in vascular modulus estimation.

# Chapter 1 Introduction

## 1.1 Motivation

Patients with chronic kidney disease (CKD) and end-stage renal disease (ESRD) have high risk of cardiovascular disease due to vascular calcification (1) and accelerated atherosclerosis, caused at least in part by abnormal endothelial function (1-3). For the detection of future cardiovascular risk, the vascular wall dilation has been measured between pre- and post-vascular occlusion in flow mediated dilation (FMD) measurements (4). The vascular wall shear rate (WSR) is a significant factor influencing vascular wall dilation (4). The accuracy of FMD measurements will be improved by determining the relationship between WSR and vascular wall dilation. This relationship is corroborated by considering vascular wall elasticity because the vascular wall dilation is not only associated with the WSR, but vascular wall elasticity (5).

First, this study measures the elasticity of the arterial wall using ultrasound radio-frequency (RF) signals. The RF signals are acquired from B-mode images of a human brachial artery for healthy adult subjects under normal physiologic pressure and the use of external pressure (pressure equalization) to increase strains. Strains in the arterial wall during arterial dilation (from diastole to systole) are determined using a 2D speckle tracking algorithm. These ultrasound results are compared with measurements of arterial strain as determined by finite-element analysis (FEA) models with and without the effects from surrounding tissue, which is represented by a homogenous material with fixed elastic modulus. Second, this research aims to measure wall edges and wall shear rates for *in-vitro* flow experiments using decorrelation ultrasound based velocity measurement. By moving a transducer at a given speed on a tissue-mimicking phantom, the speckle movements versus correlation curves are obtained for each depth using 2D tracking. The flow velocity is obtained by multiplying the speckle movement in two consecutive frames by the acoustic frame rate. The wall edge is determined using B-mode images and 2$^{nd}$

order gradient of flow velocity profiles. The wall shear rate is measured at the wall edge and evaluated by comparison with velocity gradients from parabolic flow velocity profiles based on Poiseuille theory. Third, this research measures the vascular wall shear rate in the brachial artery for nine healthy, six chronic kidney disease and two end-stage renal disease subjects using the decorrelation based ultrasound velocity measurement. The vascular wall shear rate and vascular diameter pre-, during- and post-vascular occlusion with a pressure cuff are compared for five healthy and three renal disease (two chronic kidney disease and one end-stage renal disease) subjects at top and bottom wall edges.

## 1.2 Literature Review

### 1.2.1 *Review of Vascular Wall Elasticity Measurements*

Ultrasound techniques have been utilized for non-invasive measurements of vascular elasticity including vessel wall motion estimation, intraparietal strain imaging, and pulse-wave velocity measurement (6-12). Vessel compliance measurements were also conducted by monitoring internal pulsatile deformation in tissues surrounding the normal brachial artery (13). Vascular wall strain measurements have been achieved using these techniques, but dynamic range of strain measurement was limited due to small arterial pulsation under physiologic arterial pressure.

To expand the strain dynamic range, the pressure equalization technique has been developed. Using pressure equalization, the mean arterial pressure was lowered by applying an external force on the artery (14, 15).

### 1.2.2 *Review of Doppler Ultrasound Flow Velocity Measurements*

Doppler ultrasound measurements have been widely used to measure blood flow in vessels using the frequency shift due to fluid reflector motion based on the assumption that the angle between the beam and the vessel orientation is known (16). Multi-gate ultrasound Doppler has advanced spatial resolution and is able to measure the flow velocity profile at the wall edges (16) and has been applied in this setting to measure the WSR from the longitudinal view of the blood vessel (17-22) based on 1D velocity measurement. The multi-gate ultrasound Doppler also depends on the assumptions that

the lumen is circular and that the flow is symmetrical in the out-of-plane directions, both of which are violated in the presence of vascular tortuosity and branching (16).

### 1.2.3 *Review of Lateral Speckle Tracking Flow Velocity Measurements*

The tracking of ultrasound RF signals has been utilized to study blood flow velocity profiles. Using correlation based lateral speckle tracking, blood flow velocity profiles have been measured from longitudinal views of blood vessels (23-27). However, B-mode image acquisitions of longitudinal views of blood vessels were limited by vascular tortuosity and branching (28).

### 1.2.4 *Review of Decorrelation Flow Velocity Measurements*

Transverse views of blood vessels have been used to measure blood velocity profiles. For transverse views of blood vessels, the decorrelation of ultrasound RF signals along 1D A-line and in 2D B-mode images have been applied to the study of blood velocity profiles. Using the decorrelation of ultrasound RF signals, the vessel wall interface could be detected (29) and blood flow velocity profile was qualitatively identified (30). The blood flow velocity profile measurement using the decorrelation of ultrasound RF signals from A-lines has been demonstrated, but the quantification of blood flow velocity was not achieved.

RF signals of 2D B-mode images were used to determine the blood flow profiles in transverse views of a vessel. Bamber et al. (31) demonstrated that decorrelation could be used to identify blood flow using the time rate-of-change of correlation in B-mode images. Li et al. (32) has theoretically demonstrated the linear decrease of correlation according to elevational speckle movement. Speckle decorrelation has been used to measure the motion of transducer to produce 3D ultrasound images (32-35). This technique has been applied by Rubin et al. (36) to qualitatively identify the blood flow profile in both in-vitro flow phantom and *in-vivo* animal studies. Rubin et al. (37) also used the Doppler flow measurements to improve the accuracy of volumetric flow from the decorrelation based flow profiles and theoretically modeled exponential decrease of correlation according to elevational speckle movement. Previous research demonstrated that speckle decorrelation could generate flow velocity profiles, but the decorrelation was not experimentally measured.

## 1.3 Research Objectives and Tasks

The primary objective of this research is to evaluate novel measurement methods of determining vascular wall strain and WSR, which are interrelated physiologic parameters fundamentally important in vascular disease. As discussed above in the motivation (Section 1.1) it is a reasonable hypothesis that the accuracy of vascular wall strains and WSR measurements in vessels will be improved using the ultrasound RF signals. The secondary objective of this research is to investigate the relationship between the WSR and vascular wall dilation. These objectives are accomplished throughout the process include:

a) the arterial wall elasticity measurements using ultrasound 2D speckle tracking and the evaluation of surrounding tissue effects on the arterial wall strain and stress using finite element analysis
b) the wall edges and edge velocity gradient measurements for *in-vitro* flow experiment using the speckle decorrelation flow velocity measurement
c) the WSR and vascular diameter pre-, during- and post-vascular occlusion with pressure cuff measurements for healthy and renal disease subjects using the decorrelation based flow velocity measurement

## 1.4 Outline

This dissertation presents vascular wall elasticity measurements using ultrasound RF signals as well as vascular wall edges and WSR measurements using decorrelation based ultrasound flow velocity measurement.

Chapter 1 of the dissertation provides the primary motivations for this doctoral research as well as a literature review of related research work.

Chapter 2 describes the arterial wall strain measurements using ultrasound 2D speckle tracking and the evaluation of surrounding tissue effects on the arterial wall strain and stress using finite element analysis.

Chapter 3 illustrates the wall edge and edge velocity gradient measurements for *in-vitro* flow experiment using decorrelation based ultrasound flow velocity measurement.

Chapter 4 presents the vascular wall shear rate and vascular diameter pre-, during- and post-vascular occlusion with pressure cuff measurements for healthy and renal disease subjects using decorrelation based ultrasound measurement.

Chapter 5 concludes this research and provides ideas for future work in this field along with the author's original contributions.

# Chapter 2 Vascular Wall Elasticity Measurements

## 2.1 Introduction

Arterial stiffness is associated with numerous disease processes, including cardiovascular and renal disease, peripheral vascular occlusive disease, and diabetes. A possible cause of this increased stiffness includes a change in the ratio of collagen to elastin in the extracellular matrix of the arterial media (38-40). A variety of noninvasive techniques have been employed to measure arterial stiffness and vascular elasticity. The pulse-wave velocity (PWV) technique estimates average arterial stiffness on the basis of the travel time of a wave between two measurement sites. PWV is considered one of the best methods of measuring stiffness when time of propagation of the arterial pulse is determined between the carotid and femoral arteries (41). But carotid-femoral PWV results may differ substantially depending on whether time is measured from the foot of the waveform (using an arterial tonometer) or the point of maximum systolic upstroke (42). Local arterial stiffness is poorly defined by PWV and the resolution of this technique is limited by reflected waves and blood noise. Improvements in PWV estimates of local strain have been obtained by using the radiation force of ultrasound to generate propagating waves in arterial walls (43). The same research group has distinguished between normal and calcified femoral arteries in pigs *in-vivo* using vibroacoustography, which allows imaging of objects on the basis of the acoustic signal produced by two intersecting ultrasound beams (44). Ultrasound estimates of vessel wall motion have included studies to measure femoral artery diameter and pulsatile changes in diameter to evaluate vessel thickness and stiffness in type 2 diabetes mellitus (12), carotid artery diameter and wall motion to determine the relationship of arterial calcification to vessel stiffness in end-stage renal disease (9), and femoral and carotid artery compliance in chronic dialysis patients (10). Vessel compliance has been measured by monitoring internal pulsatile deformation in tissues surrounding the normal brachial artery (13). Several studies have explored use of tissue Doppler imaging in pulse-wave velocity

(PWV) and intraparietal strain measurements (8, 11). To maximize the accuracy of motion estimation, high-resolution ultrasound with speckle tracking algorithms have been employed (45, 46) in the renal setting to measure the mechanical properties of arteries and transplant kidneys, demonstrating the potential to distinguish between normal and fibrotic tissue (47).

Blood vessels are examples of subsurface organs or tissue with highly nonlinear mechanical properties. When palpated, nonlinear structures undergo "strain stiffening" where there is less strain for a given pressure differential with increasing deformation (47). Arteries distended under normal physiologic pressure produce little strain because the normal arterial wall is a nonlinear elastic medium. This relatively low level of strain effectively limits the accuracy of measurements of the mechanical properties of arteries under physiologic conditions. However, lowering the transmural pressure on the arterial wall by applying external compression increases wall strain and deformation for a given pressure differential (14, 47). Our elasticity imaging technique achieves pressure equalization by means of continuous freehand compression or use of a blood pressure cuff. The applied external force produces internal pressure comparable to that resulting from measurement of a subject's blood pressure. The artery pulsates maximally when the applied external pressure equals the diastolic pressure, and the vessel collapses completely when the applied pressure is greater than the systolic pressure. The broader range of strain resulting from this technique may improve the ability to distinguish noninvasively between normal and diseased arterial walls if motion tracking can be performed accurately. With use of the pressure equalization procedure, ultrasound elasticity imaging with speckle tracking has the potential to track motion accurately and thereby detect subtle changes in strain in the vascular wall with unprecedented precision and accuracy (14, 47, 48).

Previous ultrasound estimates of radial artery strain considered only the nonlinear elastic properties of the artery (14), noting the artery modulus to be substantially greater than that of the surrounding tissue. This allows one to approximate the modulus estimates of the artery using strain measurements from the arterial wall alone, ignoring the effects on strain of the much larger and softer surrounding tissue. However, surrounding tissue has the potential to absorb or transmit pressure to the artery and may

have a particularly important effect on arterial strain when external compression is applied (14, 47). While it may seem reasonable to use only arterial wall strain measurements to approximate the modulus estimates under physiologic conditions, an interesting phenomenon occurs during pressure equalization - Not only does the artery wall modulus decrease by "unloading" the vessel, reducing transmural pressure with pressure equalization, but the opposite change occurs in the surrounding tissue. The present study evaluates the effect of the surrounding tissue modulus and validates the strain results of artery under both normal physiologic pressure and pressure equalization. Two FEA artery models are used, one with and one without surrounding tissue modulus effects, and the FEA results are compared with *in vivo* high-resolution ultrasound data.

## 2.2 Materials and Methods

### 2.2.1 *Elasticity Imaging*

Local, nonlinear, high-resolution ultrasound elasticity imaging was performed on a 45-year-old healthy human male subject. The subject was enrolled for our study after providing informed consent, under a study protocol approved by our institution's Investigational Review Board. A Philips (Bothell, WA) IU22 ultrasound scanner with a 7-MHz center frequency linear array transducer was used for data collection at frame rates of approximately 180 frames per second. The subject was seated and his arm placed in the supinated position and extended forward along the sagittal plane and resting at approximately heart level on a solid surface. The scan head was aligned on the anterior surface of the forearm so that the scan plane aligned $90^{o}$ to the elbow-wrist axis (coronal plane), enabling a true accurate cross-section of the brachial artery to be obtained. Observing the B-scan images, continuous freehand positioning over the arterial region of interest was conducted, ensuring the artery remained approximately in the center of the image. Dilation of the subject's brachial artery was observed in response to the transmitted transmural pulse pressure within the artery induced by physiologic cardiac pulsations under normal atmospheric pressure. Imaging was also performed using the same method, but with the pressure equalization technique (14, 47). The external pressure was applied to the surface of the arm directly above the brachial artery using the transducer head for both tasks. When the external pressure matched the patient's diastolic

blood pressure, maximal pulsation of the artery was achieved. The real-time RF data were recorded continuously for each B-mode image frame for off-line post processing.

During post-processing of the RF ultrasound signals, the displacements of the brachial artery and surrounding structures were tracked from frame-to-frame (over time), using a high-resolution, two-dimensional, correlation-based phase-sensitive speckle tracking algorithm (45, 46). Figure 2-1 illustrates the estimation of vessel deformation through a cross-section of an artery along the reflected post-receive beam formed RF signature.

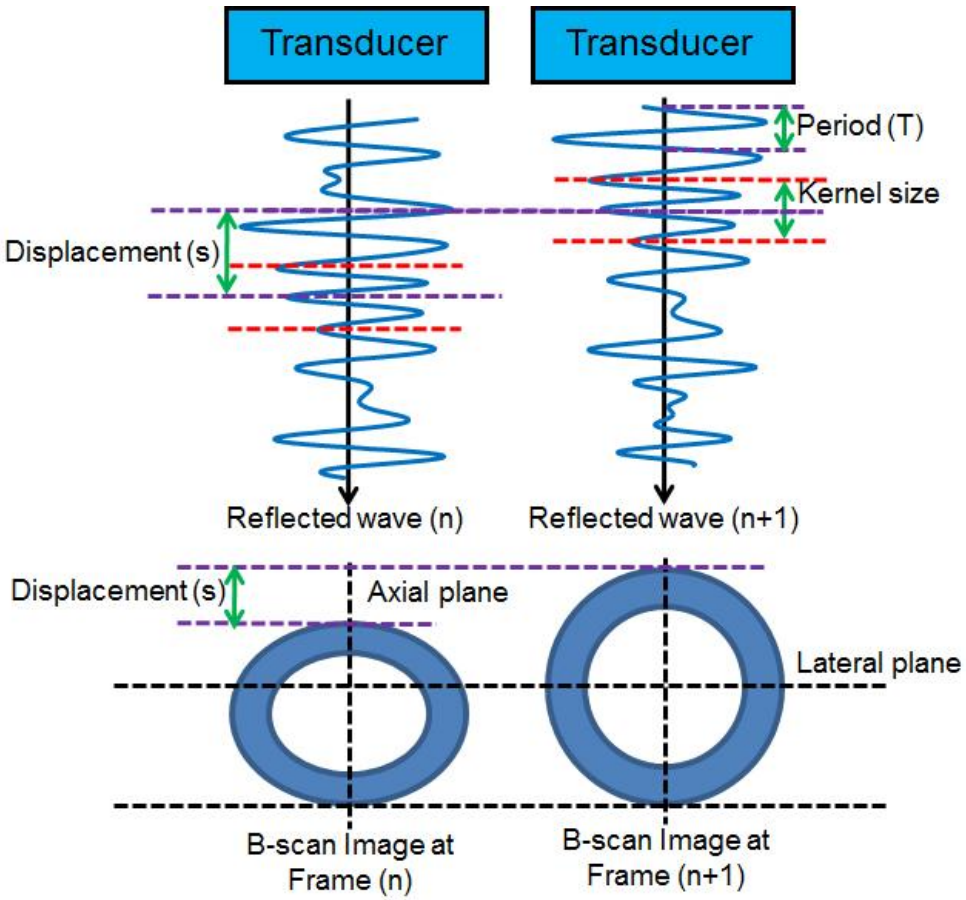


Figure 2-1. Illustration of the displacement determined from the frame-to-frame "lag" distance calculated using the correlation between the characteristic underlying radiofrequency (RF) ultrasound signals between frames.

Initially, the ultrasound array is pulsed in a fashion as to create a longitudinal acoustic wave in the form of a focused beam. As this beam crosses tissue interfaces with varying acoustic impedances, a certain portion of the wave is reflected, while the rest of the energy is transmitted deeper into the tissue. The reflected beam is received by the transducer, amplified, filtered and sampled to form a sequence of discrete numeric values accurately representing the reflected waveform. Digital signal processing is then used to calculate the correlation between each reflected beam from consecutive frames. For each new reflected signal obtained, kernels (vectors of sequential samples) are extracted, time shifted to various degrees, multiplied and summed with the previous beam to produce a third cross-correlation signal. A general form of this equation is shown in Equation 2-1, where $x$ is the reflected signal, and $i$ is the position and shift of the kernel, $h$, along the signal:

$$y[i] = \sum_{j=0}^{M-1} h[j]\, x[i-j]$$

Equation 2-1

The maximum of $y[i]$ indicates the position of closest match between the signals. Since the reflections are due to physical structures in the tissue, mechanical deformation (i.e., compression) produces shifts in sequential reflected waveforms. The amount of signal shift required to find the maximum correlation corresponds to the tissue deformation. Because the transmission time of each beam is accurately controlled, the deformation between time intervals can be determined, therefore the velocity of tissue features can be determined. The derivative with respect to space of the displacement provides the strain. For 2-D speckle tracking this process is repeated multiple times for each beam as well as between adjacent beams constituting the image. For our study, the lateral and axial displacements were calculated at the position of the maximum correlation coefficient, using a correlation kernel size approximately equal to the speckle spot. The axial displacement estimate was then further refined by determining the phase zero-crossing position of the analytic signal correlation. A spatial filter twice as large as the kernel size was used to enhance signal-to-noise ratio with good spatial resolution. A weighted correlation window and spatial filtering of adjacent correlation functions were

used to reduce frame-to-frame displacement error (45). To support calculation of Lagrangian strain, interframe motion of reference frame (e.g., first frame) pixels were integrated to produce the accumulated tissue displacement. Spatial derivatives of the displacements were calculated in a region of the artery to estimate the radial normal strain. The principal components of strain were determined according to the direction of the ultrasound beam. Longitudinal strain is the axial strain measured along the beam direction, and lateral strain is perpendicular to the axial strain. Longitudinal strain is more accurate than lateral strain, as resolution is at least an order of magnitude greater along the ultrasound beam than in the lateral (across beam) direction (see Figure 2-1). Therefore, all strains were measured in the axial direction and at regions with maximum axial strain values: top, bottom and both sides of arterial wall.

### 2.2.2 *Finite-element Analysis (FEA)*

With regard to FEA modeling, it is necessary to obtain accurate Young's modulus values for the materials/tissues used. A microelastometer (model 0301, ARTANN Laboratories, West Trenton, New Jersey) was used to empirically measure the strain/stress relationship on samples of bovine peripheral muscular artery and surrounding tissue obtained from a butcher shop. Cylindrical tissue specimens with a diameter of 1 mm and height of 2 mm were separately cut from the arterial wall and surrounding tissue and individually placed between the stamp and bottom plate of the microelastometer. The distance between the bottom plate and base of the microelastometer stamp was used as the reference point for displacement measurement. The tissue sample was compressed to a force of 150g or 70% of the starting height (whichever limit is met first) to obtain the tissue's force/height dependence (49). The stress (force per unit area) versus strain (change in length) results were calculated based on the height, force and cross-sectional area of the tissue. These quantities can be related through the following equation to obtain the Young's modulus of elasticity for the tissue,

$$E = \frac{\sigma}{\varepsilon} = \frac{FL_0}{A_0 \, \Delta L} \qquad \text{Equation 2-2}$$

where $\sigma$ and $\varepsilon$ are the stress and strain, respectively, $F$ is the applied force in Newtons, $L_0$ and $A_0$ represent the initial non-deformed length and cross-sectional area, and $\Delta L$ is the change in length. Because the tissue exhibits a non-linear elastic response the Young's modulus varies depending on the values of $L_0$ and $\Delta L$, with the tangent to the stress-strain curve indicating the Young's modulus for a specific $L_0$. However, as $\Delta L \rightarrow 0$ inaccuracies in measurement become more pronounced. For our analysis we assumed a linear elastic response (Hooke's Law) over the region of interest as $\Delta L$ is small for pulsatile arterial pressure variations considered in our research.

FEA of the artery models with and without surrounding tissue was performed using ABAQUS software (Simulia, Providence, Rhode Island), version 6.4, and the Young's moduli obtained in the microelastometer experiment. The axial strain was analyzed under conditions simulating both physiologic pressure and pressure equalization. A simplified model of the brachial artery and its surrounding tissue was designed (Figure 2-2). For the FEA model, the quadratic-dominated element shape was used. Dimensions were determined on the basis of the ultrasound B-mode image, and boundary conditions were based on the ultrasound experiment.

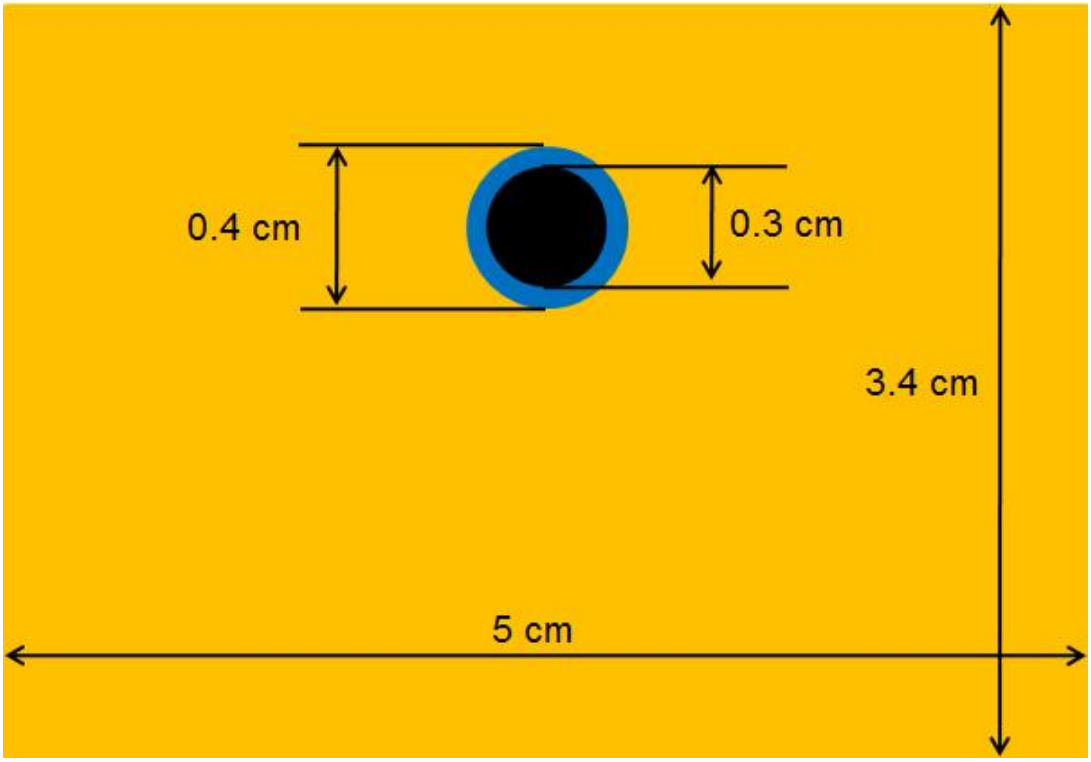


Figure 2-2. Finite-element analysis (FEA) model of artery and surrounding tissue, including dimensions.

We assumed the volume of the surrounding tissue to be much larger than that of the artery. Thus, the boundary conditions for surrounding tissue included a fixed bottom and sides that were free to move vertically but not horizontally (horizontally symmetric conditions). Two-dimensional mesh was designed to analyze this model. Volume change of the tissue was assumed to be negligible and thus the Poisson's ratio was regarded as 0.5.

## 2.3 Results

### 2.3.1 *Elasticity Imaging*

The accumulated displacement of the arterial wall was calculated from the pixel-by-pixel displacement relative to the original frame starting at diastole of the cardiac cycle. Normal accumulated strain values were obtained from the accumulated displacement, and the average strain value was estimated from five regions of interest chosen along the arterial wall during one pulsation of the artery. These strain values show axial strains, as

shown in Figure 2-1, that were derived from spatial derivatives of the displacements in a region of the artery. The axial strain values were converted to radial normal strain by changing vector direction according to the radial normal direction of the arterial wall in order to compare the imaging and FEA strain results. Figure 2-3 shows the B-scan image and strain-versus-time plot of five regions of interest along the top edge of the vessel wall during one cardiac cycle under physiologic pressure.

Analysis of all images showed the average strain under physiologic pressure was about –5% at the top and bottom of the arterial wall and 1% and 3% at the sides, compared to about –26% at the top and 11% and 24% at the sides under equalized pressure. (The value of average strain at the bottom of the wall under pressure equalization was disregarded as unreliable due to poor tracking). The vertical dashed line in Figure 2-3 represents the time at end-diastole (or onset of systole) when wall strain magnitude is at minimum.

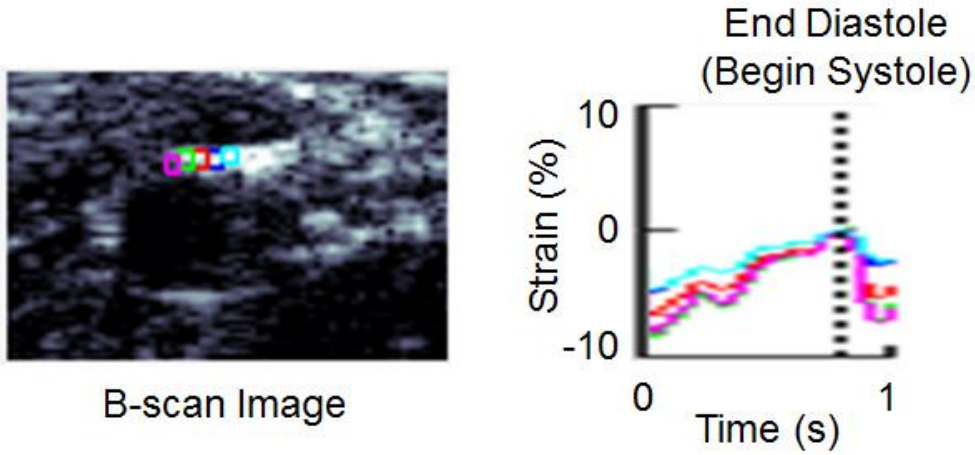


Figure 2-3. B-scan image and the strain-versus-time plot during one cardiac cycle under physiologic pressure. The average strain differences are calculated from five regions of interest along the arterial wall using ultrasound elasticity imaging.

### 2.3.2 *Finite-element Analysis (FEA)*

Figure 2-4 provides the results of the bovine artery and surrounding tissue microelastometer experiments as stress-strain curves. It can be seen that although strain is nonlinear overall, it can be approximated as a piecewise linear function over each of the physiologic and pressure equalization ranges.

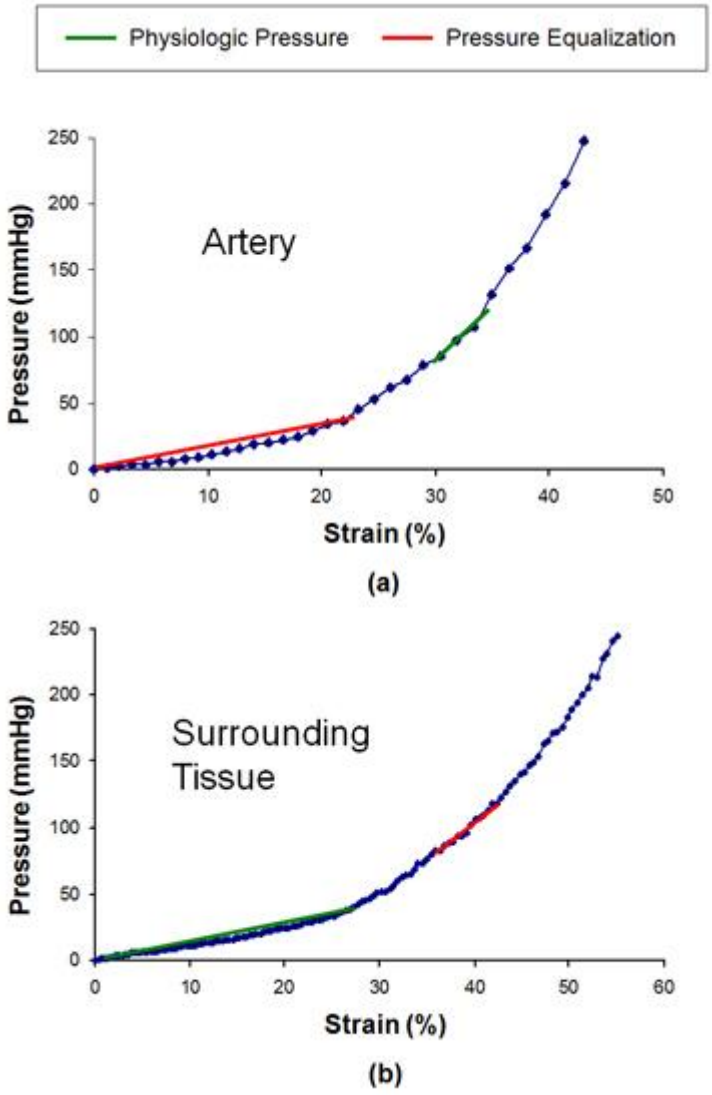


Figure 2-4. Stress-strain relationship for (a) bovine arterial wall and (b) surrounding tissue. The linear approximations of Young's modulus used in the finite-element analysis (FEA) model are summarized in Table 2-1.

Table 2-1 gives the Young's modulus values determined for each pressure range, using Equation 2-2, where σ is the change in pressure in kilopascals inside the artery and ε is the strain.

Table 2-1 The Young's moduli of artery and surrounding tissue under physiologic pressure and pressure equalization

| | Artery | Surrounding Tissue |
|---|---|---|
| Physiologic pressure | 118 kPa | 14 kPa |
| Pressure equalization | 22 kPa | 76 kPa |

Figure 2-5(a) shows the boundary conditions and mesh on the artery model with surrounding tissue. Figure 2-5(b) shows the strain distribution in the tissue under physiologic pressure. As the internal pressure increases from 80 to 120 mmHg, the radius of the artery increases, but the thickness of the arterial wall decreases. From Figure 2-5(b) it can be seen that the lateral sides (left and right) of the artery expand outwards, while the axial edges (top and bottom) tend to move inward (indicated as a negative strain) toward the center of the artery. In the ultrasound experiment, the subject's upper arm rests flat on a table, and pressure equalization is achieved by using the transducer to apply pressure to the arm. Thus, the bottom of the surrounding tissue is constrained while pressure is applied to the top. Under conditions of normal physiologic blood pressure of 120/80 mmHg, the transmural arterial wall pressure increases from 80 (diastolic) to 120 (systolic) mmHg. Under these conditions the artery and tissue are already under a certain amount of strain, as can be seen from Figure 2-4(a) and Figure 2-4(b), resulting in a certain amount of resistance against further expansion of the vessel. A specific arterial pressure results in a force on the internal lumen wall of the artery. This force results in a displacement, or expansion of the artery. Due to the base strain offset (pre-strain) imposed due to the physiologic pressure and non-linear elastic response (steeper Young's modulus), a small displacement change occurs as the physiologic pressure pulses. As the artery expands, the arterial wall and surrounding tissue are deformed, resulting in an increasing elastic force opposing the pressure induced force.

Arterial deformation reaches equilibrium when the sum of the force vectors balance, which occurs relatively quickly due to the slope of the stress-strain curve. During the pressure equalization procedure used to illicit nonlinear behavior of the arterial wall (50), an external force is applied, which results in deformation of the artery and surrounding tissue. This deformation is again balanced by the reaction force due to the elasticity of the tissue. When the reaction force exceeds the pressure-induced force, the vessel collapses. As the physiologic pressure pulses, the pressure force exceeds the external force and the artery expands again until the forces are once again in equilibrium. Due to the external force, the base strain offset (pre-strain) is removed so the expansion occurs over an area of the stress-strain curve with a lower Young's modulus, meaning that a larger displacement is necessary to balance the forces.

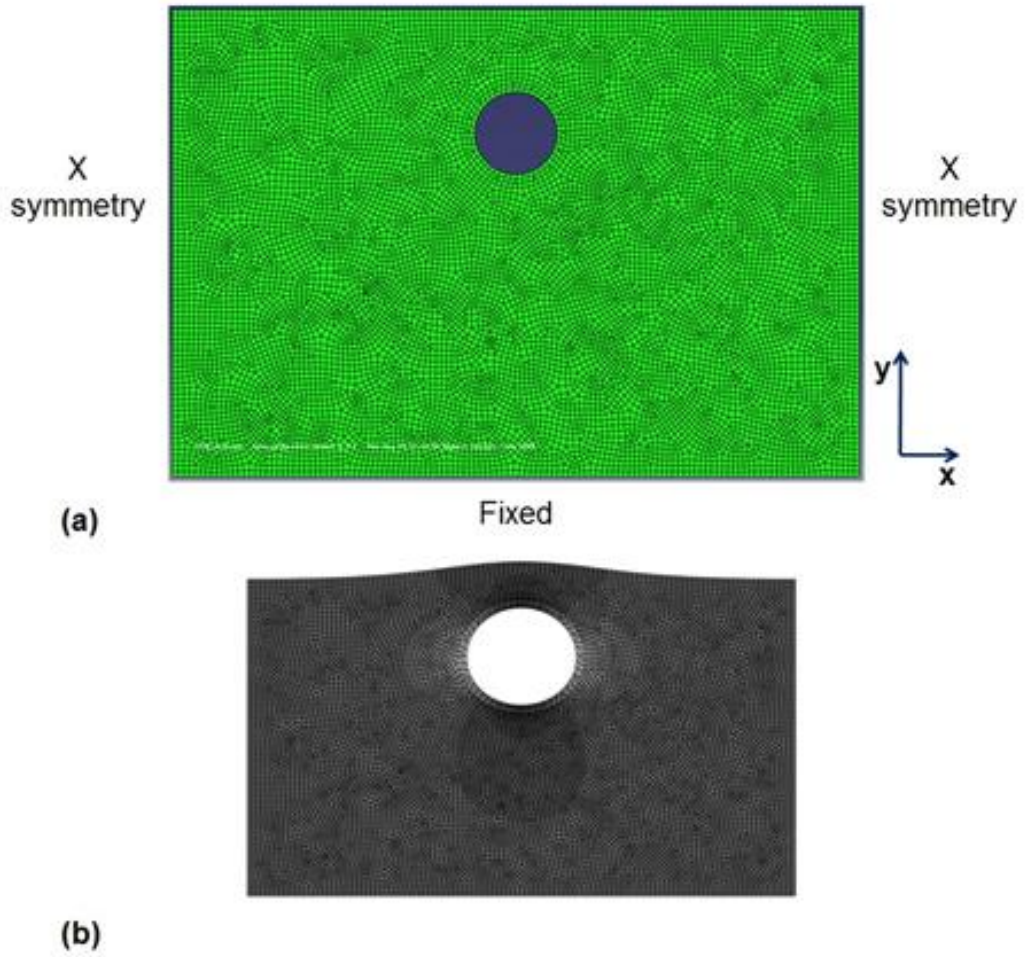


Figure 2-5. (a) The boundary condition and (b) strain distribution under physiologic pressure of the finite-element analysis (FEA) artery model.

Average strains and standard deviations (STDs) of n = 5 regions of interest obtained from the FEA artery models for both physiologic pressure and equalized pressure are

shown in Table 2-2, where they are compared with the ultrasound imaging results.

Table 2-2. The average strains of artery and surrounding tissue under physiologic pressure and pressure equalization.

| | Region | Ultrasound Results | FEA1 | FEA2 |
|---|---|---|---|---|
| Physiologic pressure | Top | -0.050 ± 0.023 | -0.086 ± 0.008 | -0.113 ± 0.004 |
| | Bottom | -0.058 ± 0.013 | -0.086 ± 0.009 | -0.111 ± 0.003 |
| | Left | 0.012 ± 0.011 | 0.134 ± 0.011 | 0.170 ± 0.005 |
| | Right | 0.034 ± 0.019 | 0.136 ± 0.009 | 0.170 ± 0.004 |
| Pressure equalization | Top | -0.256 ± 0.073 | -0.194 ± 0.043 | -0.606 ± 0.023 |
| | Bottom | -0.059 ± 0.009 (Poor tracking) | -0.213 ± 0.038 | -0.598 ± 0.016 |
| | Left | 0.115 ± 0.112 | 0.161 ± 0.021 | 0.914 ± 0.025 |
| | Right | 0.241 ± 0.141 | 0.164 ± 0.016 | 0.915 ± 0.019 |

FEA and imaging results are also compared in Figure 2-6(a) and Figure 2-6(b) for the regions of interest at the top and sides, respectively, of the arterial wall. Under physiologic pressure, the average strain at the top and bottom of the arterial wall in the model with surrounding tissue (FEA1) was –9%, compared to –11% in the model without surrounding tissue (FEA2). The difference in average strain values at the sides was 13% versus 17% in the models with and without surrounding tissue, respectively. Under pressure equalization, however, the differences in average strain values between the two models were considerably greater: –20% versus –60% in the models with and without surrounding tissue, respectively, at the top and bottom regions of interest; and 16% versus 91% in the models with and without surrounding tissue, respectively, at the sides of the arterial wall.

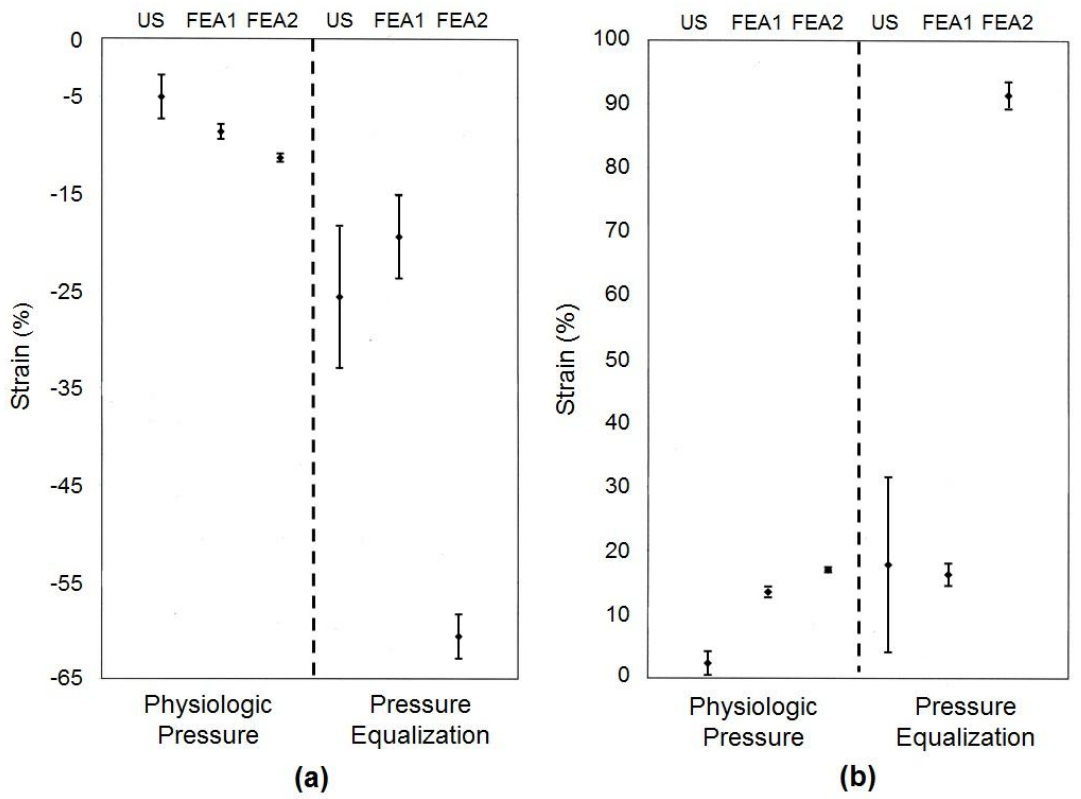


Figure 2-6. Average strain values and standard deviations from five regions of interest at the (a) top and (b) sides of the arterial wall under physiologic pressure and pressure equalization, as determined by high-resolution ultrasound imaging with speckle tracking (US) and finite-element analysis models with surrounding tissue (FEA1) and without surrounding tissue (FEA2).

Figure 2-7 shows the stress distribution of the artery model with surrounding tissue (FEA1) under both physiologic pressure and pressure equalization, with arrows showing high stress regions. Maximum stress increased from about 235 to 356 mmHg under physiologic pressure and was concentrated inside the arterial wall. On the other hand, the high-stress region was outside of the vessel wall under pressure equalization, when maximum stress increased from about 99 to 116 mmHg. Thus, a large portion of the external pressure was absorbed under pressure equalization, resulting in low stress on the arterial wall

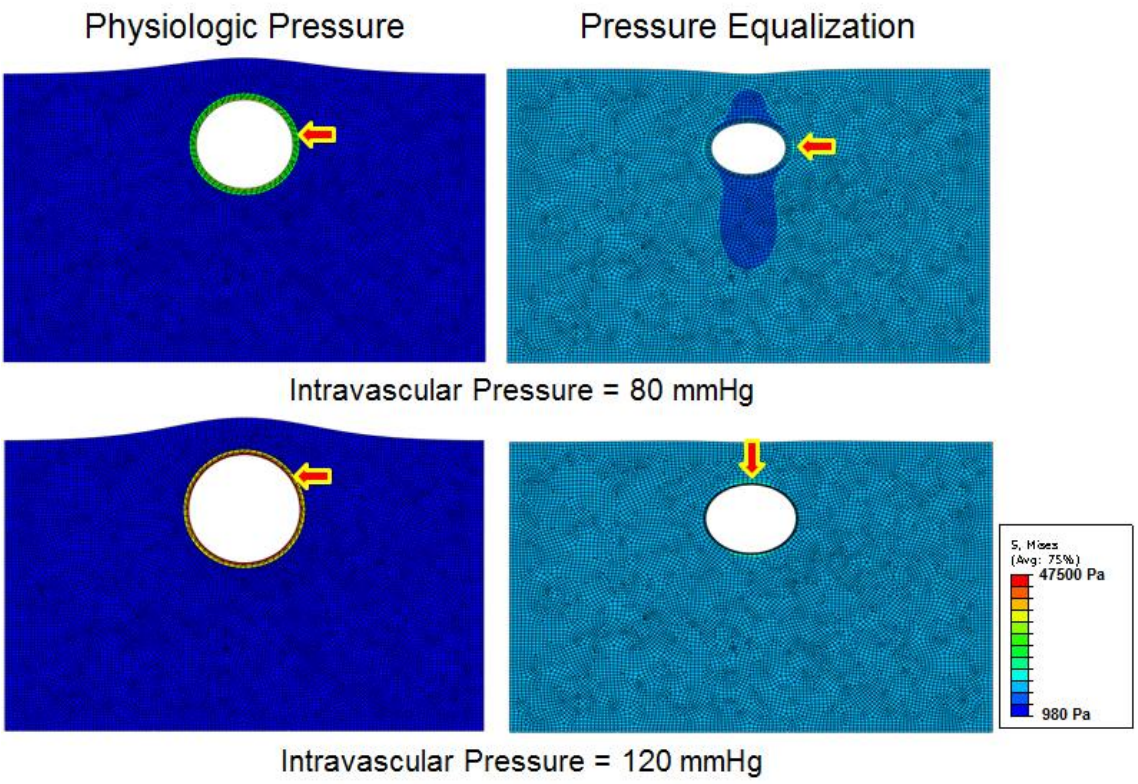


Figure 2-7. The stress distribution of the artery model with surrounding tissue (FEA1) under either physiologic pressure or pressure equalization. The arrows point to high-stress regions.

## 2.4 Discussion

High-resolution ultrasound with speckle-tracking algorithms can accurately and precisely measure the motion and mechanical strain of subsurface structures and tissues such as arteries and other vessels. This noninvasive imaging technique has the clinical potential to distinguish subtle changes in arterial mechanics.

However, the arterial wall is a highly nonlinear elastic medium that undergoes little deformation when the artery is distended under normal physiologic loading. The small amount of arterial strain produced under physiologic pressure limits the range of possible measurements by elasticity imaging to characterize stiffness fully. However, previous ultrasound imaging research (14, 47) has demonstrated that this limitation can be overcome by applying external pressure to lower the mean arterial pressure (MAP) that produces the low effective elastic modulus, and therefore higher radial strain, in the vessel wall. Reducing MAP decreases preload or transmural pressure and allows the arterial pulse pressure to produce much larger strain. Use of the pressure equalization technique therefore expands the dynamic range of potential strain measurements.

Previous estimates of peripheral artery strain under pressure equalization have relied on the Young's modulus of only the artery (14). We sought to investigate the effect of surrounding tissue in ultrasound elasticity measurements by comparing strain results from imaging to those of two FEA models, one employing the modulus of only artery (FEA2) and one employing the moduli of both artery and surrounding tissue (FEA1). The ultrasound and FEA strain measurements differ little under physiologic pressure. Under pressure equalization, however, the strain levels predicted by the FEA2 model are substantially greater than the levels measured by both imaging and the FEA1 model, which are relatively similar. Therefore, surrounding tissue appears to have a significant effect on arterial strain and should not be ignored in models of strain under pressure equalization. One possible hypothesis for this effect could be the relationship between the Young's moduli of the two tissues under physiologic and pressure equalization states. By evaluating Figure 2-4 and Table 2-1, it can be seen that under physiologic pressures the Young's modulus of the arterial wall is significantly greater than that of the surrounding tissue (about 8×). This means that the elasticity of the artery is

predominantly responsible for balancing the expansion force produced due to the blood pressure. However, if we consider the pressure equalization state it can be seen that the Young's modulus of the surrounding tissue is approximately 3× that of the artery wall. This means that the surrounding tissue is playing a far greater role in balancing the force due to the pressure in the artery. This relationship can be clearly seen in Figure 2-6(a) and (b), by comparing the FEA1 (with surrounding tissue) and FEA2 (no surrounding tissue) graphs for physiologic pressures and pressure equalization. In both cases, higher strain values are obtained when no surrounding tissue is present. Under physiologic pressures we would not expect to see a great difference between the FEA1 and FEA2 results. However, under pressure equalization we see much higher strain (deformation) when no surrounding tissue is present in the simulation.

A limitation of this study is the use of only one human subject for the collection of ultrasound data. The ultrasound apparatus and method of data collection were considered too experimental and impractical for use in a larger clinical investigation. The preliminary findings of the comparison of the ultrasound and FEA elasticity analyses reported here warrant further development of an ultrasound apparatus that is suitable for use in a larger clinical study.

## 2.5 Conclusions

Prior studies have made important contributions to our understanding of arterial compliance. Ultrasound speckle tracking has advanced our understanding by allowing high-resolution measurements. Provocative maneuvers are being developed to increase our understanding of tissue mechanics. These results indicate the use of strain information as a diagnostic tool may need to include the effects of surrounding tissue mechanics, especially when maneuvers such as pressure equalization are used to enhance the dynamic range of elasticity imaging.

# Chapter 3 Quantification of Flow Velocity and Edge Velocity Gradient from Ultrasound Radio Frequency Signals

## 3.1 Introduction

The blood flow velocity profile is important for diagnosis of cardiovascular diseases, which are associated with abnormal blood flow in arteries due to hemodynamic changes of patients (28). The blood flow velocity gradient at the wall edge has been utilized to estimate the vascular wall shear stress, which has a key role in vascular physiology as well as the pathophysiology of vascular diseases (51). Based on Poiseuille theory, the blood flow velocity profile is parabolic and high velocity gradients occur at the vascular wall in steady-state and fully developed laminar flow in normal conduit vessels (52). In areas with vascular tortuosity, branching, and the presence of vascular plaque, the blood flow velocity profile is non-parabolic (28). Ultrasound has been the preferred non-invasive technique to measure the blood flow velocity profile.

Multi-gate Doppler ultrasound measurement has been applied to estimate the blood flow velocity in vessels (16). Using multi-gate Doppler measurements, the blood flow velocity profile and blood flow velocity gradient at the wall edge were determined from longitudinal views of blood vessels (17, 18, 21, 22). However, multi-gate Doppler ultrasound estimates of blood flow are based on 1D velocity measurements, which depend on the assumptions that the lumen is circular and that the flow is symmetrical in the out-of-plane directions, both of which are violated in the presence of vascular tortuosity and branching (16).

To measure the 2D flow velocity, the tracking of ultrasound RF signals has been also utilized to study the blood flow velocity profile. Using correlation based lateral speckle tracking, blood flow velocity profiles have been measured from longitudinal views of blood vessels (23-27). Blood flow velocity profiles have been quantified using the correlation based lateral speckle tracking, but B-mode image acquisitions of longitudinal

views of blood vessels were limited by vascular tortuosity and branching (28). To overcome these limitations, transverse views of blood vessels were used to measure blood velocity profiles. For transverse views of blood vessels, the decorrelation of ultrasound RF signals along 1D A-line and in 2D B-mode images have been applied to the study of blood velocity profiles. Using the decorrelation of ultrasound RF signals, the vessel wall interface could be detected (29) and blood flow velocity profile was qualitatively identified (30). The blood flow velocity profile measurement using the decorrelation of ultrasound RF signals from A-lines has been demonstrated, but the quantification of blood flow velocity was not achieved.

RF signals of 2D B-mode images were used to determine the blood flow profiles in transverse views of a vessel. Bamber et al. (31) demonstrated that decorrelation could be used to identify blood flow using the time rate-of-change of correlation in B-mode images. Li et al. (32) has theoretically demonstrated the linear decrease of correlation according to elevational speckle movement. Speckle decorrelation has been used to measure the motion of transducer to produce 3D ultrasound images (32-35). This technique has been applied by Rubin et al. (36) to qualitatively identify the blood flow profile in both in-vitro flow phantom and *in-vivo* animal studies. Rubin et al. (37) also used the Doppler flow measurements to improve the accuracy of volumetric flow from the decorrelation based flow profiles and theoretically modeled exponential decrease of correlation according to elevational speckle movement. Previous research demonstrated that speckle decorrelation could generate flow velocity profiles, but the decorrelation was not experimentally measured. The first goal of this research is to estimate flow profiles using speckle decorrelation due to elevational motion in tissue-mimicking phantoms. Speckle decorrelation can be used to measure velocity profiles because when blood particles travel through an ultrasound imaging plane, the received echo signals decorrelate at a rate that is related to the flow velocity (50, 53-55). To achieve this goal, the transducer is moved at a series of constant velocities across a tissue-mimicking phantom. The relationship between speckle (transducer) velocity and beam-to-beam correlation as a function of position along beam is obtained. This calibration function can then be used to calculate velocity from a 2D transverse image given a specific observed decorrelation.

A second goal of this research is to determine the edge of vascular walls and the velocity gradients at the edge using the speckle decorrelation approach. The wall edge is determined using both the B-mode image and $2^{nd}$ order gradient of the flow velocity profile at the wall edge. The accuracy of the ultrasound measured flow velocity profile and the velocity gradient are evaluated by comparison with the parabolic velocity profile based on Poiseuille theory.

The third goal of this research is to compare the transverse decorrelation based-, and lateral speckle tracking flow velocity profiles. For lateral speckle tracking flow velocity measurement, the ultrasound RF signals of B-mode image are acquired from longitudinal views of the hole in the flow phantom through which blood mimicking fluid is flowing. The speckle movement is determined using correlation based lateral speckle tracking. The flow velocity is obtained by multiplying the speckle movement in two consecutive frames by the acoustic frame rate. The wall edge is also determined using both B-mode image and 2nd order gradient of the flow velocity profile. The velocity gradient is measured at the wall edge from the flow velocity profile. The flow velocity profile and the velocity gradient are compared with the decorrelation flow velocity profile and velocity gradient.

## 3.2 Materials and Methods

To obtain the data required to achieve the three goals, two experiments were performed: 1) speckle decorrelation measurement using tissue-mimicking phantom with a linear rail system and 2) *in-vitro* flow measurement using blood mimicking fluid with a flow phantom. Two methods, decorrelation based transverse velocity estimation and lateral speckle tracking velocity estimation, were used to measure the flow velocity profile and the velocity gradient at the wall edge. For the decorrelation based velocity estimation, the experimental setup shown in Figure 3-1 was used to obtain the calibration data and the setup shown in Figure 3-4 was used to obtain the flow data.

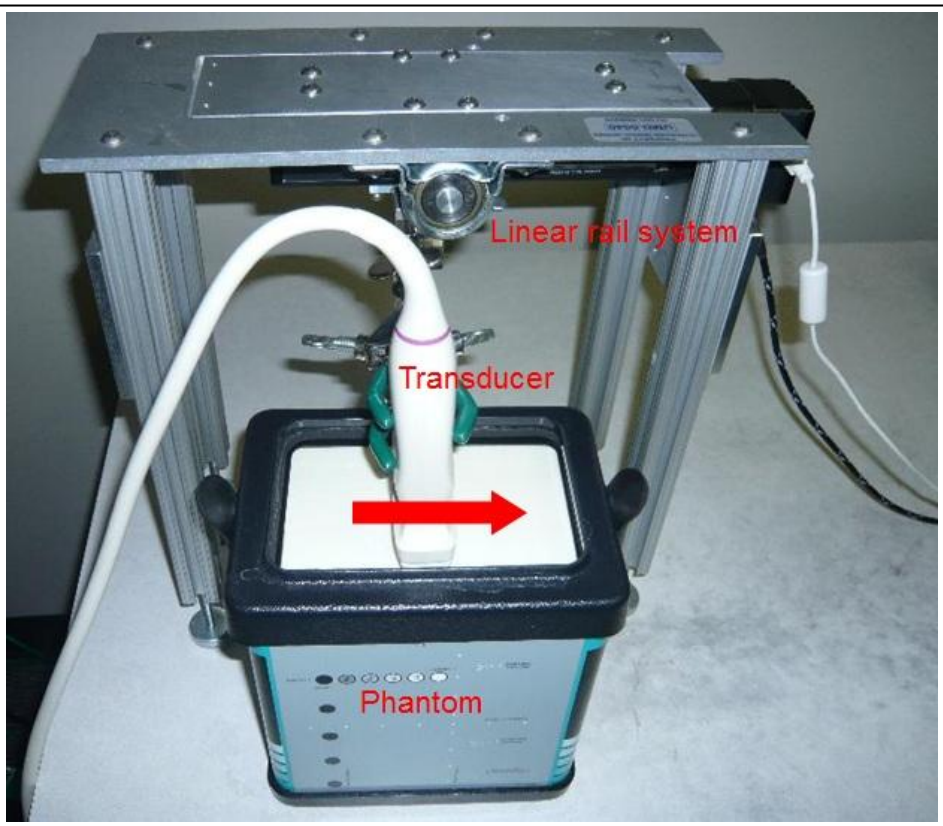


Figure 3-1. The linear rail system and the tissue mimicking phantom.

The first experimental setup for speckle decorrelation measurement, as shown in Figure 3-1, consists of a tissue-mimicking phantom, a stepper-motor driven linear rail system and an ultrasound transducer. The tissue-mimicking phantom contains scatterers producing fully developed speckle. The linear rail system (Epsilon Imaging, Ann Arbor,

Michigan, USA) generates speckle movement by moving an ultrasound transducer with desired velocity over the surface of a tissue-mimicking phantom.

The ultrasound transducer (model L12-5 scanner, Epsilon Imaging, Ann Arbor, Michigan, USA) with a 9-MHz linear array acquires series of 19.5 mm × 24.9 mm B-mode image, which consists of 0.09 × 0.09 mm pixels, with incremental spacing in the elevational direction over a tissue-mimicking phantom. A 7 × 8 grid of region of interest (ROI) is chosen in the B-mode image (Figure 3-2). Each ROI has 30 × 30 pixels, which is the sample number adequate to show consistent correlation values. The size of ROI is 2.72 × 2.73 mm, which has sufficient speckles to perform the speckle decorrelation. The software EchoInsight™ (Epsilon Imaging, Ann Arbor, Michigan, USA) executes the finite impulse response (FIR) high pass filtering and a 2D speckle tracking, which has a 5 by 3-pixel kernel and a 9 by 5-pixel filter, for the B-mode images. The FIR high pass filtering, which subtracts RF-signals of two intervals of frames, is applied for the B-mode RF-signals to suppress the reverberation noise and enhance the variation of RF-signals between frames and the accuracy of wall edge detection.

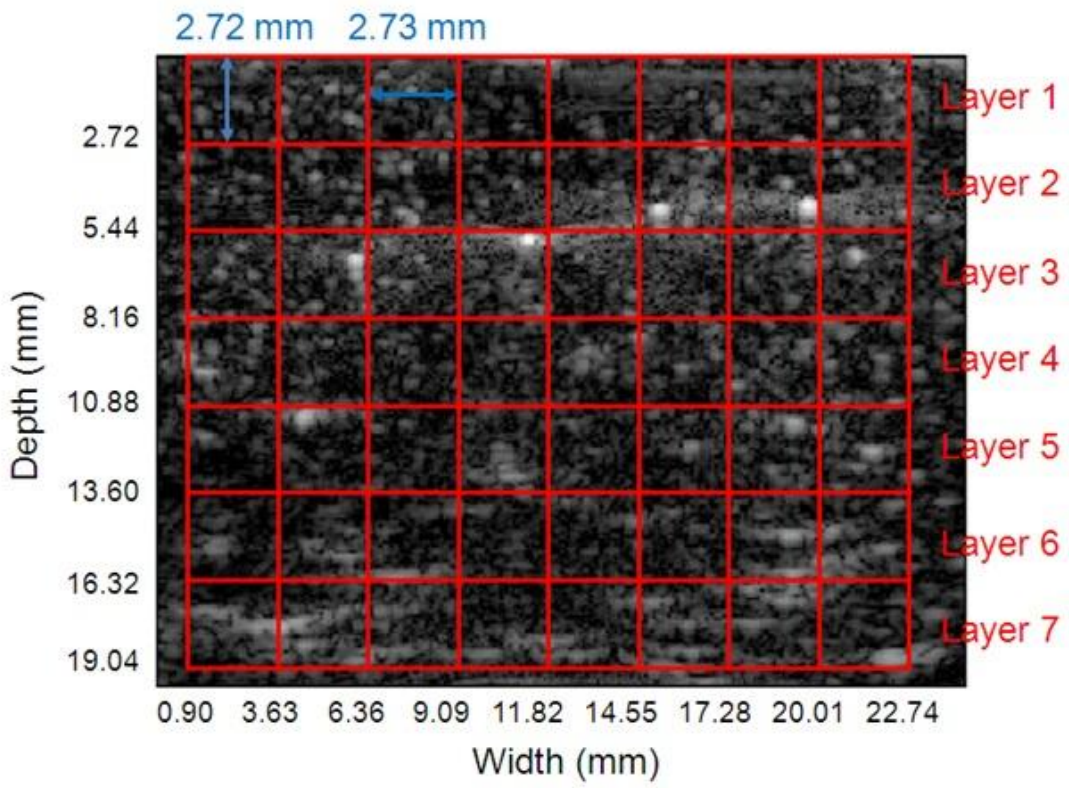


Figure 3-2. B-mode image of the tissue mimicking phantom and the 7 by 8 grid region of interest (ROI).

Figure 3-3(a) shows the beam correlation width, elevational speckle velocity and speckle decorrelation in the phantom speckle decorrelation measurement. The beam correlation width is defined as full width at half maximum (FWHM) of the correlation versus speckle movement curve, as illustrated in Figure 3-3(b) (56). The beam correlation width determines the maximum flow velocity that can be measured. When the speckle movement during time interval between two consecutive firings of the transducer exceeds the beam correlation width, complete loss of speckle tracking occurs (37). This limits the maximum flow velocity that can be measured using the decorrelation based method and will be evident later in the Results and Discussions sections. In addition, the beam correlation width versus depth determines the ultrasound beam profile, which can qualitatively validate the proposed method.

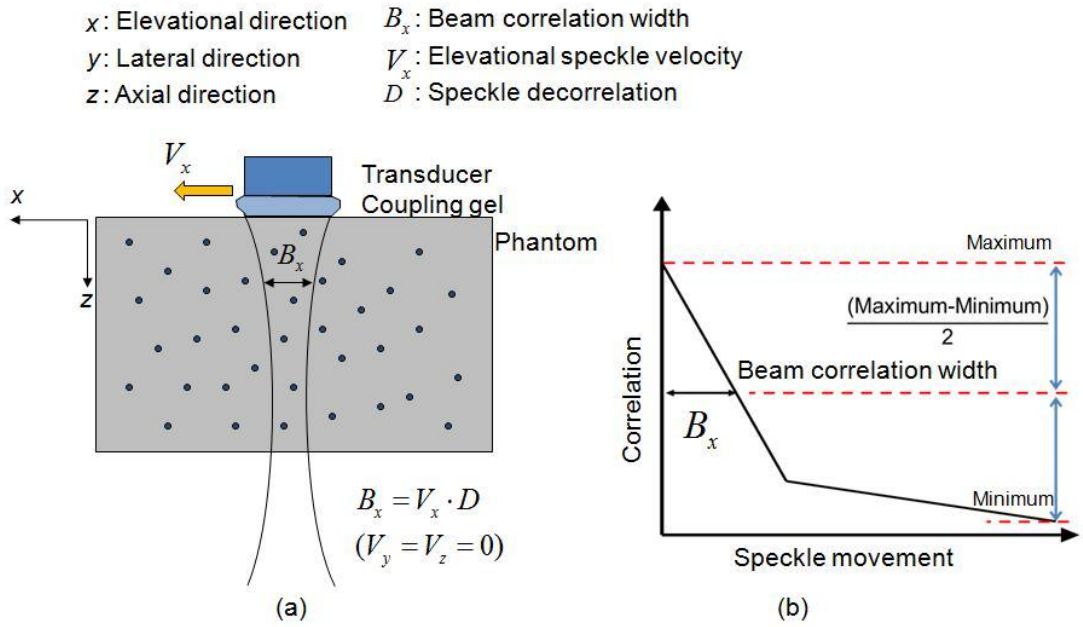


Figure 3-3. (a) The definition of directions, beam correlation width, elevational speckle velocity and speckle decorrelation in the phantom. (b) The anticipated speckle movement versus correlation curve and the beam correlation width of the curve.

For the first experimental setup (Figure 3-1), 47 frames of B-mode images were acquired by moving the ultrasound transducer with a 0.044 mm step size at 0.1 s per step over the phantom using the linear rail system. 2D speckle motion tracking was performed for the B-mode images by increasing the lag, which is the frame-to-frame increment, from 1 to 46. A 7 × 8 grid of region of interest (ROI) was chosen in the B-mode image (Figure 3-2). The mean and standard error (SE) of the speckle movement versus correlation curves were obtained for each depth of the seven layers from the B-mode image (Figure 3-2).

The second experimental setup for *in-vitro* flow measurement consists of a peristaltic pump, a graduated cylinder, a flow phantom and an ultrasound transducer, as shown in Figure 3-4. The peristaltic pump (Barnant, Barrington, IL, USA) injects a fluid mixture, which consists of water and glycerine in the ratio of 5:1 and has plastic particles with 30 ± 3 μm diameter at a concentration of $1.7\times10^4$ particles/cc (ATS Laboratories,

Bridgeport, CT, USA) to increase the backscatter signal. Mean volume flow rates of 50, 100, 150, 200, 250, 500, and 1000 ml/min, within the range of human blood flow rate between 1 to 1000 ml/min (57) were studied. The mean volume flow rate is measured using a graduated cylinder. The flow phantom (Model 525, ATS laboratories, Bridgeport, CT, USA), made of tissue-mimicking urethane rubber, has 5.5 mm diameter hole as the flow path.

In the second experimental setup (Figure 3-4), 700 B-mode frames were acquired at an acoustic frame rate of 348 Hz from the transverse view of the hole in the flow phantom. The correlation map was computed as a function of time for the flow phantom with the fluid mixture flowing at specific velocities. The correlation map of the flow phantom was used to determine the decorrelation rate corresponding to the fluid motion. Because the differences in speeds of sound, 1390-1500 m/s for the tissue-mimicking phantom in Figure 3-1 (58), 1555-1587 m/s for the fluid mixture (based on data provided by the manufacturer, ATS) and 1450 m/s for flow phantom (59), are small, their contributions to any errors in the estimates will be small. The decorrelation of the fluid mixture and the average speckle movement versus correlation curves determined from the first experiment were used to measure the speckle displacement. The speckle movement in two consecutive frames was multiplied by the frame rate to determine the flow velocity. Using an averaged correlation map from the complete 700 frame set, the flow velocity profile was obtained for the circular cross-section of the hole inside the flow phantom. This flow velocity profile was used to determine the velocity gradient at the wall edge using linear regression.

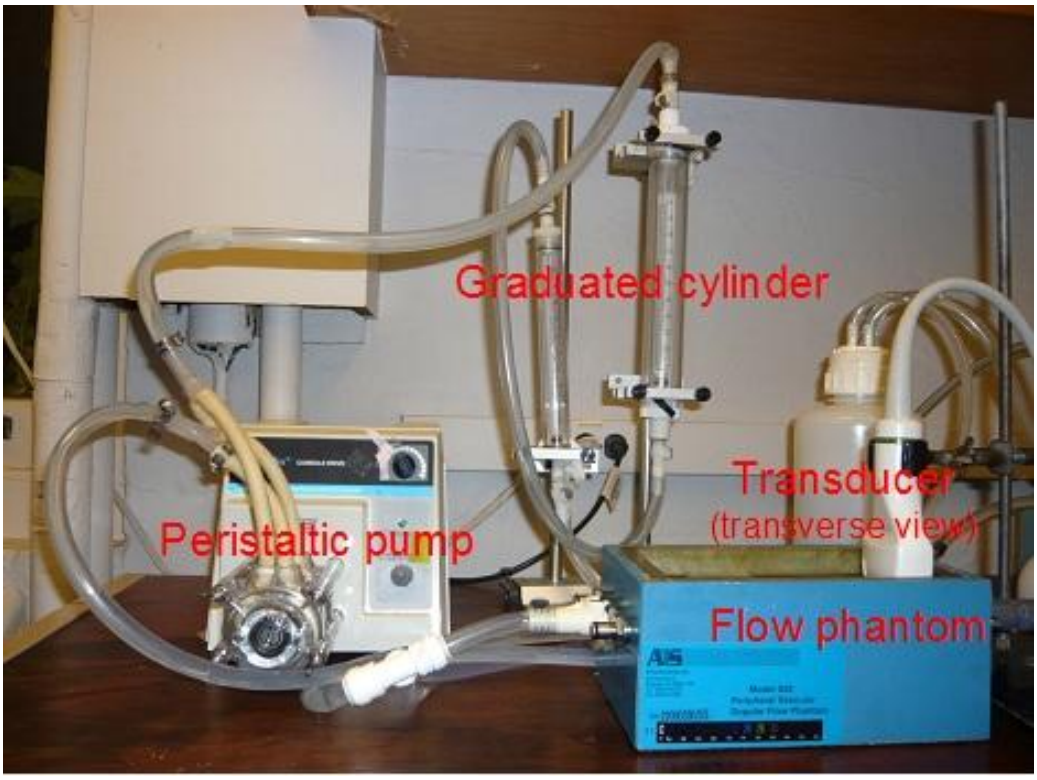


Figure 3-4. The graduated cylinder, peristaltic pump and flow phantom.

For lateral speckle tracking velocity estimation, the second experimental setup (Figure 3-4) was utilized to measure the flow velocity from the longitudinal view of the flow phantom. 917 B-mode frames were acquired using a 426 Hz frame rate to obtain the lateral velocity map of the fluid mixture flowing at a specific velocity.

Using an averaged lateral velocity map from the entire range of 917 frames, the flow velocity profile was obtained for the longitudinal cross section of the hole in the flow phantom with the flowing fluid mixture. Similarly, the velocity gradient at the wall edge was determined from this flow velocity profile using a linear regression estimate assuming that the flow is zero at the wall.

The wall edges were determined using the B-mode image and the 2$^{nd}$ order spatial derivative, gradient, of the flow velocity profile. In the B-mode image, pixels in the vicinity of wall edges were identified from the brightness change of gray scale pixels due to acoustic impedance change between the tissue mimicking phantom and the fluid

mixture (60). Among these pixels, the wall edges were determined by the highest value of the 2nd order gradient of the velocity profile. Figure 3-5(a) shows the theoretical parabolic velocity profile for laminar flow in a circular tube. The 1st and 2nd order gradient of the parabolic velocity profiles are shown in Figure 3-5(b) and (c), respectively. For the 1st order gradient of the velocity profile, discontinuity was occurred at the wall edges. For the 2nd order gradient of the velocity profile, an infinite value ($+\infty$) was generated at the wall edges. The sites/pixels with the maximum values of the 2nd order gradient of the velocity profile were identified as the wall edges.

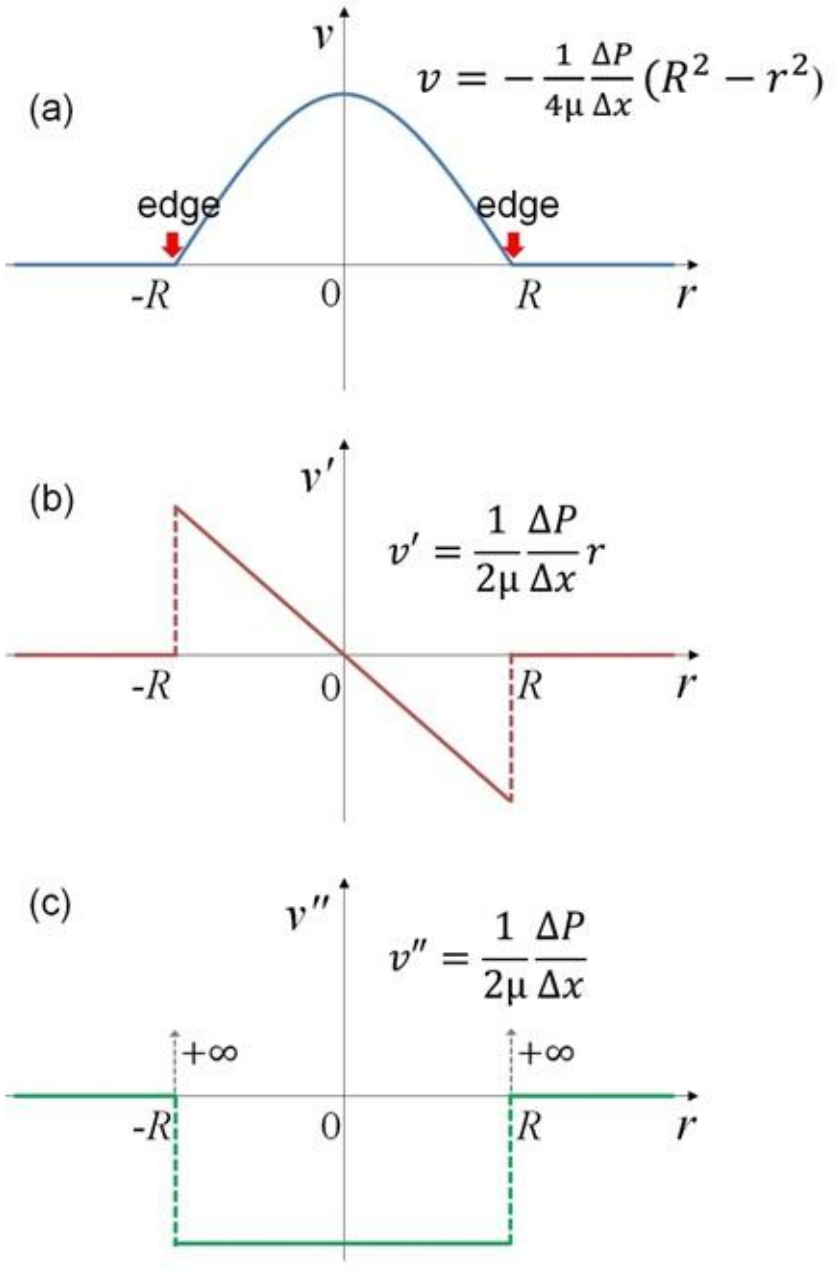


Figure 3-5. (a) Theoretical parabolic velocity curve and (b) the 1st and (c) 2nd order gradient of the velocity curve. $v$: velocity, $\mu$: dynamic viscosity, $v'$: 1st gradient of velocity, $v''$: 2nd gradient of velocity, $R$: radius of the hole, $r$: distance from the center, $\Delta P$: pressure difference, $\Delta x$: distance in direction of flow, $\frac{\Delta x}{\Delta P}$ <0 is constant.

## 3.3 Results

### 3.3.1 *Decorrelation based flow velocity profile measurement and edge detection*

Figure 3-6 shows the average and SE of the speckle movement versus correlation curves for 7 layers. The correlation coefficient and the speckle movement represent a normalized covariance and the elevational displacement of speckle through the beam, respectively. The depth is defined from the top surface of the phantom with the transducer in the position for the transverse view.

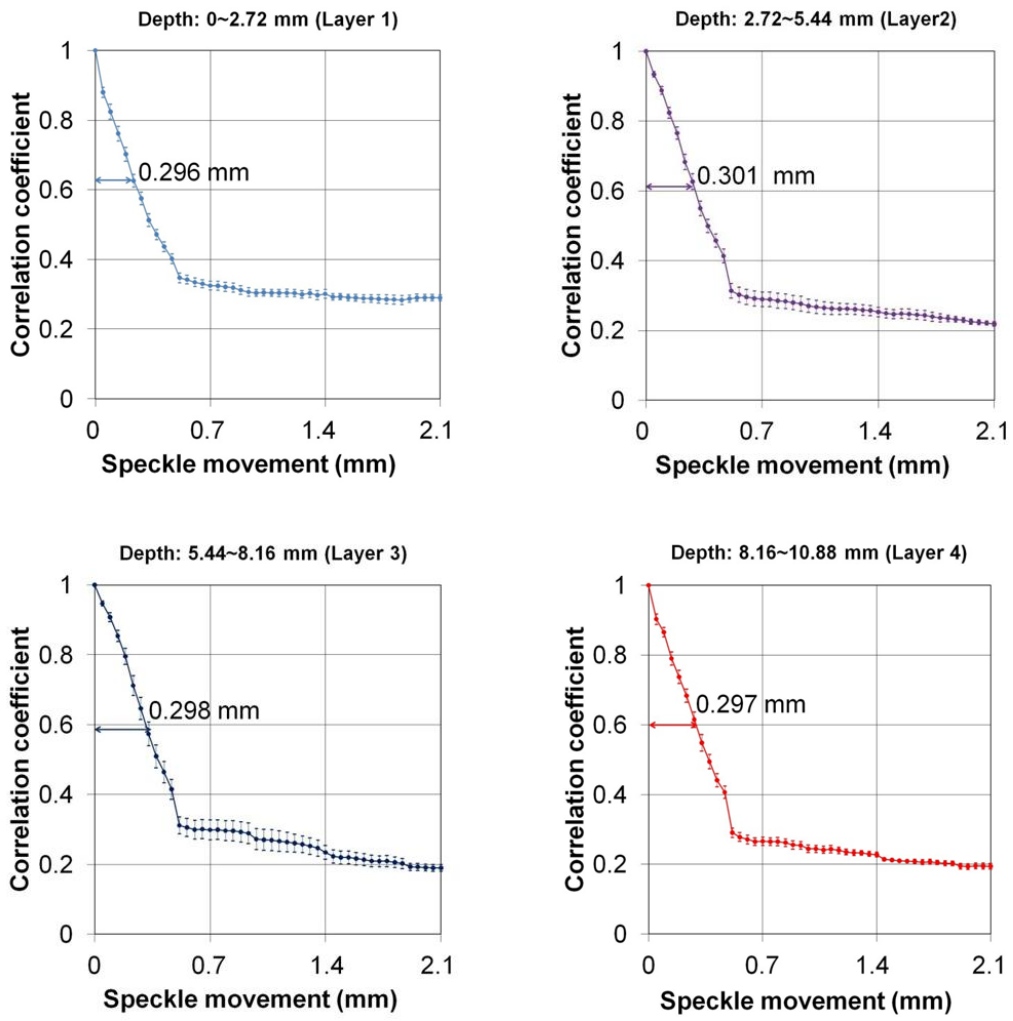


Figure 3-6. Average and standard error (SE) of speckle movement versus correlation curves from 8 ROIs in 7 layers each measuring 2.72 mm in height.

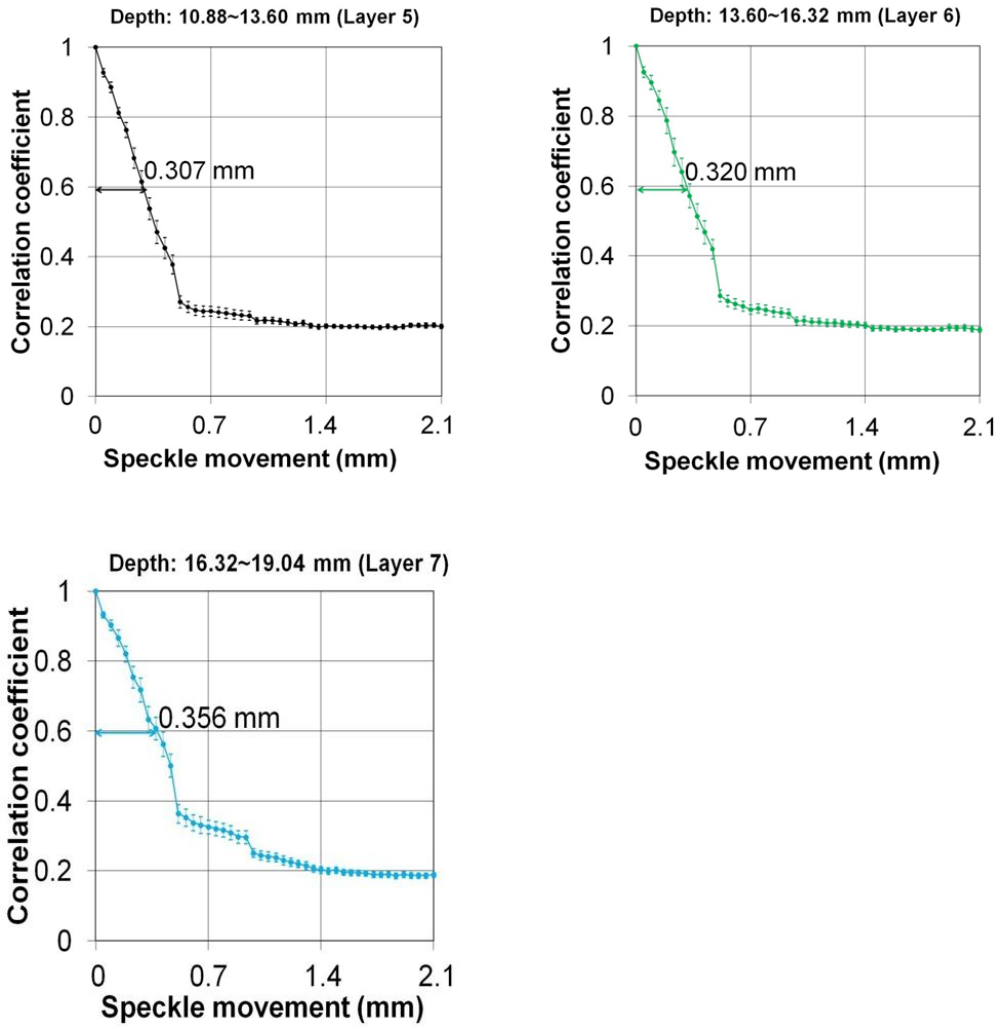


Figure 3-6 (cont.). Average and standard error (SE) of speckle movement versus correlation curves from 8 ROIs in 7 layers each measuring 2.72 mm in height.

For the depth from 0 to 2.72 mm, the correlation coefficient sharply and linearly decreased from 1.0 to 0.34 with the speckle movement from 0 to 0.5 mm. Beyond 0.5 mm speckle movement, the correlation coefficient decreased slowly from 0.34 to 0.29. The beam correlation width, determined at FWHM of the average speckle movement versus correlation curve, was 0.296 mm in this layer. For the next layer with depth from 2.72 to 5.44 mm, the correlation coefficient also sharply and linearly decreased from 1.0 to 0.31 with the speckle movement from 0 to 0.5 mm. The correlation coefficient then slowly decreased to 0.22 at 2.1 mm speckle movement. The beam correlation width

increased to 0.301 mm in this layer. Similar patterns of sharp and linear decrease in correlation coefficient from 1.0 to 0.3 about 0.5 mm speckle movement and followed by a transition to slow decrease repeated in the following five layers. The linear decrease of the correlation coefficient versus speckle movement was proposed by Li et al. (32) and observed in all layers. The beam correlation width was approximately 0.30 mm in the top four layers (depth from 0 to 10.88 mm) and steadily increased to 0.36 mm in deeper layers (depth from 10.88 to 19.04 mm). The divergence of the beam correlation width was observed.

The measurement of beam correlation width was repeated four times. Figure 3-7 shows the average and SE of the four beam correlation width measurements versus depth. The average beam correlation width was represented as the solid circle with different colors for each layer. The SE of beam correlation width was the distance between the solid circle and the open cross symbol on both sides of the average.

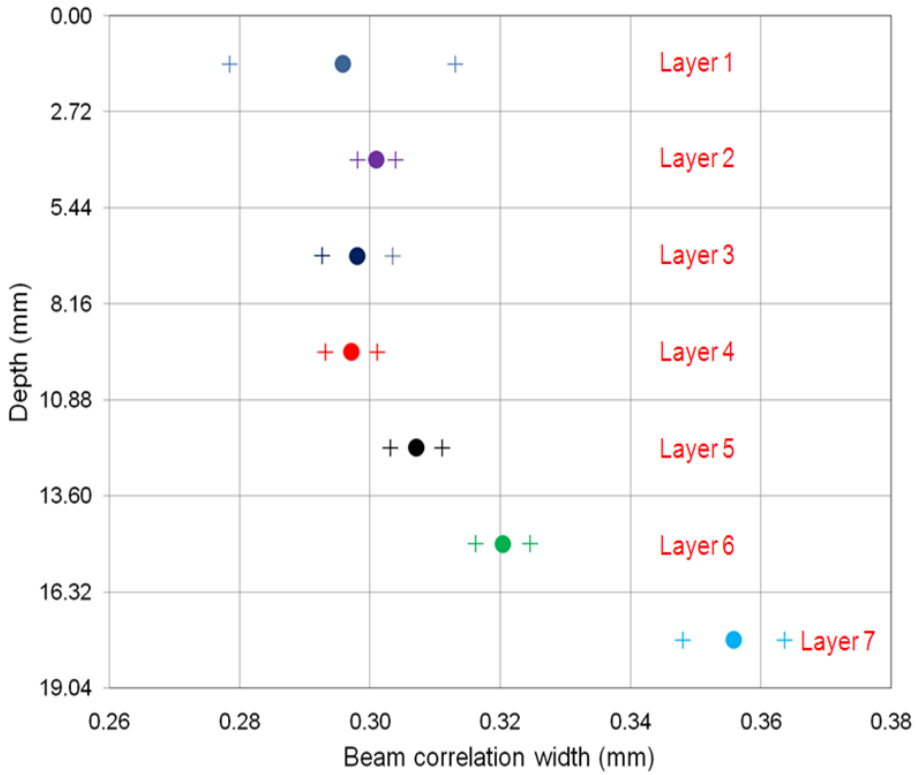


Figure 3-7. Average and standard error (SE) of beam correlation width versus depth.

The top layer had large variation of the measurement with the highest SE of the beam correlation width (0.017 mm). Layers 2, 3, and 4 had consistent beam correlation width measurements with low SE (0.003 to 0.005 mm) and showed gradual convergence of ultrasound beam correlation width to the lowest value of 0.297 mm in Layer 4. The ultrasound beam then gradually diverged from Layers 5 to 7. This convergence and divergence of beam correlation width versus depth has been proposed by Shung (60) and qualitatively validated the measurement and analysis.

Speckle movement versus correlation curves were applied to quantify the flow velocity using 2D speckle tracking of the flow phantom with fluid mixture flowing at mean volume flow rate of 100 ml/min using the second experimental setup (Figure 3-4). Figure 3-8(a) shows the B-mode image of the transverse view of the hole with the fluid mixture in the flow phantom. A total of 700 consecutive B-mode frames were acquired in 2.01 s. 2D motion estimation was performed for the 700 frames by correlating adjacent frames (one lag) to generate 699 correlation maps. In each pixel, the correlation coefficient in these 699 correlation maps was averaged to obtain the averaged correlation map as shown in Figure 3-8(b).

A line, denoted as a-a, was selected across the center of the hole in the averaged correlation map (Figure 3-8(b)). The correlation coefficient of the pixels along the a-a line was obtained five times under the same (100 ml/min) volume flow rate. The average and SE of correlation coefficients along the a-a line are shown in Figure 3-9 for the 100 as well as 50, 150 and 200 ml/min flow rate, each also has five measurements using the B-mode transverse view of the hole in the flow phantom. The correlation coefficient of pixels in the a-a line was 1.0 up to about 6.6 mm, the depth of the top edge of the hole. Inside the hole, the correlation coefficient gradually dropped to a minimum value in the middle of the hole where the flow velocity was the highest and then increased back to 1.0 at the bottom edge of the hole. The change of correlation coefficient across the hole demonstrated the feasibility to use the correlation coefficient to estimate the flow velocity profile, as proposed by Rubin et al. (36). The minimum average correlation coefficient for 50, 100, 150 and 200 ml/min volume flow rate was 0.92, 0.72, 0.65 and 0.56, respectively. A high flow rate generated a lower minimum average correlation coefficient, which was also observed by (36).

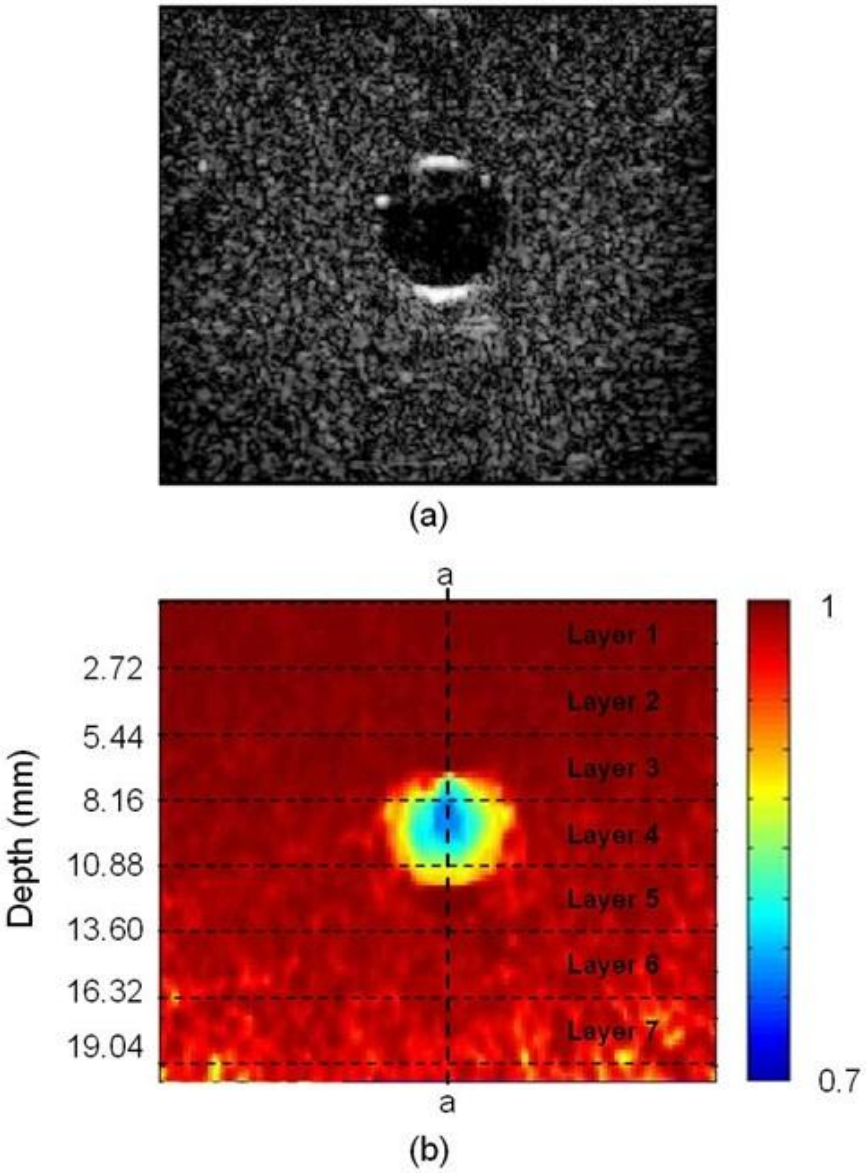


Figure 3-8. (a) B-mode image and (b) correlation map of the transverse view of the hole with the fluid mixture flowing at mean volume flow rate of 100 ml/min in the flow phantom.

To quantify the flow velocity using the correlation coefficient, the depth along the a-a line was divided into seven layers each measuring 2.72 mm in height similar to the speckle decorrelation measurement (Figure 3-2). These seven layers are shown in Figure 3-9. In each layer, the value of correlation coefficient in the a-a line was used to find the amount of speckle movement in two consecutive frames based on the average speckle

movement versus correlation curves in Figure 3-6. The speckle movement in the fluid mixture was determined from Layers 3, 4 and 5, the location of the hole in the flow phantom. The speckle movement in two consecutive frames was multiplied by the acoustic frame rate (348 Hz) to estimate the flow velocity.

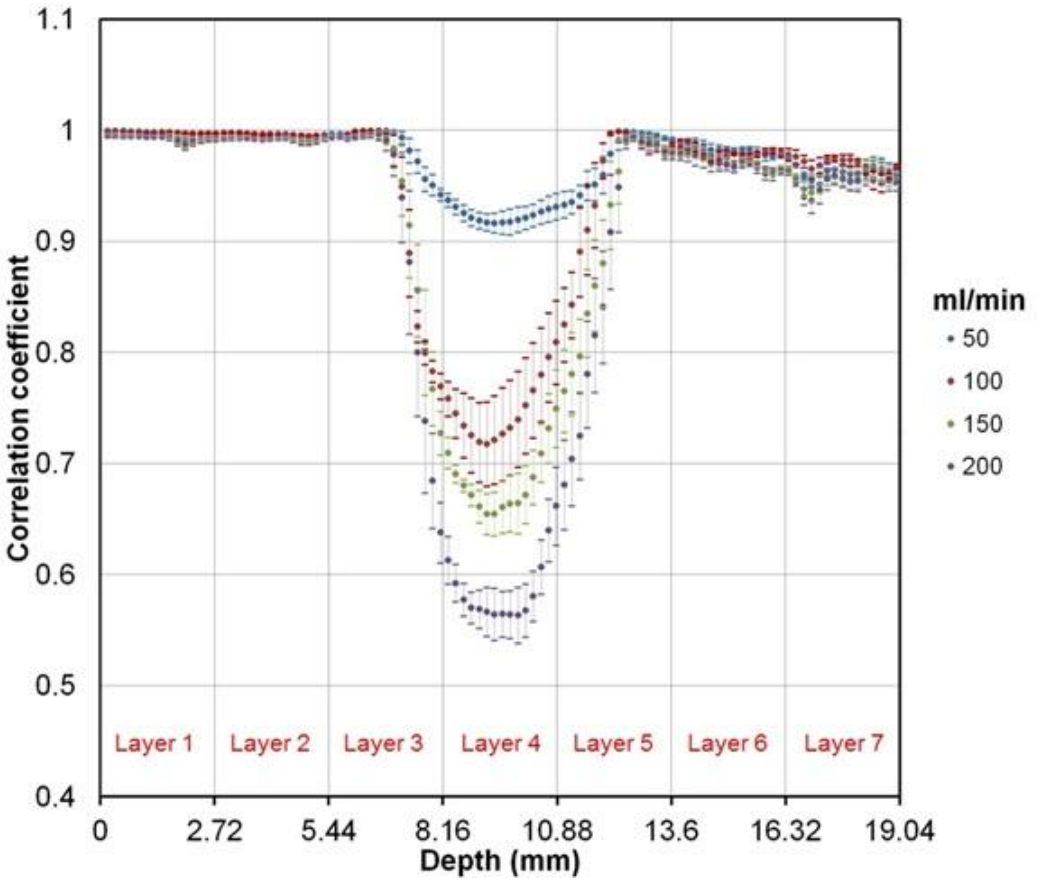


Figure 3-9. Average and standard error (SE) of the depth versus correlation coefficient curves from the line a-a for 50, 100, 150 and 200 ml/min volume flow rate.

The open square symbol in Figure 3-10 shows the velocity profile estimated using the decorrelation based flow velocity measurement method at 50, 100, 150 and 200 ml/min volume flow rate. The theoretical (parabolic) velocity profiles, which are represented by solid lines, are also presented for comparison. Near the top and bottom edges, the trend of sharp increase of flow velocity was the same for both the decorrelation based flow velocity profile and the theoretical velocity profile. This demonstrated the feasibility of

the decorrelation based flow velocity measurement method to estimate the flow velocity gradient at the edge (not the whole velocity profile) of the hole. In the middle of the hole, the decorrelation based flow velocity measurement underestimated the flow velocity because the speckle movement during time interval (0.003 s) between two consecutive firings of the transducer was larger than the beam correlation width. This phenomenon has been observed by Rubin et al. (37).

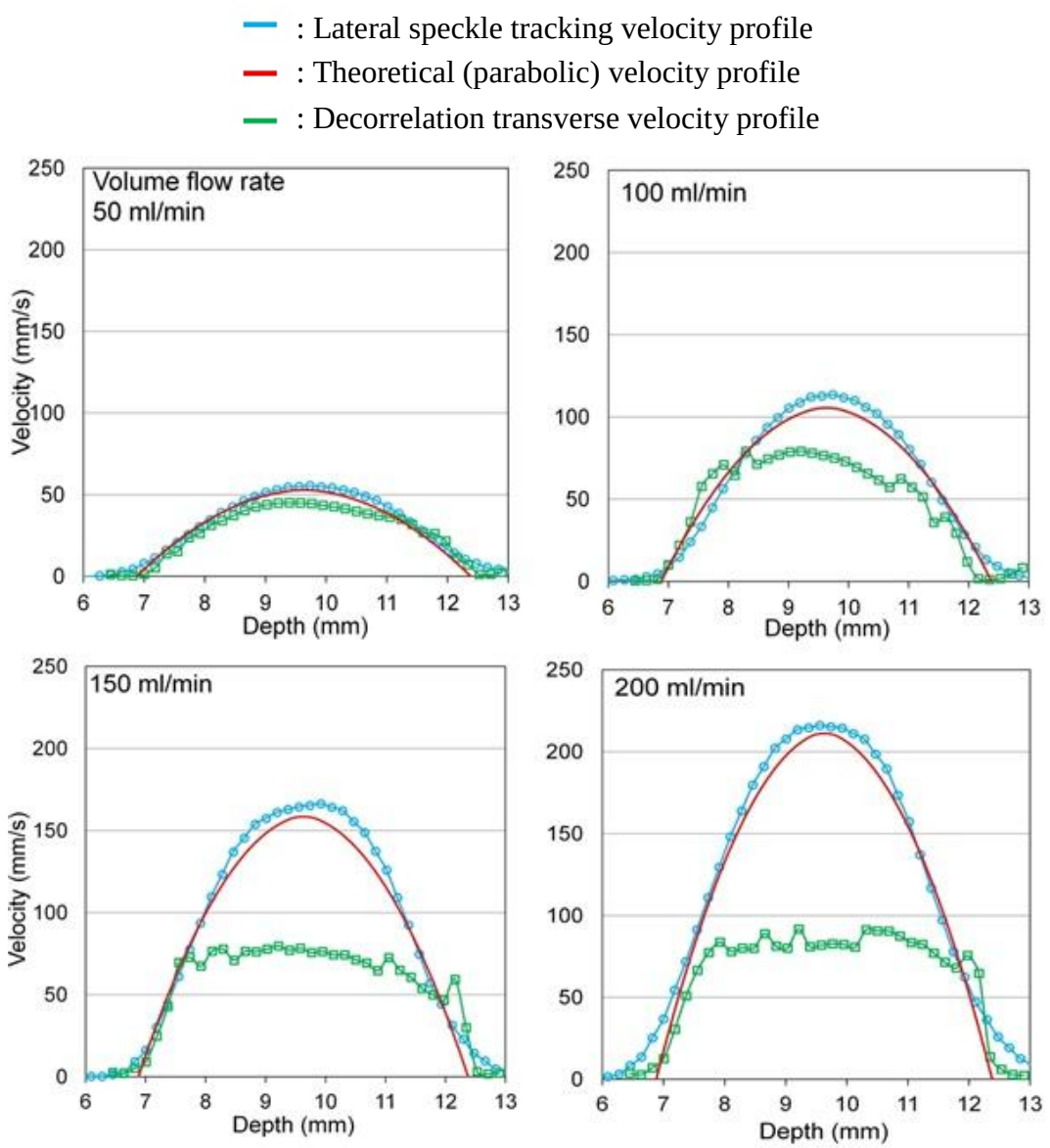


Figure 3-10. Flow velocity profiles across a center of a cross section of the hole in the flow phantom at mean volume flow rate of 50, 100, 150 and 200 ml/min. The correlation based lateral speckle tracking velocity profile was translated to the depth from 6 to 13 mm for comparison.

The top and bottom wall edges were determined using the edge detection method based on the 2nd order gradient of the velocity profile. Figure 3-11(a) shows the B-mode image of the transverse view of the hole with the fluid mixture flowing at 100 ml/min volume flow rate. The a-a line across the top and bottom edge and center of the hole is marked. Closed-up views of pixels in the hole and near the top and bottom edges as well

as the a-a line are shown in Figure 3-11(b). Four pixels near the top edge, denoted as T1, T2, T3 and T4, were identified based on the transition of grey scale at depth of 6.45, 6.63, 6.82 and 7.00 mm.

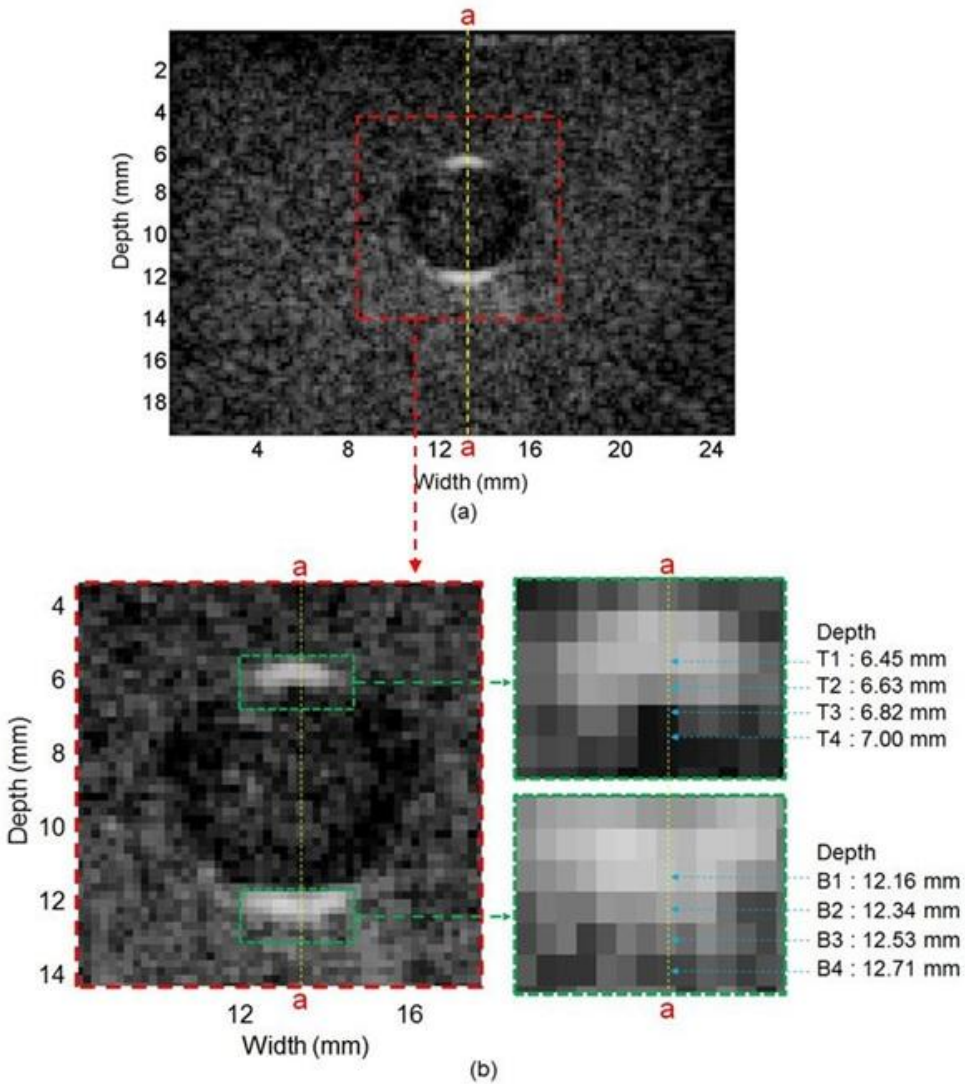


Figure 3-11. (a) B-mode image of the transverse view of the hole with the fluid mixture flowing at 100 ml/min volume flow rate and (b) closed-up views of pixels in the hole and near the top and bottom edges as well as the a-a line.

The 2nd order gradient at T1, T2, T3 and T4 and adjacent pixels along the a-a line was determined and shown in Figure 3-12(b) for 100 ml/min volume flow rate. The pixel T3 had the highest 2nd order gradient (243 $mm^{-1}s^{-1}$) among four pixels and was determined as the top edge. It is noted that pixels around T1 and T4 could have higher

value of 2nd order gradient but not be considered as the wall edge because they are not in the group of pixels were originally selected.

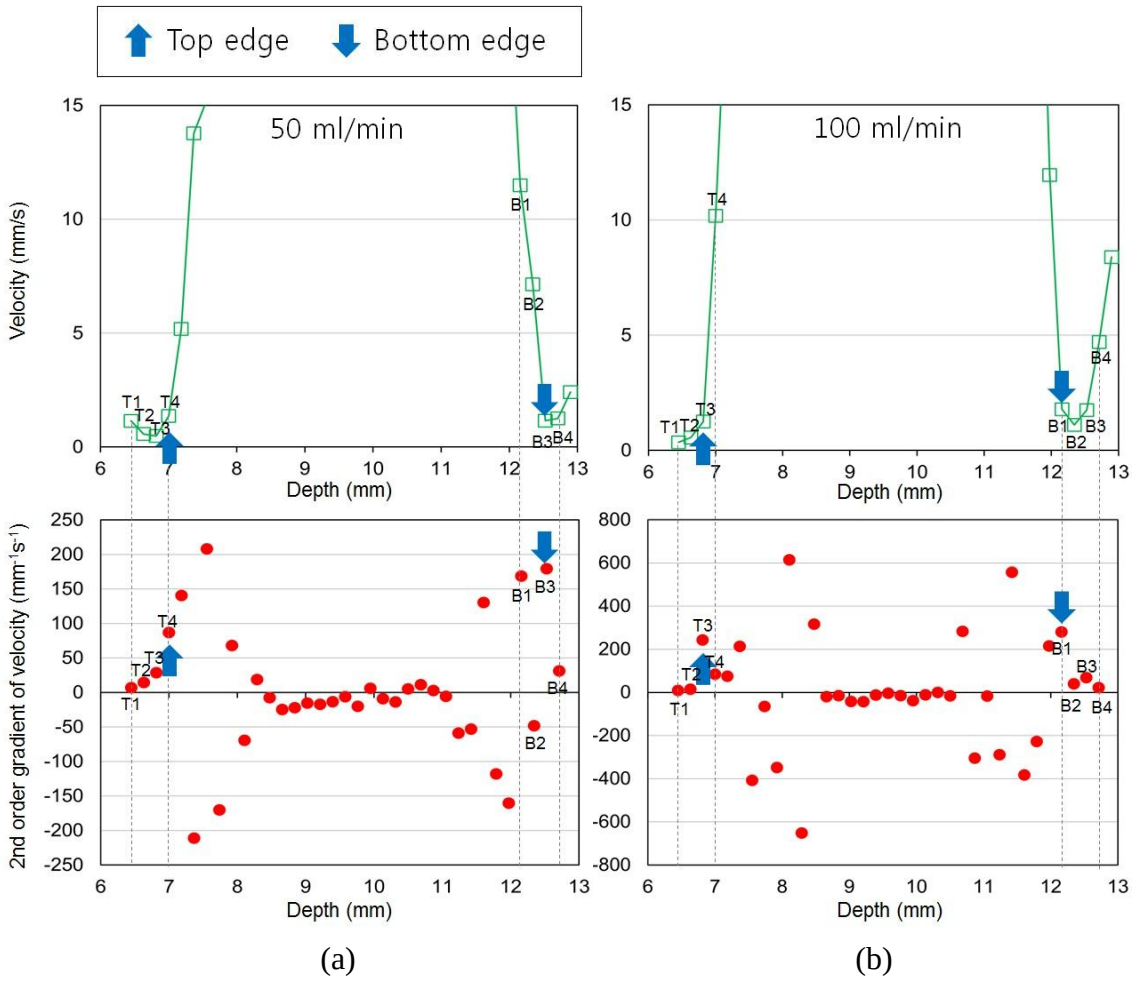


Figure 3-12. Flow velocity profiles and the 2nd order gradient of the flow velocity profile across the a-a line at (a) 50, (b) 100, (c) 150 and (d) 200 ml/min volume flow rate.

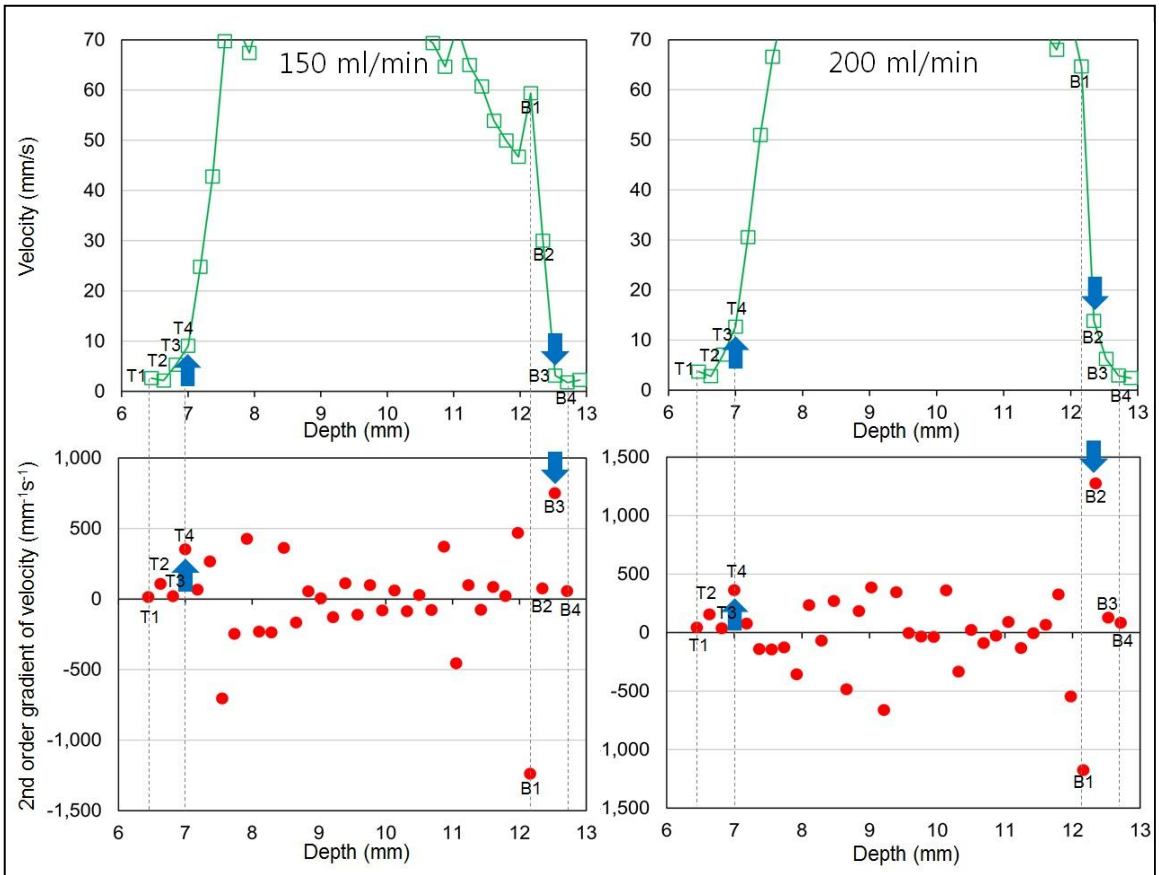


Figure 3-12 (cont.). Flow velocity profiles and the 2nd order gradient of the flow velocity profile across the a-a line at (a) 50, (b) 100, (c) 150 and (d) 200 ml/min volume flow rate.

Similarly, four pixels, denoted as B1, B2, B3 and B4 in Figure 3-11(b), were selected near the bottom edge in depth from 12.16 to 12.71 mm. The 2$^{nd}$ order gradient at B1, B2, B3 and B4 and adjacent pixels along the a-a line was determined and shown in Figure 12(b) for 100 ml/min volume flow rate. The pixel B1 had the highest 2$^{nd}$ order gradient (280 $mm^{-1}s^{-1}$) among four pixels and was determined as the bottom edge. This edge detection method was repeated for 50, 150 and 200 ml/min volume flow rate to obtain the top and bottom wall edges. As shown in Figure 3-12(a) and (c), 50 and 150 ml/min volume flow rate, the top and bottom edges were determined at pixels T4 and B3, respectively. For the 200 ml/min, the top and bottom edges were T4 and B2, respectively, as shown in Figure 3-12(d).

### 3.3.2 *Lateral speckle tracking flow velocity profile measurement and edge detection*

The flow velocity profile was also measured using the correlation based lateral speckle tracking of the flow phantom with fluid mixture flowing at mean volume flow rate of 50, 100, 150 and 200 ml/min in the second experimental setup (Figure 3-4). Figure 3-13(a) shows the B-mode image of the longitudinal view of the hole with 150 ml/min volume flow rate in the flow phantom. A total of 917 consecutive B-mode frames (in 2.15 s) were acquired. The 2D speckle tracking was performed by correlating adjacent frames (one lag) to generate 916 lateral velocity maps. In each pixel, the value of lateral velocity in these 916 lateral velocity maps was averaged to obtain the averaged lateral velocity map, as shown in Figure 3-13(b) for 150 ml/min flow rate.

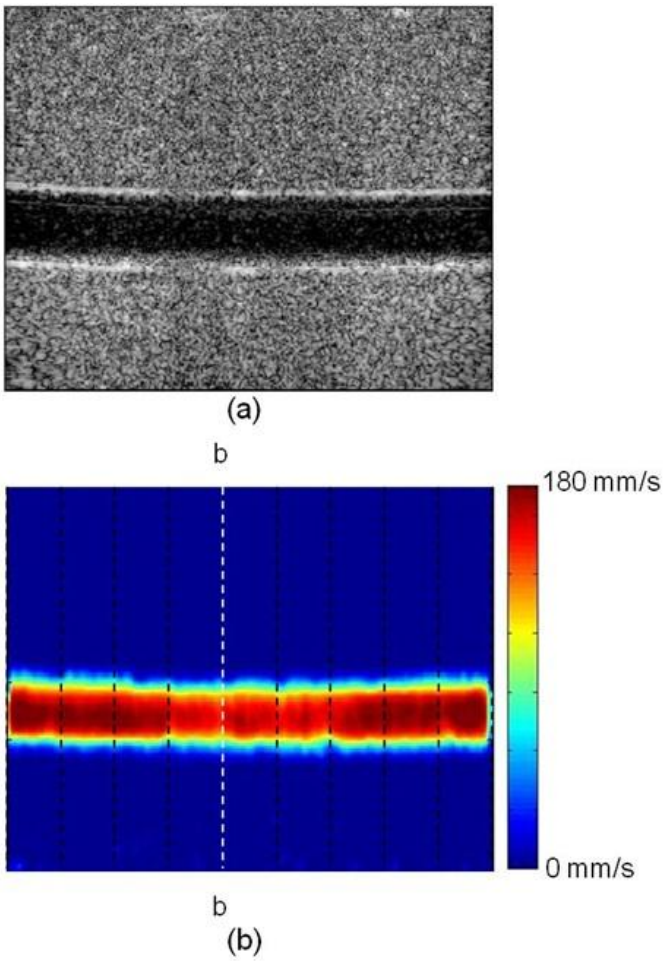


Figure 3-13. (a) B-mode image and (b) lateral velocity map of the longitudinal view of the hole with the fluid mixture flowing at mean volume flow rate of 150 ml/min in flow phantom.

Due to the pulsatile flow from the peristaltic pump (Figure 3-4), the flow velocity was not consistent along the hole, as observed in Figure 3-13(b). Ten lines with interval of 30 pixels, as shown in Figure 3-13(b), were selected across the hole. The total flow rate of the flow velocity profile measured using lateral speckle tracking in each line was calculated. The line with the flow rate closest to 150 ml/min, denoted as b-b in Figure 3-13(b), was selected to represent the flow velocity profile at 150 ml/min volume flow rate. This procedure was repeated for 50, 100 and 200 ml/min flow rate to find the cross-sectional line which had the integrated flow rate best matched to the target flow rate.

The flow velocity profiles estimated using the lateral speckle tracking flow velocity measurement method at 50, 100, 150 and 200 ml/min mean volume flow rate are shown using open circle symbol in Figure 3-10. The lateral speckle tracking flow velocity measurement method spread beyond both edges due to the correlation window with 0.54 mm size. This was caused by the spatial smoothing effect of the flow velocity profile at the edge (45).

The top and bottom wall edges were also determined using the edge detection method based on the $2^{nd}$ order gradient of the velocity profile. Figure 3-14(a) shows the B-mode image of the longitudinal view of the hole with the fluid mixture flowing at 150 ml/min volume flow rate. For the lateral speckle tracking (longitudinal view), the depth of the hole in the flow phantom was 6.9 mm deeper than that in the decorrelation based flow velocity measurement (transverse view). The depth for lateral speckle tracking was offset by this value for mutual comparison of the measurement results using these two setups. The b-b line with the integrated flow rate closest to 150 ml/min is marked. Closed-up views of pixels in the b-b line near the hole are shown in Figure 3-14(b). Four pixels near the top edge, denoted as T1, T2, T3 and T4, were identified in depths of 6.45, 6.63, 6.82 and 7.00 mm, respectively. The $2^{nd}$ order gradient at T1, T2, T3 and T4 and adjacent pixels along the b-b line was determined and shown in Figure 3-15(c) for 150 ml/min volume flow rate. The pixel T4 had the highest $2^{nd}$ order gradient (219 $mm^{-1}s^{-1}$) among three pixels and was determined as the top edge.

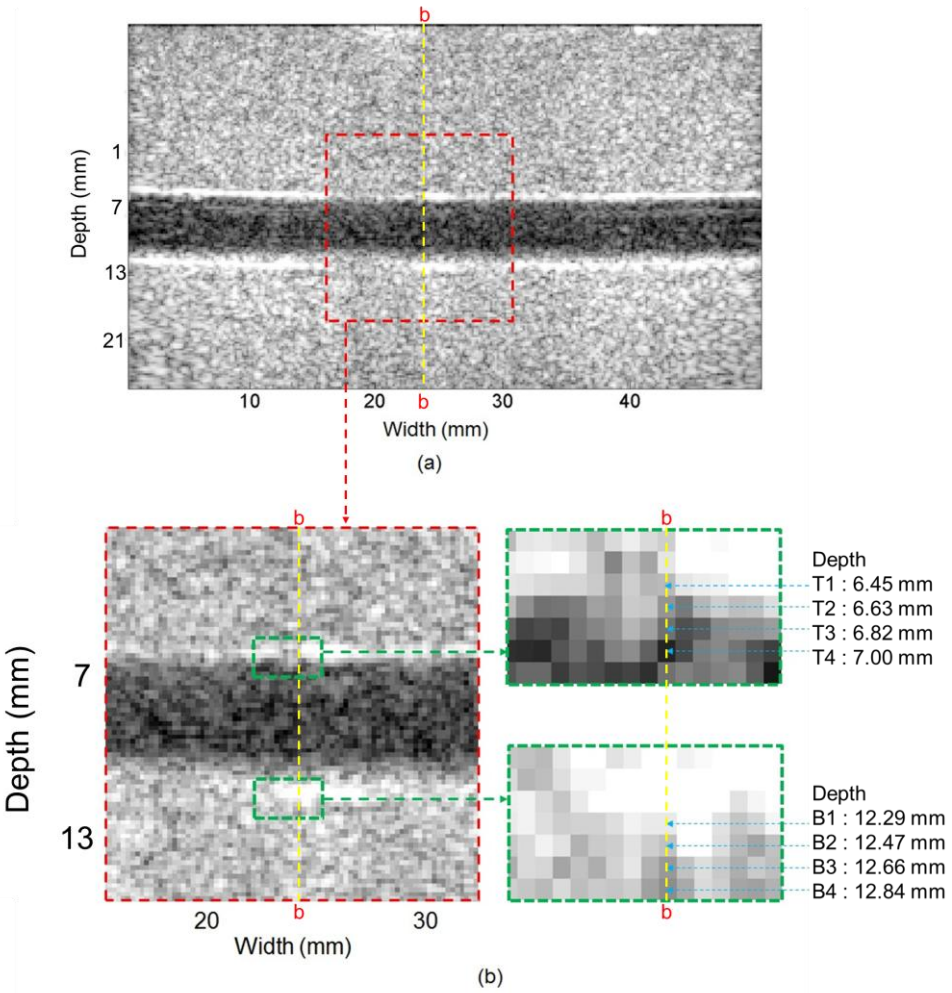


Figure 3-14. (a) B-mode image of the longitudinal view of the hole with the fluid mixture flowing at 150 ml/min volume flow rate and (b) closed-up views of pixels in the hole and near the top and bottom edges as well as the b-b line.

Similarly, four pixels, denoted as B1, B2, B3 and B4 in Figure 3-14 (b), were selected near the bottom edge with depth at 12.29, 12.47, 12.66 and 12.84 mm. The 2$^{nd}$ order gradient at B1, B2, B3 and B4 and adjacent pixels along the b-b line was determined and shown in Figure 3-15(c) for 150 ml/min volume flow rate. The pixel B2 had the highest 2$^{nd}$ order gradient (109 mm$^{-1}$s$^{-1}$) among four pixels and was determined as the bottom edge. This edge detection method was repeated for 50, 100 and 200 ml/min volume flow rate to obtain the top and bottom wall edges. For 50 and 100 ml/min volume flow rate, the top and bottom edges were determined at pixels T3 and B1, as shown in Figure

3-15(a) and (b), respectively. For the 200 ml/min (Figure 3-15(d)), the top and bottom edges were T2 and B2, respectively.

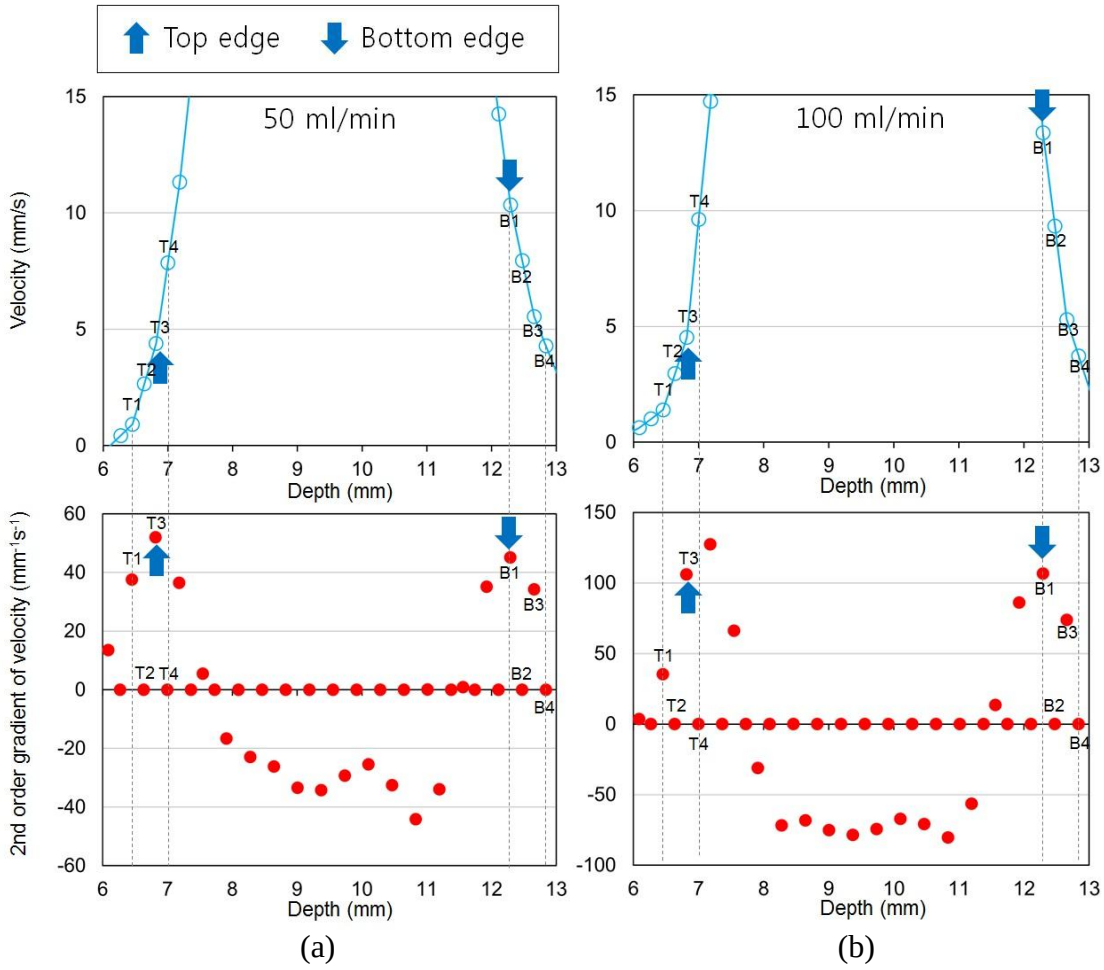


Figure 3-15. Flow velocity profiles and the 2nd order gradient of the flow velocity profile across the b-b line at (a) 50, (b) 100, (c) 150 and (d) 200 ml/min volume flow rate.

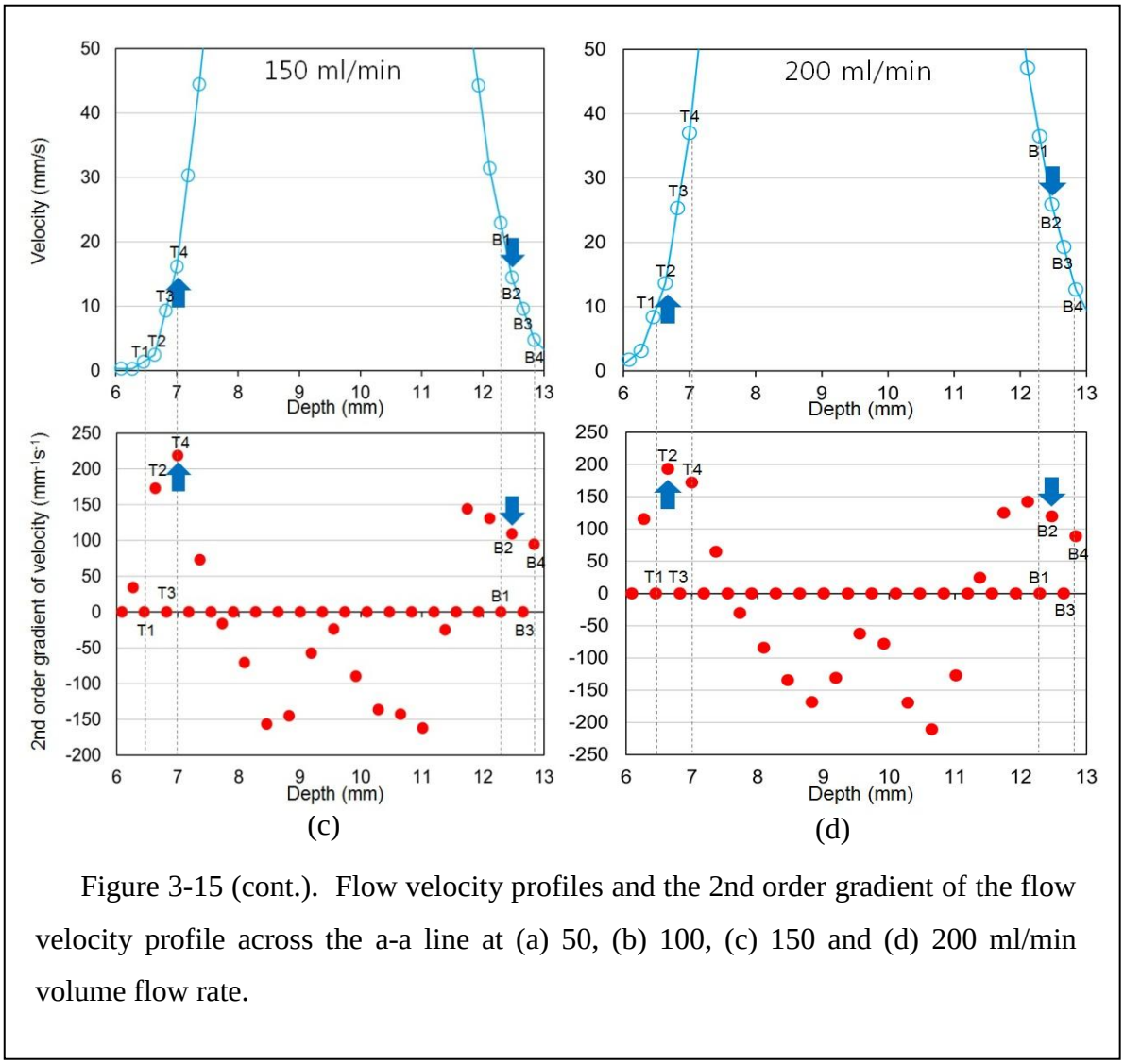


Figure 3-15 (cont.). Flow velocity profiles and the 2nd order gradient of the flow velocity profile across the a-a line at (a) 50, (b) 100, (c) 150 and (d) 200 ml/min volume flow rate.

### 3.3.3 *Velocity gradient estimation*

The velocity gradient at the wall edge was estimated using the linear regression of the flow velocity at pixels adjacent to the wall edge. Figure 3-16 shows results of velocity gradient with 3, 4 and 5 pixels adjacent to the wall edge (denoted as the 3-, 4- and 5-pixel, respectively, to include the pixel representing the wall edge) at volume flow rate of 50, 100, 150 and 200 ml/min. The velocity gradient of theoretical parabolic velocity profile at the wall edge was also listed in Table 3-1. The velocity gradient rose from 32.7 to 131 $s^{-1}$ with an increase of volume flow rate from 50 to 200 ml/min. The percentage error relative to the theoretical value was calculated.

The decorrelation based flow velocity measurement had good estimation of the velocity gradient using 3 pixels. The error was 3%, 14%, 7% and 21% for 50, 100, 150 and 200 ml/min flow rate, respectively. The lateral speckle tracking required more pixels for more accurate estimation of velocity gradient. The 5-pixel had the best estimation with 32%, 38%, 14% and 39% error for 50, 100, 150 and 200 ml/min flow rate, respectively. This level of error was higher than that in the decorrelation based flow velocity measurement.

Table 3-1. Flow velocity gradient at the wall edge at mean volume flow rate of 50, 100, 150 and 200 ml/min.

| | | Velocity gradient ($s^{-1}$) (% Error) | | | |
|---|---|---|---|---|---|
| Mean volume flow rate (ml/min) | | 50 | 100 | 150 | 200 |
| Theoretical (parabolic) velocity profile | | 32.7 | 65.3 | 98.0 | 131 |
| Decorrelation based velocity profile | 3-pixel | **33.7 (3%)** | **56.2 (14%)** | **91.4 (7%)** | **104 (21%)** |
| | 4-pixel | 27.2 (17%) | 63.4 (3%) | 108 (10%) | 98.9 (25%) |
| | 5-pixel | 29.7 (9%) | 75.6 (16%) | 93.5 (4.6%) | 89.7 (32%) |
| Lateral speckle tracking velocity profile | 3-pixel | 19.0 (42%) | 30.9 (53%) | 77.5 (21%) | 64.0 (51%) |
| | 4-pixel | 21.0 (36%) | 36.8 (44%) | 81.4 (17%) | 73.4 (44%) |
| | 5-pixel | **22.3 (32%)** | **40.7 (38%)** | **84.1 (14%)** | **79.7 (39%)** |

The trend of high error in velocity gradient estimation at high volume flow rate was the same as in the decorrelation based flow velocity measurement. This can be observed in Figure 3-16. At 200 ml/min, both decorrelation based and lateral spectral tracking flow velocity measurement methods cannot predict the rapid rise of flow velocity at the wall edge.

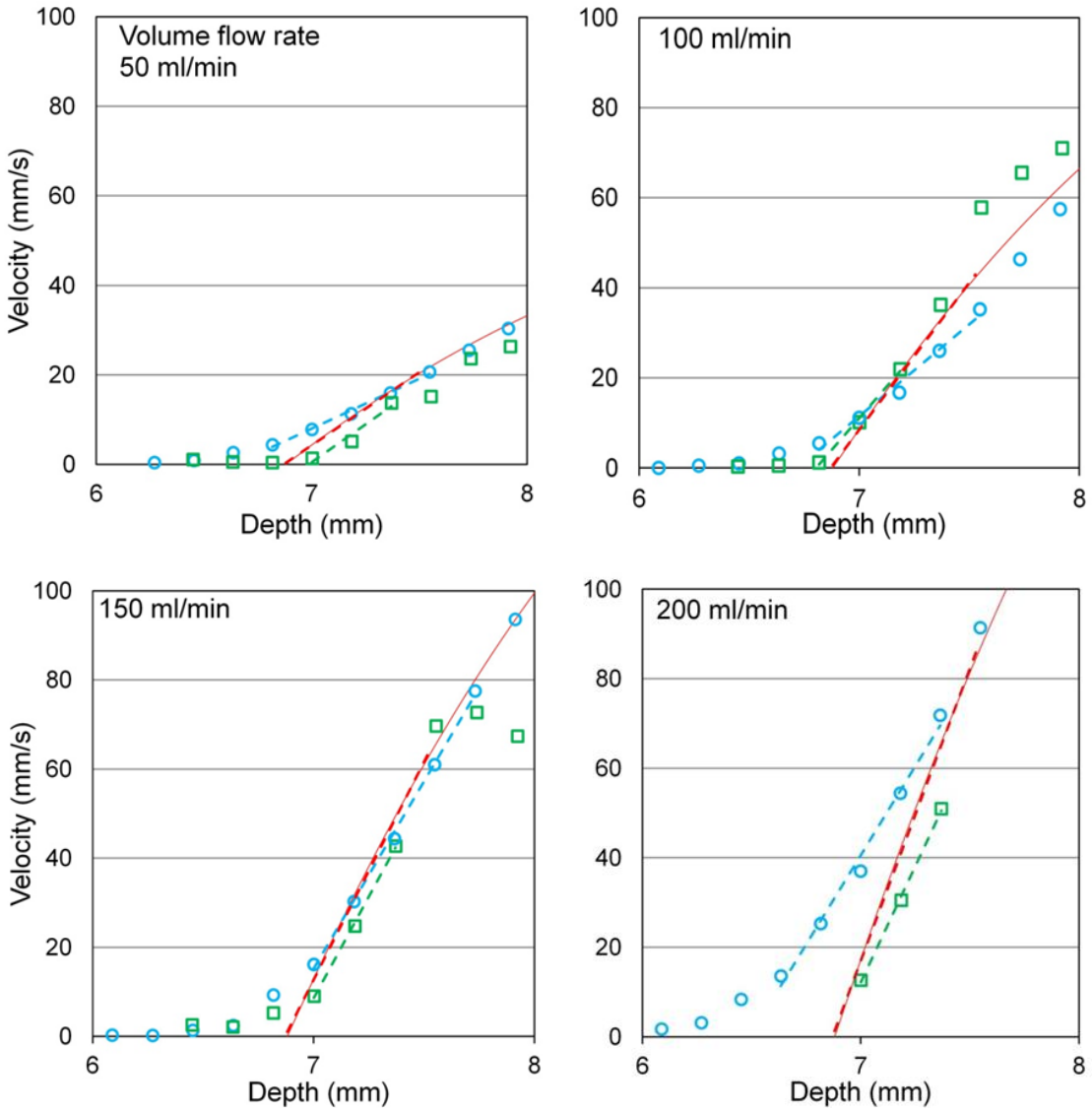


Figure 3-16. Flow velocity gradients at the wall edge at mean volume flow rate of 50, 100, 150 and 200 ml/min.

## 3.4 Discussion

The decorrelation flow velocity measurement method demonstrated to be more accurate than the lateral speckle tracking method for the prediction of the velocity gradient at the wall edge. Although the decorrelation based method has a limitation on measuring high flow velocity, as evident in Figure 3-10, it is more suitable to predict the wall edge velocity gradient. The maximum velocity gradient error was 21% at 200 ml/min volume flow rate as shown in Figure 3-16. Figure 3-17 shows the theoretical velocity versus decorrelation based flow velocity. The underestimation of flow velocity increased at high volume flow rate. In this study, the limit for accurate decorrelation measurement of flow velocity was about 80 mm/s, which was determined by the beam correlation width (about 0.3 mm) and the acoustic frame rate (348 Hz).

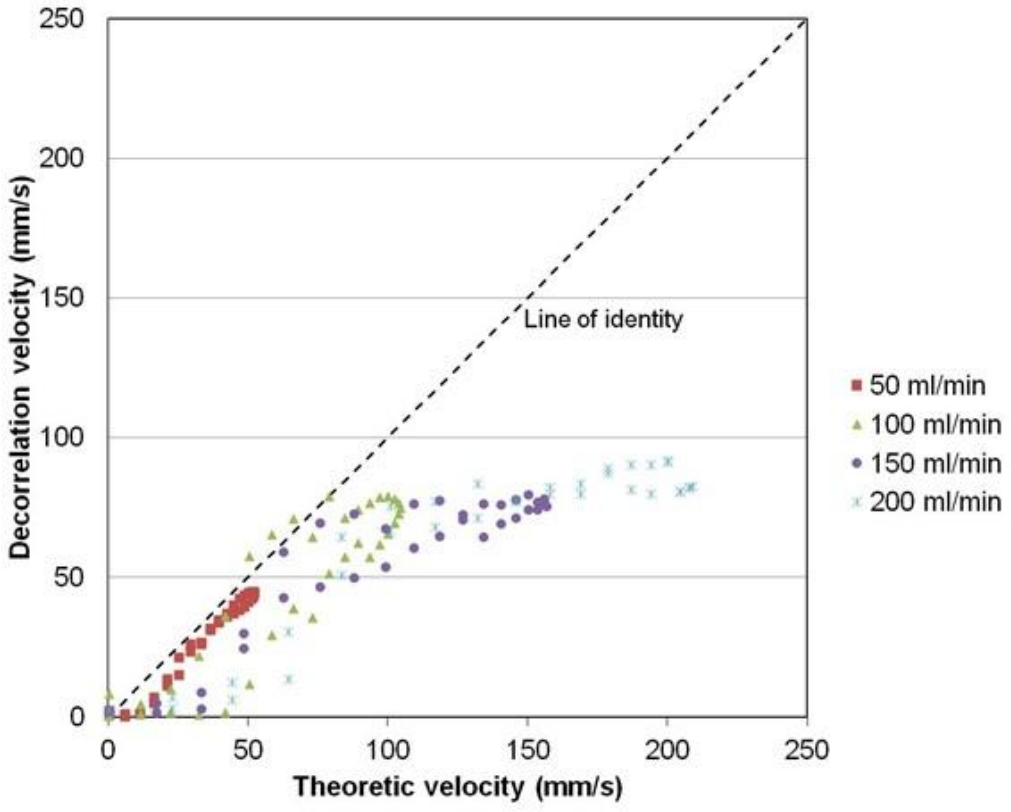


Figure 3-17. Theoretical velocity versus decorrelation based flow velocity.

The lateral speckle tracking flow velocity measurement method could measure the whole velocity profile (Figure 3-10). This is shown in Figure 3-18 on the theoretical velocity versus lateral speckle tracking flow velocity. Due to the correlation window spatial smoothing, the accuracy for predicting the edge velocity gradient was limited. The most accurate prediction of velocity gradient was only 14% at 150 ml/min volume flow rate as shown in Figure 3-16.

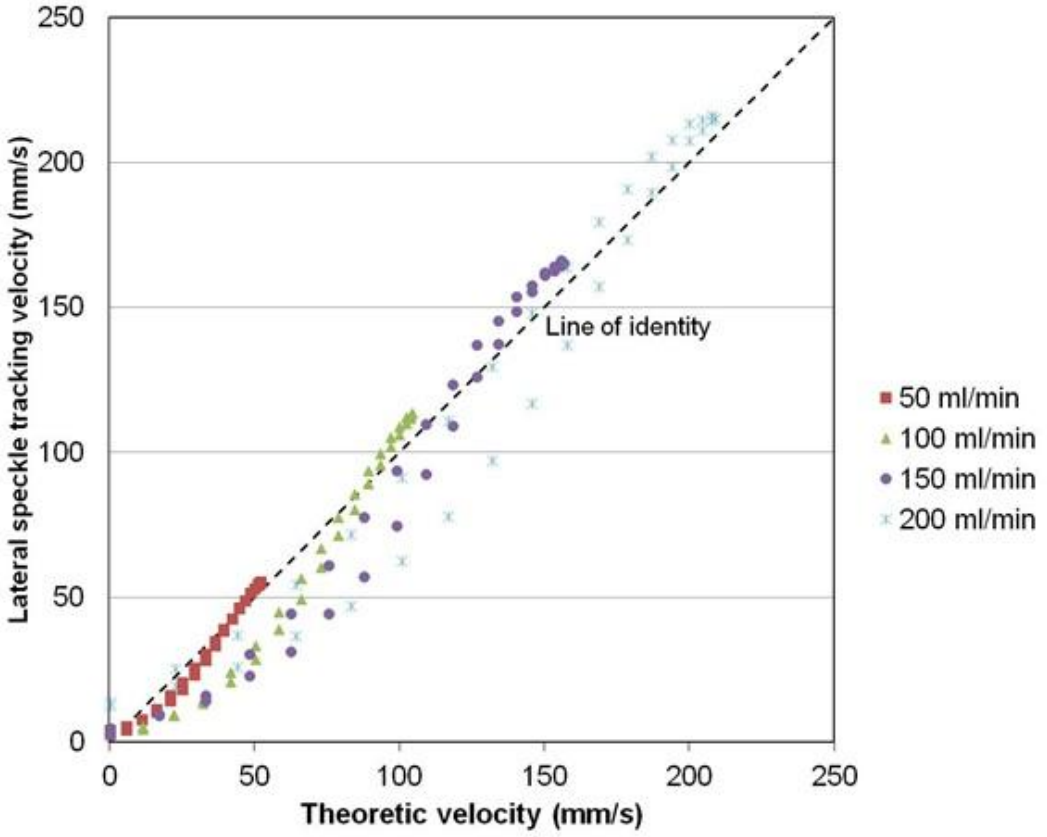


Figure 3-18. Theoretical velocity versus correlation based lateral speckle tracking velocity.

## 3.5 Conclusion

The decorrelation flow velocity measurement method not only can predict the edge velocity gradient more accurately than the lateral speckle tracking flow velocity measurement method but also has the advantage of the transverse view of the vessel for *in-vivo* patient study. A long section of vessel with uniform size is difficult to identify in the patient due to the tortuosity and branch of vessels. The transverse view of the vessel is more suitable for ultrasound transducer setup.

An application and future study of the decorrelation flow velocity measurement method is the vascular wall shear stress measurement to identify the potential for heart disease. The decorrelation based velocity measurement method is ideal to predict the flow velocity gradient and the vascular wall shear stress on healthy and high-risk patient populations to study a non-invasive way for diagnosis of heart disease.

# Chapter 4 *In-vivo* Vascular Wall Shear Rate of Renal Disease Patients

## 4.1 Introduction

Patients with chronic kidney disease (CKD) and end-stage renal disease (ESRD) have high risk of cardiovascular disease due to vascular calcification (1) and accelerated atherosclerosis, caused at least in part by abnormal endothelial function (1-3). The WSR is associated with the impairment of endothelial function and evidence is mounting it is an important indicator of future cardiovascular disease (61-66). The WSR may also be helpful in diagnose of the atherosclerosis, which has been associated with low mean WSR (67, 68).

Currently, WSR estimation is usually based on the measurement of peak blood velocity in the vessel center and the assumption that the blood velocity profile is parabolic in vessels (69-72). However, in areas of vascular tortuosity, branching and the presence of vascular plaque, the blood velocity profile is non-parabolic (28). Therefore, the direct measurement of blood velocity near the vascular wall edge may provide a significant aid for determining the WSR and reducing measurement dependence on modeling assumptions that may not be universally applicable. Ultrasound techniques have been utilized for these direct noninvasive measurements of the WSR.

Multi-gate ultrasound Doppler measurement has the advanced spatial resolution for determining the flow velocity profile at vessel wall edges (16) and has been applied to measure the WSR from longitudinal views of blood vessels based on 1D velocity measurement (17-22). The use of Doppler requires the ultrasound beam to intersect the blood flow at a non-perpendicular angle. Therefore, multi-gate ultrasound Doppler requires the assumptions that the lumen is circular and flow is symmetrical in the out-of-plane directions in order to correct for the distortion introduced due to the isonification angle. However, both assumptions are violated in the presence of vascular tortuosity and branching (16).

Decorrelation flow velocity measurement provides a possible method to overcome some of the assumptions associated with WSR measurement and has been applied to measure the flow velocity in the transverse view of the vessel (31, 36, 37). This method has been expanded to identify vascular wall edges, measure WSR directly at the vessel-blood interface and has shown potential advantages for *in-vivo* patient study.

The research presented in this manuscript involves utilizing ultrasound RF signals acquired from the brachial artery in upper arm for nine healthy, six CKD and two ESRD subjects. The blood velocity profile is measured from the transverse and longitudinal views, perpendicular to or along the blood flow direction in the brachial artery. The performance of decorrelation imaging and correlation based lateral speckle tracking flow velocity measurement methods are compared between the various patient states. The WSR is measured during the acquisition time interval using three pixels from the vascular wall edge to lumen interior using the blood velocity profile. The mean and maximum WSR are determined during sequential cardiac cycles and compared between healthy and renal disease (CKD and ESRD) subjects. The WSR and vascular diameter are determined for pre-, during- and post-vascular occlusion and compared between the healthy and the renal disease (CKD and ESRD) subjects.

## 4.2 Materials and Methods

### 4.2.1 *Subjects*

A total of nine healthy, six CKD and two ESRD subjects were enrolled for our study after providing informed consent, under a study protocol approved by our Investigational Review Board. The clinical information for the CKD patients, denoted as SB10 to SB15, and ESRD patients, denoted as SB16 and SB17, are summarized in Table 4-1. The age of the CKD subjects ranged between 42 and 73. The estimated glomerular filtration rate (eGFR) was between 4 and 39 ml/min. The systolic blood pressure ranged from 132 to 180 mmHg and the diastole blood pressure ranged from 60 to 84 mmHg. The CKD subjects had documented history of coronary artery disease (SB11, SB12 and SB14), diabetes (SB10, SB11, SB12, SB14 and SB15), hyperlipidemia (SB10, SB11 and SB12), arthritis (SB10), hypertension (SB12, SB14 and SB15), myeloma (SB13) and thrombocytopenia (SB13). The two ESRD subjects (SB16 and SB17) were aged 49 and

30, respectively. Their systolic and diastolic blood pressures were 118 and 180 mmHg, and 80 and 76 mmHg, respectively. The ESRD subject (SB16) has diabetes and was on hemodialysis. The ESRD subject (SB17) had a transplant kidney, congenital renal disease and a long history of hemodialysis.

Table 4-1. The chronic kidney disease (CKD) and end-stage renal disease (ESRD) subjects' clinical information. (SB: subject, M: male, F: female, SBP: systole blood pressure, DBP: diastole blood pressure, eGFR: estimated glomerular filtration rate)

| | | CKD | | | | | | ESRD | |
|---|---|---|---|---|---|---|---|---|---|
| | | SB10 | SB11 | SB12 | SB13 | SB14 | SB15 | SB16 | SB17 |
| Age | | 73 | 62 | 62 | 48 | 42 | 66 | 49 | 30 |
| Gender | | F | F | M | F | F | M | M | M |
| SBP | | 142 | 158 | 130 | 132 | 160 | 150 | 118 | 180 |
| DBP | | 84 | 60 | 60 | 80 | 84 | 74 | 80 | 76 |
| eGFR (ml/min) | | 21 | 16 | 39 | 6 | 10 | 4 | 5 | * |
| **Disease** | Coronary artery disease | | ■ | ■ | | ■ | | | |
| | Diabetes | ■ | ■ | ■ | | ■ | ■ | ■ | |
| | Hyperlipidemia | ■ | ■ | ■ | | | | | |
| | Arthritis | ■ | | | | | | | |
| | Congenital renal disease | | | | | | | | ■ |
| | Hypertension | | | ■ | | ■ | ■ | | |
| | Myeloma | | | | ■ | | | | |
| | Thrombocytopenia | | | | ■ | | | | |

■: Denote the subject has the disease

*: No value due to transplant kideny

### 4.2.2 *Measurement Instrumentation*

The ultrasound transducer (Model L12-5 scanner, Epsilon Imaging, Ann Arbor, Michigan, USA) with a 9-MHz linear array acquires the 19.5 mm × 24.9 mm and 28.5 mm × 49.8 mm B-mode images from the transverse and longitudinal view of the brachial artery, respectively. The software EchoInsight$^{TM}$ (Epsilon Imaging, Ann Arbor, Michigan, USA) performs the finite impulse response (FIR) high pass filtering of the RF data and applies a 2D speckle tracking algorithm using a 5 by 3-pixel kernel and a 9 by 5-pixel filter. The FIR high pass filtering, which subtracts RF-signals of two intervals of consecutive frames, is applied for the B-mode RF-signals to suppress the reverberation noise and enhance the variation of RF-signals between frames and the accuracy of wall edge detection.

### 4.2.3 *Measurement Procedure*

The WSR was measured from the transverse view of the brachial artery pre-, during- and post-arterial occlusion by inflating a pressure cuff placed around the upper arm to a suprasystolic pressure for about one minute. Figure 4-1(a) shows the pre- and post-arterial occlusion and Figure 4-1(b) shows the during-arterial occlusion measurement. Figure 4-1(c) shows the blood velocity measurement from longitudinal view of the artery. The subjects were examined in sitting position and their arm was located at heart level. The ultrasound transducer was placed on the anterior surface of the upper arm. The RF signals were acquired from the transverse and longitudinal views of the brachial artery. For the transverse and longitudinal view, the artery remained in the center of the B-mode image by applying continuous freehand positioning over the arterial region of interest.

Two measurement methods, decorrelation and correlation based lateral speckle tracking, were used to obtain the blood velocity profile from the transverse and longitudinal view, respectively. For the decorrelation flow velocity measurement method, 2D speckle motion tracking was performed over 1000 B-mode frames to obtain 999 correlation maps of the artery. An arbitrarily line was selected across the center of the vessel in these 999 correlation maps. The median temporal filtering with 20 frames was applied to correlation coefficient of the pixels along the selected line for entire 999 frames using MATLAB (version 2009a, Mathworks, Natwick, MA, USA) to reduce the

noise from tissue motion. Speckle movement due to blood flow for the transverse plane was calculated using the relationship obtained through a calibration procedure where the correlations of sequential acoustic beams were mapped versus a controlled speckle movement (Park et al. submitted). 999 blood velocity profiles were determined in 2.9 s along the selected line by multiplying the speckle movement in two consecutive frames by the acoustic frame rate.

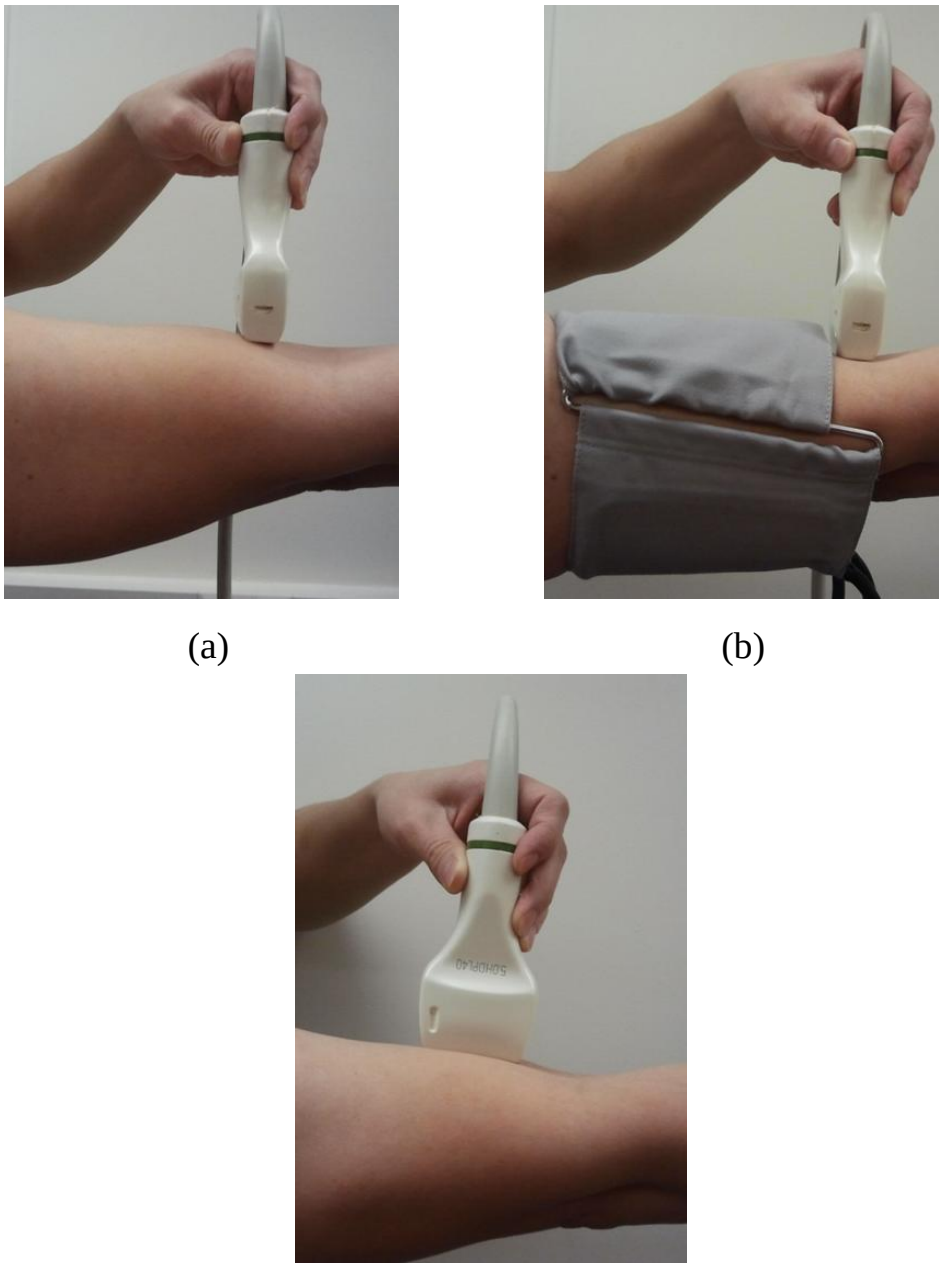

Figure 4-1. (a) Transverse blood velocity measurement in the brachial artery, (b) transverse blood velocity measurement in the brachial artery with pressure cuff and (c) longitudinal blood velocity measurement in the brachial artery.

The correlation based lateral speckle tracking flow velocity measurement method was also applied for comparison. For this method, 2D speckle tracking was performed for 917 RF frames to obtain 916 lateral velocity maps of the artery. An arbitrary line was

selected across the vessel in these 916 lateral velocity maps. The median temporal filtering with 20 frames was also applied to lateral velocity of the pixels along the selected line for entire 916 frames. 916 blood velocity profiles were determined in 2.2 s along the selected line.

The vascular wall edges were determined using the B-mode image and the 2$^{nd}$ order gradient of the blood velocity profile. Figure 4-2 shows an example of the healthy subject (SB1) B-mode image of the transverse view of the brachial artery without cuff and close-up view of pixels in the artery near the top and bottom edges as well as an arbitrarily placed vessel section line (a-a). Four pixels near the top edge, denoted as T1, T2, T3 and T4, were identified based on the transition of grey scale at depth of 5.16, 5.34, 5.53 and 5.71 mm. Similarly, four pixels, denoted as B1, B2, B3 and B4 in Figure 4-2(b), were selected near the bottom edge in depth from 9.58 to 10.1 mm. The 2$^{nd}$ order gradient of blood velocity at T1, T2, T3, T4, B1, B2, B3 and B4 and adjacent pixels along the a-a line was calculated to determine the vascular wall edges. The WSR was calculated during acquisition time interval (2.9 s) using three pixels from the wall edge to inside of the lumen in the transverse view. Figure 4-3 shows an example of the healthy subject (SB1) B-mode image of the longitudinal view of the brachial artery without cuff, and close-up views of pixels in the artery near the top and bottom edges as well as the b-b line, an arbitrary line across the vessel. The top and bottom wall edges were also determined using the edge detection method based on the 2$^{nd}$ order gradient of the blood velocity profile. The WSR was calculated during the acquisition time interval using five pixels from the wall edge to inside of the lumen for the longitudinal view.

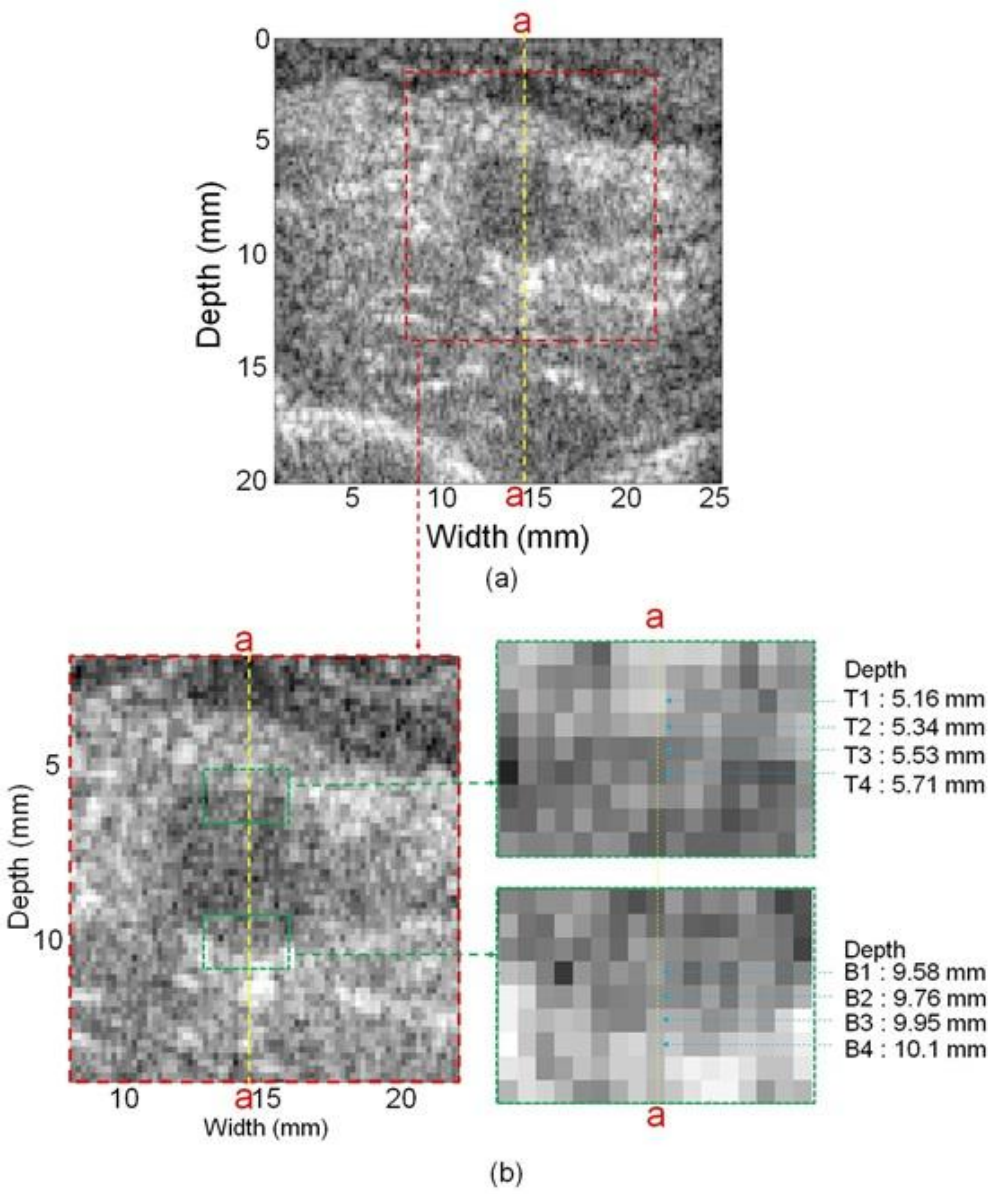


Figure 4-2. (a) B-mode image of the transverse view of the brachial artery and (b) closed-up views of pixels in the artery and near the top and bottom edges as well as the a-a line. (SB1, without cuff)

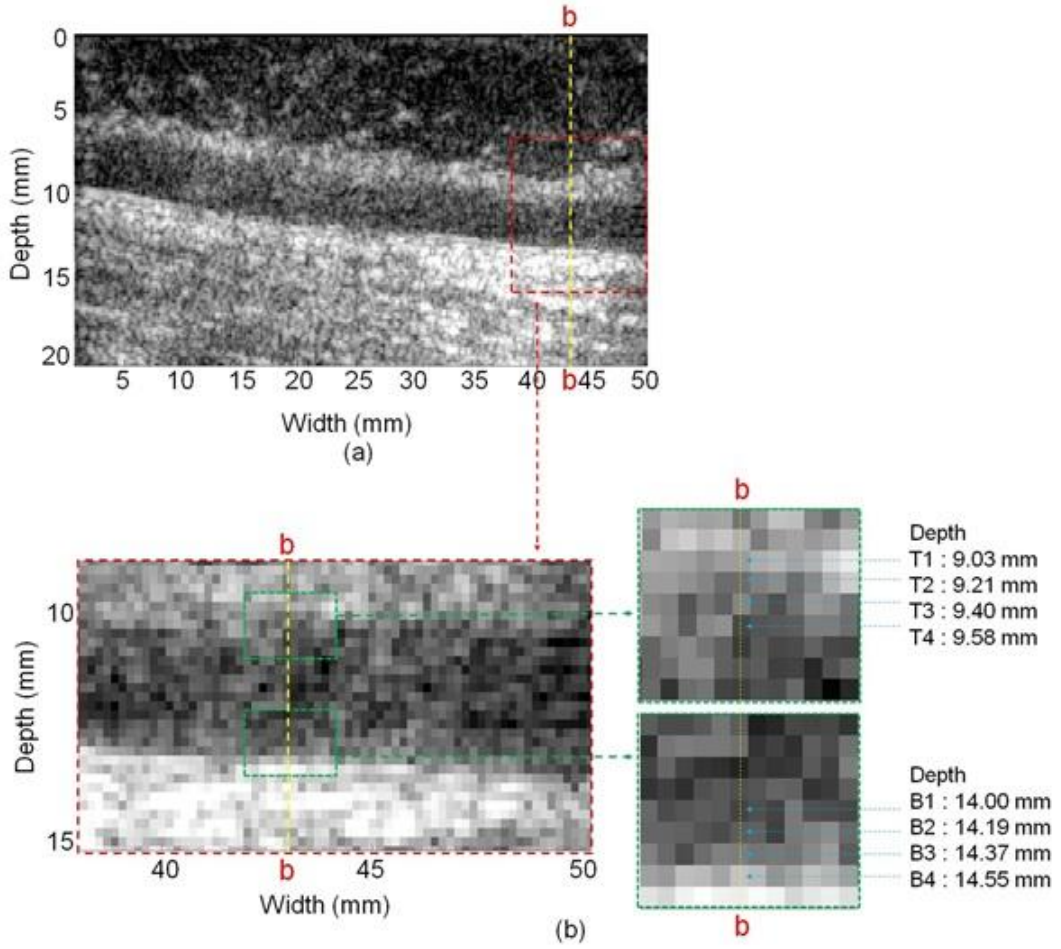


Figure 4-3. (a) B-mode image of the longitudinal view of the brachial artery and (b) closed-up views of pixels in the artery and near the top and bottom edges as well as the b-b line. (SB1, without cuff)

In each cardiac cycle, the mean WSR, denoted as $WSR_{mean}$, and the maximum WSR, denoted as $WSR_{max}$, were calculated and compared between healthy and renal disease (CKD and ESRD) subjects. The average of $WSR_{mean}$, marked as $\overline{WSR}_{mean}$, and the $WSR_{max}$, marked as $\overline{WSR}_{max}$, of the two or three cardiac cycles were determined for each subject. For the $\overline{WSR}_{mean}$ and $\overline{WSR}_{max}$, the Shapiro-Wilk normality test was performed to evaluate normal distribution of healthy and renal disease subjects. A t-test was performed for the $\overline{WSR}_{mean}$ and $\overline{WSR}_{max}$ to compare the healthy and renal disease (CKD

and ESRD) subjects. Blood flow occlusion using a pressure cuff was performed on healthy (SB1-SB9), CKD (SB10-SB15) and ESRD (SB16 and SB17) subjects. The $\overline{WSR}_{mean}$ was determined pre-, during- and post-vascular occlusion and denoted as $\overline{WSR}_{mean}^{pre}$, $\overline{WSR}_{mean}^{during}$ and $\overline{WSR}_{mean}^{post}$, respectively. The $\overline{WSR}_{max}$ was also determined pre-, during- and post-vascular occlusion and denoted as $\overline{WSR}_{max}^{pre}$, $\overline{WSR}_{max}^{during}$ and $\overline{WSR}_{max}^{post}$, respectively. These WSRs and vessel diameter are calculated and compared between the healthy and renal disease (CKD and ESRD) subjects. The t-test was performed to compare $\overline{WSR}_{mean}^{pre} - \overline{WSR}_{mean}^{during}$, $\overline{WSR}_{max}^{pre} - \overline{WSR}_{max}^{during}$, $\overline{WSR}_{mean}^{post} - \overline{WSR}_{mean}^{during}$, $\overline{WSR}_{max}^{post} - \overline{WSR}_{max}^{during}$, $\overline{WSR}_{mean}^{post} - \overline{WSR}_{mean}^{pre}$ and $\overline{WSR}_{max}^{post} - \overline{WSR}_{max}^{pre}$ and the vascular diameter for the healthy and disease subjects.

### 4.3 Results

Figure 4-4 (a) shows an example of the top and bottom vessel edge WSR versus time for a healthy subject (SB1) during the 2.9 s acquisition time interval which has three cardiac cycles using the decorrelation flow velocity measurement method. A moving average filter with 40 pixels$\times$40 frames using MATLAB (version 2009a, Mathworks, Natwick, MA, USA) was applied to remove the noise for WSR versus time. The cardiac cycle was determined from time interval between sharp gradient changes of the WSR. Figure 4-4(b) shows the depth of top and bottom wall edges versus time during the acquisition time interval. For the top and bottom wall edges, the median temporal filtering with 20 frames and moving average filter with 40 pixels$\times$40 frames were also applied to the top and bottom wall edges versus time using MATLAB (version 2009a, Mathworks, Natwick, MA, USA) for noise reduction. The arterial diameter, as shown in Figure 4-4(c), was determined by subtracting from the bottom to top wall edges. The arterial diameter changed from 3.7 to 4.4 mm during cardiac cycle.

The WSR and vascular wall edges and diameter can also be determined using the lateral speckle tracking flow velocity measurement. The $WSR_{mean}$ was similar for both the decorrelation and lateral speckle tracking flow velocity measurement, but higher variations of WSR was observed in the lateral speckle tracking flow velocity

measurement due to the correlation window spatial smoothing. The decorrelation flow velocity measurement was applied to measure the WSR in this study.

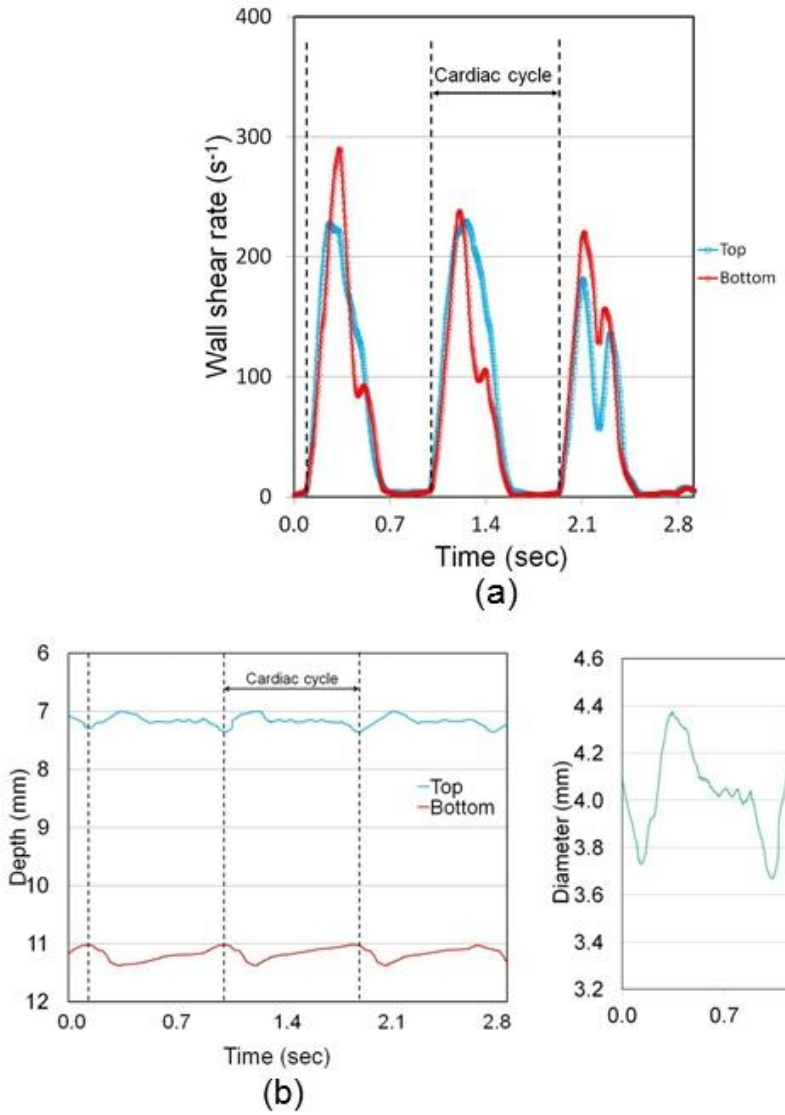


Figure 4-4. (a) Time versus vascular wall shear rate during acquisition time interval (in 2.9 s), (b) time versus top and bottom vascular wall edges during acquisition time interval (in 2.9 s) and (c) time versus arterial diameter during acquisition time interval (in 2.9 s). (SB1, without cuff)

Figure 4-5. shows the $WSR_{mean}$ and $WSR_{max}$ in each cardiac cycle for nine healthy and eight renal disease (six CKD and two ESRD) subjects at top and bottom wall edges. The $WSR_{mean}$ and $WSR_{max}$ are represented as open green diamond and blue circle symbols,

respectively. The dash line represents $\overline{WSR}_{mean}$ and $\overline{WSR}_{max}$ of the two or three cardiac cycles for each subject.

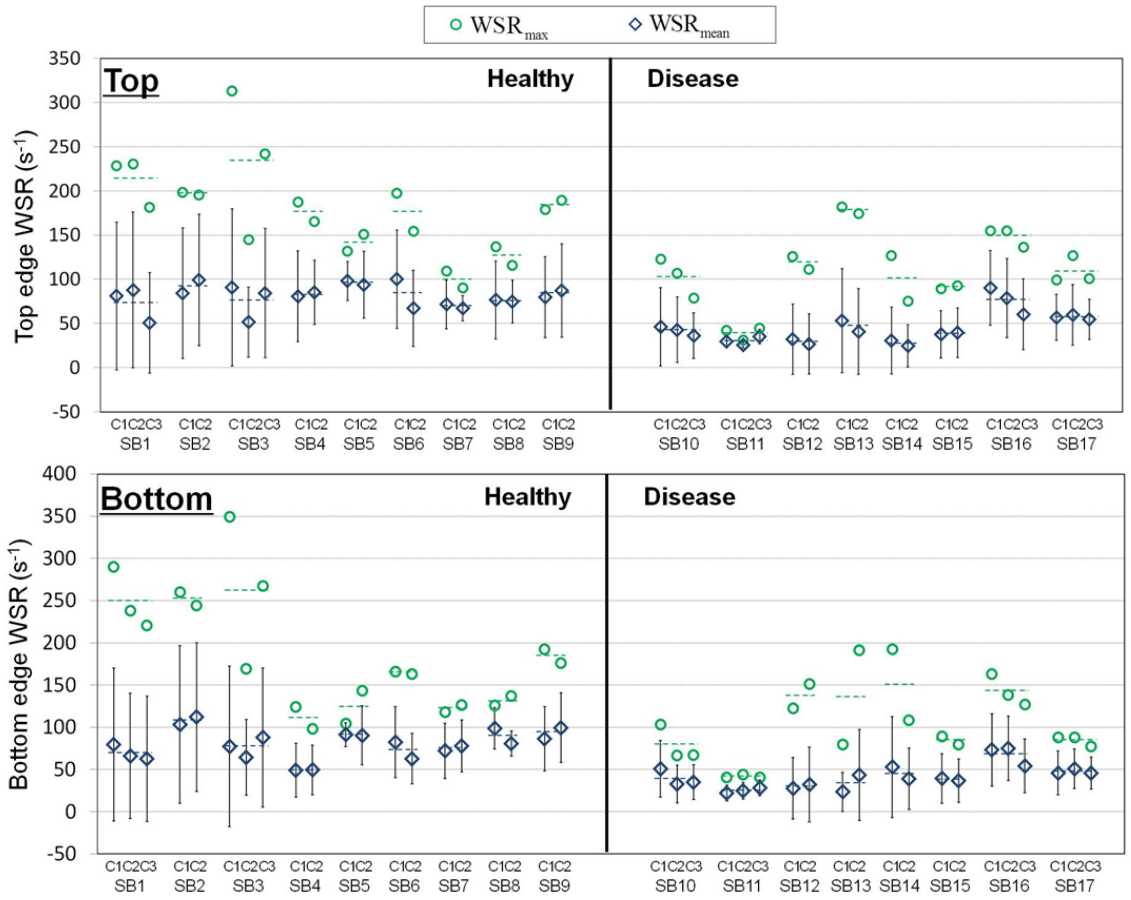


Figure 4-5. Mean vascular wall shear rate ($WSR_{mean}$) and maximum vascular wall shear rate ($WSR_{max}$) in each cardiac cycle for nine healthy and eight renal disease (six CKD and two ESRD) subjects from top and bottom vascular wall edges. (SB1 to SB9 representing healthy subjects, SB10 to SB15 representing CKD subjects and SB16 and SB17 representing ESRD subjects and C1, C2 and C3 representing cardiac cycles)

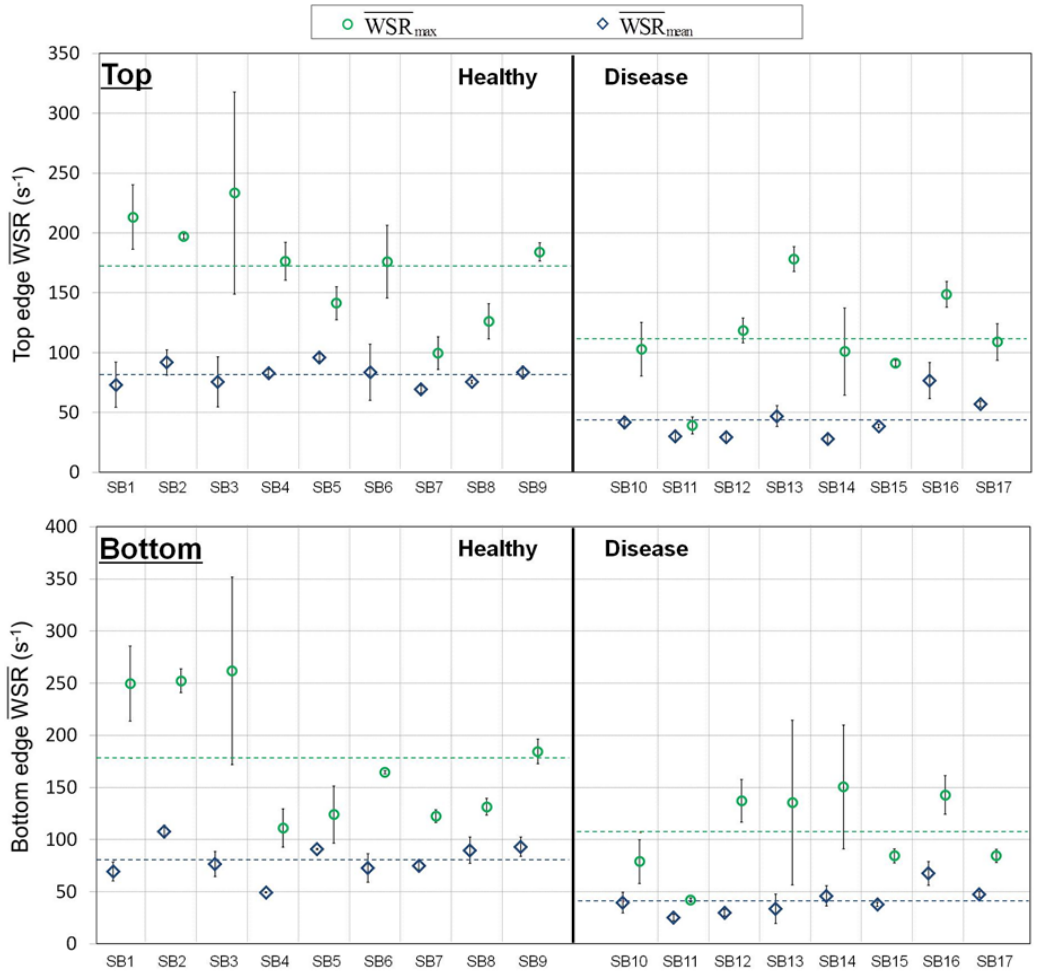


Figure 4-6. Average mean vascular wall shear rate ($\overline{WSR}_{mean}$) and maximum vascular wall shear rate ($\overline{WSR}_{max}$) for nine healthy and eight renal disease (six CKD and two ESRD) subjects from top and bottom vascular wall edges. (SB1 to SB9 representing healthy subjects, SB10 to SB15 representing CKD subjects and SB16 and SB17 representing ESRD subjects)

The $\overline{WSR}_{mean}$ and $\overline{WSR}_{max}$ for nine healthy and eight renal disease (six CKD and two ESRD) subjects are shown in Figure 4-6 at top and bottom wall edges. The dash line represents the average $\overline{WSR}_{mean}$ and $\overline{WSR}_{max}$ for the nine healthy and eight renal disease subject groups. Both $\overline{WSR}_{mean}$ and $\overline{WSR}_{max}$ had normal distribution for healthy and renal disease subjects in the Shapiro-Wilk normality test. The average $\overline{WSR}_{mean}$ and $\overline{WSR}_{max}$ were significantly different with all $p < 0.05$ at top and bottom wall edges, as summarized in Table 4-2, for the healthy versus renal disease subjects.

Table 4-2. The average and standard error of the mean (SEM) of average mean vascular wall shear rate ($\overline{WSR}_{mean}$) and average maximum vascular wall shear rate ($\overline{WSR}_{max}$) for nine healthy and eight renal disease (six CKD and two ESRD) subjects.

| | | Healthy ($s^{-1}$) | Disease ($s^{-1}$) | $p$ (two-tailed) |
|---|---|---|---|---|
| $\overline{WSR}_{mean}$ | Top | 80.96±3.03 | 43.51±5.89 | 0.00003* |
| | Bottom | 81.54±5.48 | 40.87±4.66 | 0.0001* |
| $\overline{WSR}_{max}$ | Top | 168.8±13.4 | 111.1±14.5 | 0.01* |
| | Bottom | 173.7±19.2 | 107.0±14.0 | 0.01* |

* $p < 0.05$

For five healthy and three renal disease (two CKD and one ESRD) subjects, the $\overline{WSR}_{mean}^{pre}$, $\overline{WSR}_{mean}^{during}$ and $\overline{WSR}_{mean}^{post}$ are shown in Figure 4-7 and $\overline{WSR}_{max}^{pre}$, $\overline{WSR}_{max}^{during}$ and $\overline{WSR}_{max}^{post}$ are shown in Figure 4-8 at top and bottom wall edges. Changes from average $\overline{WSR}_{mean}^{during}$ to average $\overline{WSR}_{mean}^{post}$ and from average $\overline{WSR}_{mean}^{pre}$ to average $\overline{WSR}_{mean}^{post}$ were distinctly different for the healthy and renal disease subjects as shown in Figure 4-9.

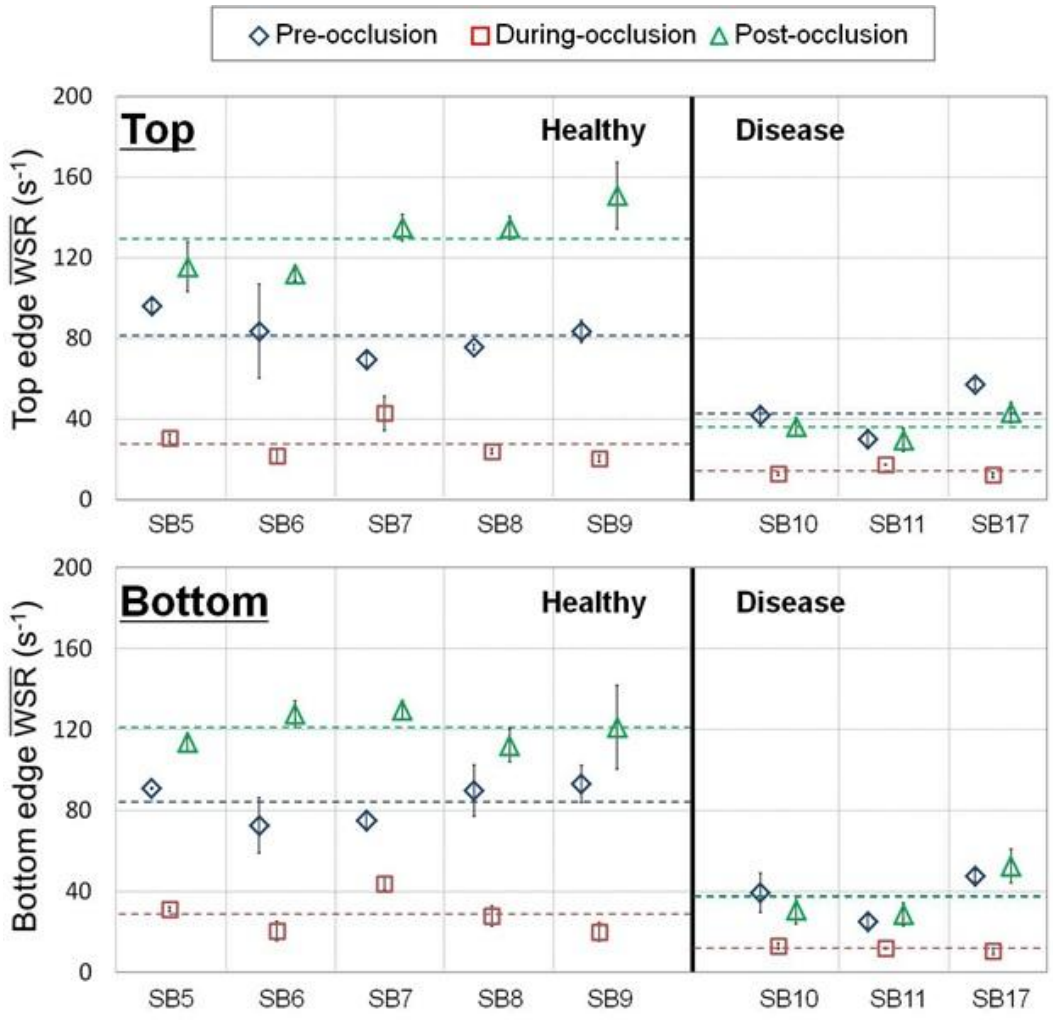


Figure 4-7. Average mean pre- ( $\overline{WSR}_{mean}^{pre}$ ), mean during- ( $\overline{WSR}_{mean}^{during}$ ) and mean post-vascular occlusion vascular wall shear rate ( $\overline{WSR}_{mean}^{post}$ ) for five healthy and three renal disease (two CKD and one ESRD) subjects from top and bottom vascular wall edges. (SB5 to SB9 representing healthy subjects, SB10 and SB11 representing CKD subjects and SB17 representing ESRD subjects)

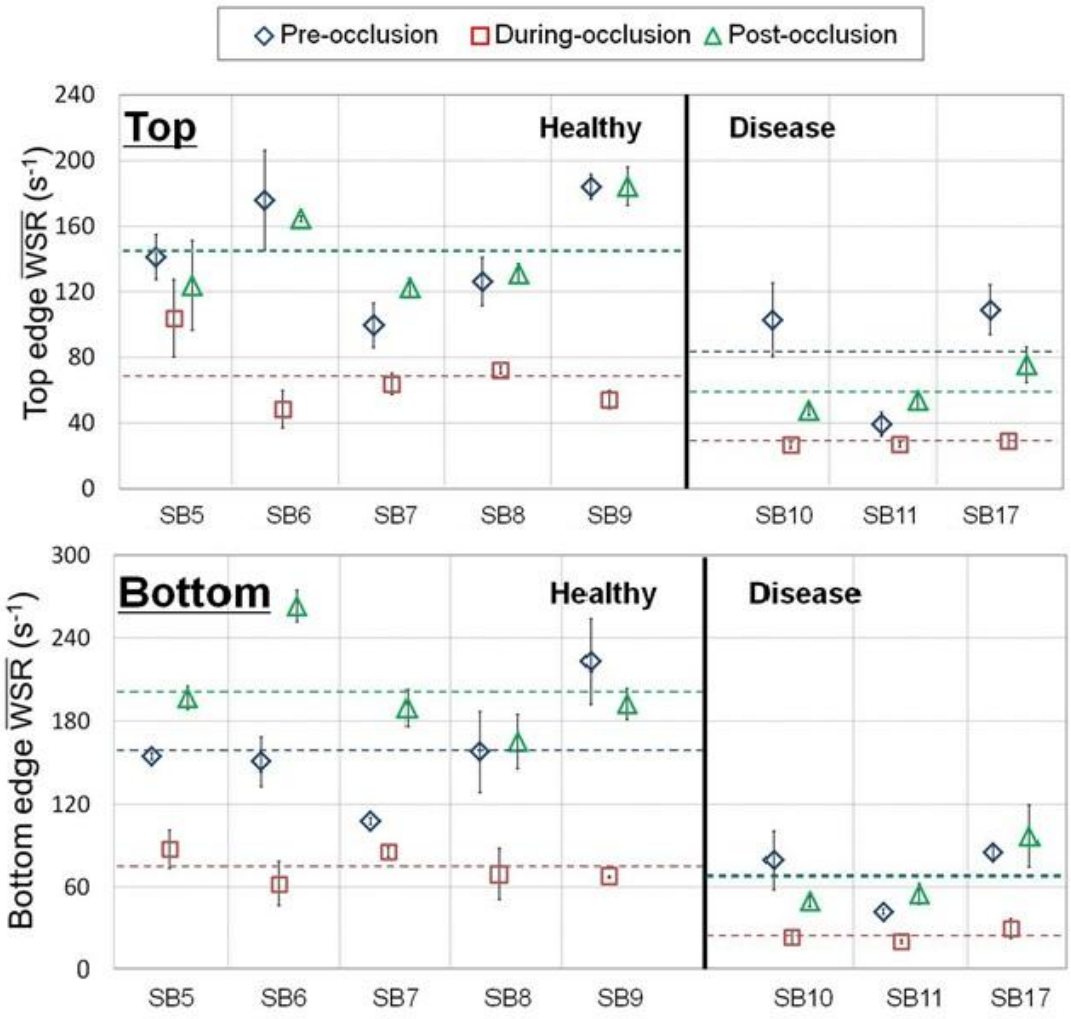


Figure 4-8. Average max pre- ($\overline{WSR}_{max}^{pre}$), max during- ($\overline{WSR}_{max}^{during}$) and max post-vascular occlusion vascular wall shear rate ($\overline{WSR}_{max}^{post}$) for five healthy and three renal disease (two CKD and one ESRD) subjects from top and bottom vascular wall edges. (SB5 to SB9 representing healthy subjects, SB10 and SB11 representing CKD subjects and SB17 representing ESRD subjects)

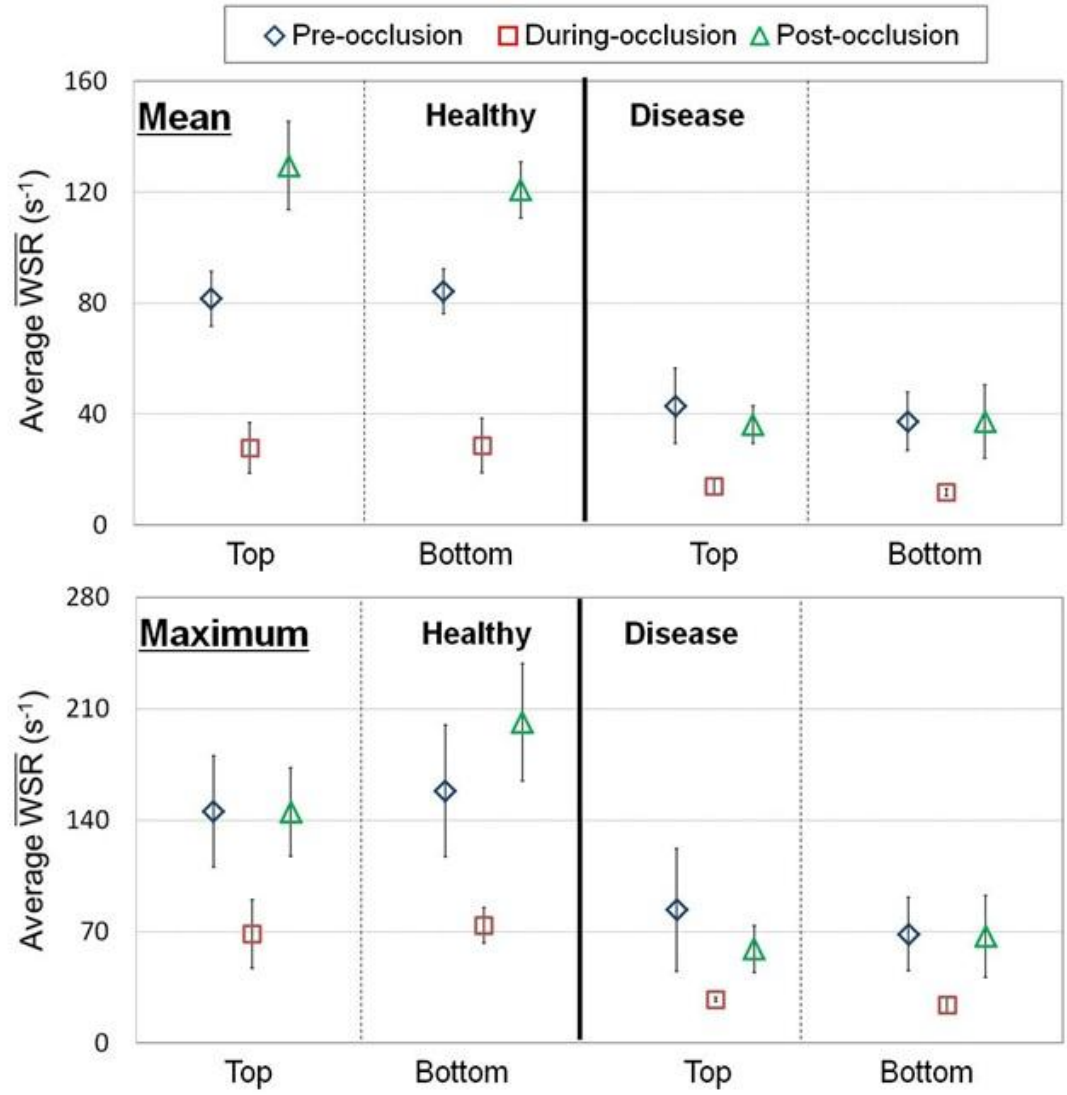


Figure 4-9. Average mean and maximum pre-, during- and post-vascular occlusion vascular wall shear rate for five healthy and three renal disease (two CKD and one ESRD) subjects from top and bottom vascular wall edges.

As summarized in the t-test results in Table 4-3, the average $\overline{\overline{WSR}}_{mean}^{post} - \overline{\overline{WSR}}_{mean}^{during}$ and average $\overline{\overline{WSR}}_{mean}^{post} - \overline{\overline{WSR}}_{mean}^{pre}$ were significant with all $p < 0.05$ at top and bottom edges for the healthy versus renal disease subjects.

Table 4-3. The average and standard error of the mean (SEM) of average mean vascular wall shear rate ($\overline{\overline{WSR}}_{mean}$) change for pre-, during- and post-blood occlusion for five healthy and three renal disease (two CKD and one ESRD) subjects.

| | | Healthy ($s^{-1}$) | Disease ($s^{-1}$) | *p* |
|---|---|---|---|---|
| $\overline{\overline{WSR}}_{mean}^{pre} - \overline{\overline{WSR}}_{mean}^{during}$ | Top | 53.80±7.19 | 28.88±9.26 | 0.08 |
| | Bottom | 55.63±6.95 | 25.58±6.88 | 0.03* |
| $\overline{\overline{WSR}}_{mean}^{post} - \overline{\overline{WSR}}_{mean}^{during}$ | Top | 101.8±8.40 | 22.20±5.44 | 0.001* |
| | Bottom | 92.15±5.00 | 25.53±8.27 | 0.0003* |
| $\overline{\overline{WSR}}_{mean}^{post} - \overline{\overline{WSR}}_{mean}^{pre}$ | Top | 48.00±10.0 | -6.68±3.90 | 0.004* |
| | Bottom | 36.52±7.50 | -0.06±4.30 | 0.006* |

* $p < 0.05$

On the contrary, the average $\overline{\overline{WSR}}_{max}^{pre} - \overline{\overline{WSR}}_{max}^{during}$ and $\overline{\overline{WSR}}_{max}^{post} - \overline{\overline{WSR}}_{max}^{pre}$ were not significantly different for the healthy and renal disease subjects at top and bottom, as summarized in Table 4-4.

Table 4-4. The average and standard error of the mean (SEM) of average maximum vascular wall shear rate ($\overline{\overline{WSR}}_{max}$) change for pre-, during- and post-blood occlusion for five healthy and three renal disease (two CKD and one ESRD) subjects.

| | | Healthy WSR ($s^{-1}$) | Disease WSR ($s^{-1}$) | *p* |
|---|---|---|---|---|
| $\overline{\overline{WSR}}_{max}^{pre} - \overline{\overline{WSR}}_{max}^{during}$ | Top | 76.88±21.4 | 56.23±22.0 | 0.551 |
| | Bottom | 84.57±21.4 | 44.49±11.1 | 0.226 |
| $\overline{\overline{WSR}}_{max}^{post} - \overline{\overline{WSR}}_{max}^{during}$ | Top | 76.74±20.3 | 31.58±7.71 | 0.154 |
| | Bottom | 127.6±19.1 | 43.02±12.3 | 0.02* |
| $\overline{\overline{WSR}}_{max}^{post} - \overline{\overline{WSR}}_{max}^{pre}$ | Top | -0.14±6.99 | -24.7±20.6 | 0.215 |
| | Bottom | 42.97±25.6 | -1.47±14.0 | 0.259 |

* $p < 0.05$

The diameter of artery pre-, during- and post-arterial occlusion was measured during the 2.9 s acquisition time interval for five healthy and three renal disease (two CKD and one ESRD) subjects. Figure 4-10 shows the average pre-, during- and post-arterial occlusion arterial diameter for five healthy and three renal disease (two CKD and one ESRD) subjects. The arterial diameter change between pre- and post-arterial occlusion was not significantly different between the healthy and renal disease subjects ($p$= 0.089).

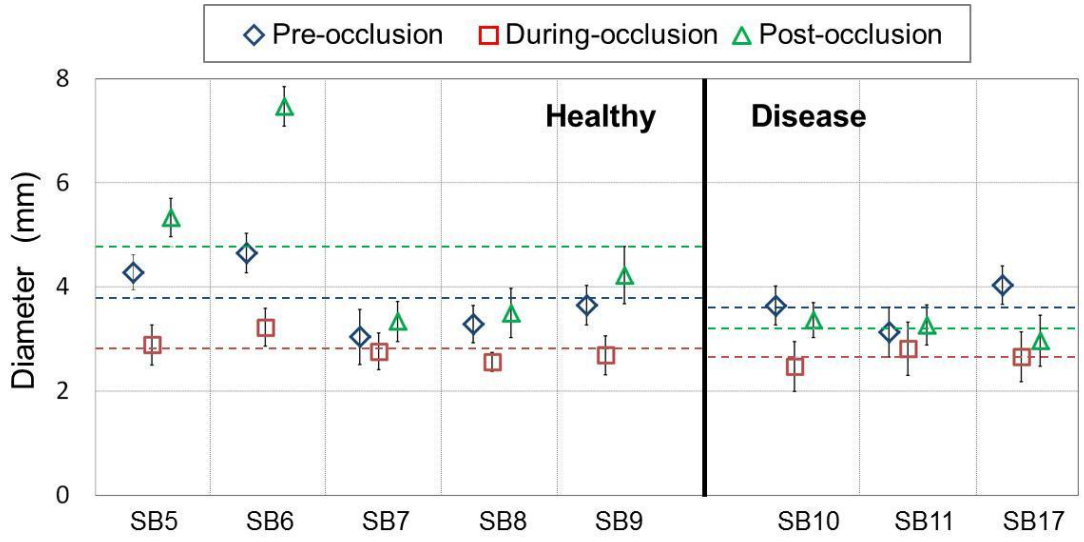


Figure 4-10. Average pre-, during- and post-vascular occlusion arterial diameter for five healthy and three renal disease (two CKD and one ESRD) subjects. (SB5 to SB9 representing healthy subjects, SB10 and SB11 representing CKD subjects and SB17 representing ESRD subjects)

## 4.4 Discussion

Although this is a small study, an interesting observation is that the WSR was found to be significantly different between groups when vessel diameter was not. Since vessel diameter tended toward significance, and since this is the value used for studies indicating vascular disease, such as flow mediated dilation (4), it suggests diameter change may become significant with a larger study population. However, since wall shear is thought to be an important underlying physical stimulus for arterial dilation it may represent an important indicator for disease, worthy of further study. In addition, these results suggest that using the appropriate measurement and analysis vehicle, WSR may be a more practical and robust measurement than the arterial diameter to determine the effects of renal disease or vascular disease in association with renal disease. Lastly, our renal disease study group had a high prevalence of vascular disease, which is typical for patients with renal disease. Knowing this, these results further suggest that this measurement method should be tested in other patient populations with known vascular disease to see if these results are reproducible in other settings. Should these findings be reproducible this method may have significant potential for future cardiovascular disease risk stratification.

## 4.5 Conclusion

This study demonstrated that healthy subjects have significantly higher $\overline{\mathrm{WSR}}_{\mathrm{mean}}$ and $\overline{\mathrm{WSR}}_{\mathrm{max}}$ than renal disease (CKD and ESRD) patients. The findings were corroborated by using both top and bottom vascular wall edges, which yielded significant differences with $p < 0.05$. The average $\overline{\mathrm{WSR}}_{\mathrm{mean}}^{\mathrm{post}} - \overline{\mathrm{WSR}}_{\mathrm{mean}}^{\mathrm{pre}}$ was significantly higher also for healthy subjects than subject with renal disease, again at both the top and bottom wall edges ($p$= 0.004 and 0.006). The arterial diameter change between pre- and post-blood occlusion was not different from renal disease (CKD and ESRD) subjects.

# Chapter 5 Conclusions

## 5.1 Major Achievements

The elasticity of the arterial wall was measured using ultrasound 2D speckle tracking and these ultrasound results were compared with measurements of arterial strain as determined by finite-element analysis models. These measurements were performed with and without a surrounding tissue, which was represented by homogenous material with fixed elastic modulus. The wall edges and edge velocity gradient were estimated for the *in-vitro* flow experiment using decorrelation based velocity measurements. The vascular wall edges and vascular wall shear rate in the brachial artery were also measured using a decorrelation based ultrasound measurement method for nine healthy, six chronic kidney disease and two end-stage renal disease subjects. The vascular wall shear rate and vascular diameter pre-, during- and post-occlusion with a pressure cuff were measured and compared for five healthy and three renal disease (two chronic kidney disease and one end-stage renal disease) subjects.

The major achievements of this body of research are:

- *Arterial wall elasticity measurements and finite element analysis of arterial wall considering surrounding tissue effect*. Ultrasound radio frequency signals were acquired from B-mode images of a human brachial artery for a healthy adult subject under normal physiologic pressure and with the use of an external pressure (pressure equalization) to increase strain. Strain differences in the arterial wall during arterial dilation (from diastole to systole) were determined using a 2D speckle tracking algorithm. These ultrasound results were compared with measurements of arterial strain as determined by finite-element analysis models with and without a surrounding tissue, which was represented by a homogenous material with fixed elastic modulus. The results indicated that the surrounding tissue elastic modulus contributes significantly to vascular strain and

methods such as those performed in this study could significantly improve the estimation of vascular elastic modulus.

- *Quantification of wall edges and edge velocity gradient for in-vitro flow experiment using decorrelation based ultrasound flow velocity measurement.* Speckle movement versus correlation curves were obtained for each depth using 2D speckle tracking in a grid region by moving a transducer with a pre-determined speed on a tissue-mimicking phantom. The flow velocity was calculated by multiplying the estimated speckle movement from two consecutive frames by the acoustic frame rate. The wall edge was determined using both the B-mode image and 2$^{nd}$ order gradient of the flow velocity profile. The velocity gradient was measured at the wall edge from the flow velocity profile. The accuracy of the ultrasound measured flow velocity profile and the velocity gradient were evaluated by comparing them with the parabolic velocity profile based on Poiseuille theory. These research results demonstrated the effectiveness and accuracy of this novel flow velocity estimation method in determining the velocity gradient near the vessel wall edge.
- *Measurements of vascular wall shear rate and vascular dilation for healthy and renal disease subjects.* The vascular wall shear rate in the brachial artery was measured using the decorrelation based ultrasound measurement method for nine healthy, six chronic kidney disease and two end-stage renal disease subjects. The vascular wall shear rate pre-, during- and post-vascular occlusion with a pressure cuff were compared for five healthy and three renal disease (two chronic kidney disease and one end-stage renal disease) subjects. The mean and maximum vascular wall shear rate was measured during the cardiac cycle at the top and bottom wall edges, which were determined using the B-mode image and the 2$^{nd}$ order gradient of the blood velocity profile. These research results demonstrated the effectiveness of this approach in determining wall shear *in-vivo*, as well as the potential utility of this approach in distinguishing healthy from diseased vascular physiology, and elucidated the underlying relationship between wall shear and the vascular dilation, which is thought to mediate changes in vascular compliance.

## 5.2 Original Contributions

The original contributions made to the literature within this research are listed below. The list of original contributions are:

1. Measurements of vascular wall strains using ultrasound 2D speckle tracking to evaluate the impact of surrounding tissue on strains.
2. Finite-element analysis of vascular wall elasticity by considering surrounding tissue effect on the arterial wall, demonstrating the previously unrecognized substantial impact of surrounding tissue on vascular strain.
3. Quantification of vascular wall edge location and vascular wall shear rate using decorrelation based ultrasound flow velocity measurement method.
4. Comparison of vascular wall shear rate for healthy and renal disease subjects, demonstrating the differences in underlying shear that may mediate the changes in compliance.
5. Comparison of vascular wall shear rate and vascular diameter pre-, during- and post-vascular occlusion with a pressure cuff for healthy and renal disease subjects that shows the potential utility for using this approach in measuring the underlying physiologic stimulus that actuates physiologic changes in strain.
6. Providing a unifying methodology and measurement approach using speckle tracking for evaluating vascular elastic modulus and the underlying wall shear stimulus that mediates changes in vascular elastic modulus.

## 5.3 Future Work

Based on the results from measurements performed during this research as well as my own analysis of the work performed over the course of this dissertation, the following research is suggested to be performed in order to move this research forward from the point it is currently at:

1. *Increase the range of decorrelation based flow velocity measurements.* The maximum flow velocity measurements are limited by the beam correlation width and acoustic frame rate for the decorrelation based flow velocity measurement. The range of flow velocity measurement will be increased by adjusting the beam

correlation width or increasing acoustic frame rate. This will extend the accuracy and robustness of this measurement approach.

2. *Vascular wall shear rate measurements for cardiovascular disease subjects.* The decorrelation based vascular wall shear rate measurement method should be tested in other patient populations with known vascular disease to see if the results of dissertation are reproducible in other settings. Should these findings be reproducible in other settings, this method may have significant potential for future cardiovascular disease risk stratification.

# References


1. Schiffrin EL, Lipman ML, Mann JF. Chronic kidney disease: effects on the cardiovascular system. Circulation. 2007;116(1):85-97.

2. Galil AG, Pinheiro HS, Chaoubah A, Costa DM, Bastos MG. Chronic kidney disease increases cardiovascular unfavourable outcomes in outpatients with heart failure. BMC Nephrol. 2009;10:31.

3. Di Angelantonio E, Chowdhury R, Sarwar N, Aspelund T, Danesh J, Gudnason V. Chronic kidney disease and risk of major cardiovascular disease and non-vascular mortality: prospective population based cohort study. BMJ. 2010;341.

4. Corretti MC, Anderson TJ, Benjamin EJ, Celermajer D, Charbonneau F, Creager MA, et al. Guidelines for the ultrasound assessment of endothelial-dependent flow-mediated vasodilation of the brachial artery: a report of the International Brachial Artery Reactivity Task Force. J Am Coll Cardiol. 2002;39(2):257-65.

5. Witte DR, van der Graaf Y, Grobbee DE, Bots ML. Measurement of flow-mediated dilatation of the brachial artery is affected by local elastic vessel wall properties in high-risk patients. Atherosclerosis. 2005;182(2):323-30.

6. Bonnefous O, Montaudon M, Sananes J, Denis E, editors. Non invasive echographic techniques for arterial wall characterization. 1996: IEEE.

7. Bonnefous O, Criton A, Germond L, Denis E, editors. New TDI developments for vascular and cardiac applications. 2000: IEEE.

8. Eriksson A, Greiff E, Loupas T, Persson M, Pesque P. Arterial pulse wave velocity with tissue Doppler imaging. Ultrasound in medicine & biology. 2002;28(5):571-80.

9. Guérin AP, London GM, Marchais SJ, Metivier F. Arterial stiffening and vascular calcifications in end-stage renal disease. Nephrology Dialysis Transplantation. 2000;15(7):1014.

10. Luik A, Spek J, Charra B, Van Bortel L, Laurent G, Leunissen K. Arterial compliance in patients on long-treatment-time dialysis. Nephrology Dialysis Transplantation. 1997;12(12):2629-32.

11. Persson M, Eriksson A, Persson H, Lindstrom K, editors. Estimation of Arterial pulse wave velocity with a new improved tissue Doppler method. the 23rd Annual EMBS Interational Conference. 2001: IEEE.

12. Taniwaki H, Shoji T, Emoto M, Kawagishi T, Ishimura E, Inaba M, et al. Femoral artery wall thickness and stiffness in evaluation of peripheral vascular disease in type 2 diabetes mellitus. Atherosclerosis. 2001;158(1):207-14.

13. Mai JJ, Insana MF. Strain imaging of internal deformation. Ultrasound in medicine & biology. 2002;28(11-12):1475-84.

14. Kim K, Weitzel W, Rubin J, Xie H, Chen X, O'Donnell M. Vascular intramural strain imaging using arterial pressure equalization. Ultrasound in medicine & biology. 2004;30(6):761-71.

15. Kim K, Weitzel W, Xie H, Rubin J, Jia C, O'Donnell M, editors. Dual arterial elastic modulus reconstruction from *in-vivo* strain imaging and PWV. 2005: IEEE.

16. Gill RW. Measurement of blood flow by ultrasound: accuracy and sources of error. Ultrasound Med Biol. 1985;11(4):625-41.

17. Brands PJ, Hoeks AP, Hofstra L, Reneman RS. A noninvasive method to estimate wall shear rate using ultrasound. Ultrasound Med Biol. 1995;21(2):171-85.

18. Bambi G, Morganti T, Ricci S, Boni E, Guidi F, Palombo C, et al. A novel ultrasound instrument for investigation of arterial mechanics. Ultrasonics. 2004;42(1-9):731-7.

19. Francalanci L, Dallai A, Tortoli P, Palombo C, Ghiadoni L, editors. Simultaneous measurement of wall shear stress and arterial distension in FMD studies. 2010: IEEE.

20. Levenson J, Pessana F, Gariepy J, Armentano R, Simon A. Gender differences in wall shear-mediated brachial artery vasoconstriction and vasodilation. J Am Coll Cardiol. 2001;38(6):1668-74.

21. Samijo SK, Willigers JM, Barkhuysen R, Kitslaar PJ, Reneman RS, Brands PJ, et al. Wall shear stress in the human common carotid artery as function of age and gender. Cardiovasc Res. 1998;39(2):515-22.

22. Tortoli P, Morganti T, Bambi G, Palombo C, Ramnarine KV. Noninvasive simultaneous assessment of wall shear rate and wall distension in carotid arteries. Ultrasound Med Biol. 2006;32(11):1661-70.

23. Aoudi W, Liebgott H, Needles A, Yang V, Foster FS, Vray D. Estimation methods for flow imaging with high frequency ultrasound. Ultrasonics. 2006;44 Suppl 1:e135-40.

24. Bohs LN, Friemel BH, Trahey GE. Experimental velocity profiles and volumetric flow via two-dimensional speckle tracking. Ultrasound in medicine & biology. 1995;21(7):885-98.

25. Bohs LN, Geiman BJ, Anderson ME, Breit SM, Trahey GE. Ensemble tracking for 2D vector velocity measurement: Experimental and initial clinical results. IEEE Trans Ultrason Ferroelectr Freq Control. 1998;45(4):912-24.

26. Gallippi C, Bohs L, Anderson M, Congdon A, Trahey G, editors. Lateral blood velocity measurement in the carotid artery via speckle tracking. 2001: IEEE.

27. Trahey GE, Allison JW, von Ramm OT. Angle independent ultrasonic detection of blood flow. IEEE Trans Biomed Eng. 1987;34(12):965-7.

28. Ku DN. Blood flow in arteries. Annual Review of Fluid Mechanics. 1997;29(1):399-434.

29. Li W, van der Steen AF, Lancee CT, Honkoop J, Gussenhoven EJ, Bom N. Temporal correlation of blood scattering signals in vivo from radiofrequency intravascular ultrasound. Ultrasound in medicine & biology. 1996;22(5):583-90.

30. Li W, van der Steen AF, Lancee CT, Cespedes I, Bom N. Blood flow imaging and volume flow quantitation with intravascular ultrasound. Ultrasound in medicine & biology. 1998;24(2):203-14.

31. Bamber J, Hasan P, Cook-Martin G, Bush N. Parametric imaging of tissue shear and flow using B-scan decorrelation rate. J Ultrasound Med. 1988;7:S135.

32. Li W, Lancee CT, Cespedes EI, van der Steen AF, Bom N. Decorrelation of intravascular echo signals: potentials for blood velocity estimation. J Acoust Soc Am. 1997;102(6):3785-94.

33. Chen JF, Fowlkes JB, Carson PL, Rubin JM, Adler RS. Autocorrelation of integrated power Doppler signals and its application. Ultrasound in medicine & biology. 1996;22(8):1053-7.

34. Fowlkes JB, Carson PL, Moskalik A, Chen JF, Rubin JM. Method and apparatus for composition and display of three-dimensional image from two-dimensional ultrasound scan data. Google Patents. 2000.

35. Tuthill TA, Krucker JF, Fowlkes JB, Carson PL. Automated three-dimensional US frame positioning computed from elevational speckle decorrelation. Radiology. 1998;209(2):575-82.

36. Rubin JM, Fowlkes JB, Tuthill TA, Moskalik AP, Rhee RT, Adler RS, et al. Speckle decorrelation flow measurement with B-mode US of contrast agent flow in a phantom and in rabbit kidney. Radiology. 1999;213(2):429-37.

37. Rubin JM, Tuthill TA, Fowlkes JB. Volume flow measurement using Doppler and grey-scale decorrelation. Ultrasound in medicine & biology. 2001;27(1):101-9.

38. Bilato C, Crow M. Atherosclerosis and the vascular biology of aging. Aging (Milan, Italy). 1996;8(4):221.

39. Brüel A, Oxlund H. Changes in biomechanical properties, composition of collagen and elastin, and advanced glycation endproducts of the rat aorta in relation to age. Atherosclerosis. 1996;127(2):155-65.

40. Faury G. Function-structure relationship of elastic arteries in evolution: from microfibrils to elastin and elastic fibres. Pathologie Biologie. 2001;49(4):310-25.

41. Pannier BM, Avolio AP, Hoeks A, Mancia G, Takazawa K. Methods and devices for measuring arterial compliance in humans. American journal of hypertension. 2002;15(8):743-53.

42. Millasseau SC, Stewart AD, Patel SJ, Redwood SR, Chowienczyk PJ. Evaluation of Carotid-Femoral Pulse Wave Velocity. Hypertension. 2005;45(2):222-6.

43. Zhang X, Greenleaf JF. Noninvasive generation and measurement of propagating waves in arterial walls. The Journal of the Acoustical Society of America. 2006;119:1238.

44. Pislaru C, Kantor B, Kinnick RR, Anderson JL, Aubry MC, Urban MW, et al. In vivo vibroacoustography of large peripheral arteries. Investigative radiology. 2008;43(4):243.

45. Lubinski MA, Emelianov SY, O'Donnell M. Speckle tracking methods for ultrasonic elasticity imaging using short-time correlation. IEEE Trans Ultrason Ferroelectr Freq Control. 1999;46(1):82-96.

46. O'Donnell M, Skovoroda AR, Shapo BM, Emelianov SY. Internal displacement and strain imaging using ultrasonic speckle tracking. Ultrasonics, Ferroelectrics and Frequency Control, IEEE Transactions on. 1994;41(3):314-25.

47. Weitzel WF, Kim K, Rubin JM, Xie H, O'Donnell HXM. Renal Advances in Ultrasound Elasticity Imaging: Measuring the Compliance of Arteries and Kidneys in End-Stage Renal. Blood Purif. 2005;23:10-7.

48. Weitzel WF, Kim K, Park DW, Hamilton J, O'Donnell M, Cichonski TJ, et al. High-Resolution Ultrasound Elasticity Imaging to Evaluate Dialysis Fistula Stenosis. Semin Dial. 2009;22:84-9.

49. Sarvazyan A. Mechanical imaging: A new technology for medical diagnostics. International journal of medical informatics. 1998;49(2):195-216.

50. Carson P, Johnson M, Holmes JH. Image Quality and Practicality of Scanning Large Abdomens with Large, Low Frequency and Smaller, High Frequency Transducers. Ultrasound in Med. 1978;4:161-2.

51. Kroll MH, Hellums JD, McIntire LV, Schafer AI, Moake JL. Platelets and shear stress. Blood. 1996;88(5):1525-41.

52. Vennemann P, Lindken R, Westerweel J. In vivo whole-field blood velocity measurement techniques. Experiments in fluids. 2007;42(4):495-511.

53. Adler RS, Rubin JM, Fowlkes JB, Carson PL, Pallister JE. Ultrasonic estimation of tissue perfusion: a stochastic approach. Ultrasound Med Biol. 1995;21(4):493-500.

54. Banjavic R, Zagzebski J, Madsen E, Jutila R. Ultrasonic beam sensitivity profile changes in mammalian tissue. Ultrasound in Med. 1978:515-8.

55. Papoulis A. Probability, random variables, and stochastic processes. New York: McGraw-Hill. 1965.

56. Oosterveld BJ, Thijssen JM, Verhoef WA. Texture of B-mode echograms: 3-D simulations and experiments of the effects of diffraction and scatterer density. Ultrason Imaging. 1985;7(2):142-60.

57. Widmaier E, Raff H, Strang K. Vander's Human Physiology: McGraw Hill. 2006.

58. Othman NS, Jaafar MS, Rahman AA, Othman ES, Rozlan AA. Ultrasound Speed of Polymer Gel Mimicked Human Soft Tissue within Three Weeks. International Journal of Bioscience, Biochemistry and Bioinformatics. 2011;1(3):223-25.

59. Melany ML, Grant EG, Farooki S, McElroy D, Kimme-Smith C. Effect of US contrast agents on spectral velocities: in vitro evaluation. Radiology. 1999;211(2):427-31.

60. Shung K. Diagnostic ultrasound: imaging and blood flow measurements: CRC Press Taylor & Francis. 2006.

61. Gokce N, Keaney JF, Jr., Hunter LM, Watkins MT, Menzoian JO, Vita JA. Risk stratification for postoperative cardiovascular events via noninvasive assessment of endothelial function: a prospective study. Circulation. 2002;105(13):1567-72.

62. Kuvin JT, Patel AR, Sliney KA, Pandian NG, Rand WM, Udelson JE, et al. Peripheral vascular endothelial function testing as a noninvasive indicator of coronary artery disease. J Am Coll Cardiol. 2001;38(7):1843-9.

63. Modena MG, Bonetti L, Coppi F, Bursi F, Rossi R. Prognostic role of reversible endothelial dysfunction in hypertensive postmenopausal women. J Am Coll Cardiol. 2002;40(3):505-10.

64. Neunteufl T, Heher S, Katzenschlager R, Wolfl G, Kostner K, Maurer G, et al. Late prognostic value of flow-mediated dilation in the brachial artery of patients with chest pain. Am J Cardiol. 2000;86(2):207-10.

65. Perticone F, Ceravolo R, Pujia A, Ventura G, Iacopino S, Scozzafava A, et al. Prognostic significance of endothelial dysfunction in hypertensive patients. Circulation. 2001;104(2):191-6.

66. Toborek M, Kaiser S. Endothelial cell functions. Relationship to atherogenesis. Basic Res Cardiol. 1999;94(5):295-314.

67. Irace C, Cortese C, Fiaschi E, Carallo C, Farinaro E, Gnasso A. Wall shear stress is associated with intima-media thickness and carotid atherosclerosis in subjects at low coronary heart disease risk. Stroke. 2004;35(2):464-8.

68. Zhao SZ, Ariff B, Long Q, Hughes AD, Thom SA, Stanton AV, et al. Inter-individual variations in wall shear stress and mechanical stress distributions at the carotid artery bifurcation of healthy humans. J Biomech. 2002;35(10):1367-77.

69. Gnasso A, Carallo C, Irace C, Spagnuolo V, De Novara G, Mattioli PL, et al. Association between intima-media thickness and wall shear stress in common carotid arteries in healthy male subjects. Circulation. 1996;94(12):3257-62.

70. Lou Z, Yang WJ, Stein PD. Errors in the estimation of arterial wall shear rates that result from curve fitting of velocity profiles. J Biomech. 1993;26(4-5):383-90.

71. Stroev PV, Hoskins PR, Easson WJ. Distribution of wall shear rate throughout the arterial tree: a case study. Atherosclerosis. 2007;191(2):276-80.

72. Wu SP, Ringgaard S, Oyre S, Hansen MS, Rasmus S, Pedersen EM. Wall shear rates differ between the normal carotid, femoral, and brachial arteries: an in vivo MRI study. J Magn Reson Imaging. 2004;19(2):188-93.